FROM TUBERCULOSIS DIAGNOSTICS TO THERAPY:

DEVELOPMENT OF A TAIL FIBER PROTEIN-DERIVED MICROFLUIDIC

DIAGNOSTIC DEVICE AND UTILIZATION OF SYNERGISTIC PROPERTIES OF

ANTIMYCOBACTERIAL DRUGS

A Dissertation

by

SIMON ROUSSEAU

Submitted to the Graduate and Professional School of
Texas A&M University
in partial fulfillment of the requirements for the degree of

DOCTOR OF PHILOSOPHY

Chair of Committee,   Jean-Philippe Pellois
Committee Members, Hays Rye
                          Jason Gill
                          Michael Polymenis
Head of Department,   Josh Wand

December 2021

Major Subject: Biochemistry

Copyright 2021 Simon Rousseau

ABSTRACT

Tuberculosis, the disease caused by the mycobacterial pathogen *Mycobacterium tuberculosis*, has been, prior to the COVID-19 pandemic, the world's deadliest infectious disease. The illness has been afflicting humans for centuries, and despite decades long efforts to eradicate it and the availability of curative treatment options, tuberculosis remains prevalent across most of the globe. According to the WHO Tuberculosis Reports, approximately 1.7 billion people are estimated to be infected by the bacteria and 1.5 million people die from the disease every year. Effective diagnostics and treatment are key to combating any infectious disease pandemic and in this work, we present a novel approach to improving both. We created a magnetophoretic microfluidic device which uses recombinant mycobacteriophage tail fiber proteins bound to magnetic nanoparticles to pull down mycobacterial cells, selectively concentrating the cells before performing a diagnostic microbiological stain protocol. We have shown that we could lower the limit of detection of *Mycobacterium tuberculosis* from a synthetic sputum sample by 6 to 26-folds per milliliter of sample, without significantly altering the process used at point-of-care clinics. We also investigated the synergistic interactions between drugs, which we believe is a key element to improving efficacy of drug regimen, but also for the creation of new drug combinations, specifically designed to work together. We have shown that using low doses of Bedaquiline causes inhibitors of PEPCK to be synthetically lethal, despite their lack of whole cell activity on their own. This suggests that typical drug discovery campaign may be missing some valuable compounds, that could play an important part of a combination regimen. Furthermore, we have synthesized the necessary substrate

required for the development of an enzymatic assay for peptidyl tRNA hydrolase. This assay could then be used to identify inhibitors of PTH, which could restore Mtb sensitivity to macrolides. These drug discovery campaigns seek to make a better use of synergistic drug interaction and use this information as an integral part of drug discovery.

DEDICATION

Dédié à Denis, Céline et Jean-Denis

ACKNOWLEDGEMENTS

I would like to thank my graduate advisor Dr. Jim Sacchettini for his support and giving me the explore my scientific curiosity. I would also like to thank Dr. Inna Krieger for her guidance and mentorship. I would also like to thank all my committee members; Dr. Jean-Philippe Pellois, Dr. Michael Polymenis, Dr. Jason Gill and Dr. Hays Rye.

Thanks also go to my friend, who made my time in College Station more enjoyable through runs, rides and trivia nights.

Finally, thanks to my family for their support over the years. A special thanks to my mother, Celine, father Denis and brother Jean-Denis.

CONTRIBUTORS AND FUNDING SOURCES

Contributors

This work was supervised by Dr. James Sacchettini and a thesis committee consisting of Dr. Jean-Philippe Pellois, Dr Hays Rye and Dr. Michael Polymenis of the Department of Biochemistry and Biophysics and Dr. Jason Gill of the Department of Animal Science.

In Chapter 2, identification and cloning of gp232 was done by a previous graduate student, Jennifer Tsai. Microfluidics experiments were all performed in collaboration with Song-I Han from the laboratory of Dr. Arum Han.

In Chapter 3, the groundwork for PEPCK drug discovery introduced in the chapter introduction was done by Dr. Haelee Kim and published in her Dissertation "Structure-guided Inhibitor Design of Mycobacterium Tuberculosis Drug Targets from Central Carbon Metabolism". Compounds were designed and synthesized in collaboration with the TB Alliance.

In Chapter4, the work was done with the assistance of Danielle Scott, a Chemistry graduate Student in the lab

All other work conducted for the thesis was completed by the student independently.

NOMENCLATURE

Mtb	*Mycobacterium tuberculosis*
M. smeg	*Mycobacterium smegmatis*
TB	Tuberculosis
TFP	Tail Fiber Protein
MB-P	Tail Fiber Protein bound Magnetic Beads
GFP	Green Fluorescent Protein
BDQ	Bedaquiline
PEPCK	Phosphoenolpyruvate Carboxykinase
PEP	Phosphoenolpyruvate
OAA	Oxaloacetate
PK	Pyruvate Kinase
LDH	Lactate Dehydrogenase
NADH	Nicotinamide adenine dinucleotide
μM	Micromolar
nM	Nanomolar
CFU	Colony Forming Unit
PTH	Peptidyl tRNA Hydrolase
tRNA	Transfer RNA
SDS-PAGE	Sodium Dodecyl Sulfate-Polyacrylamide Gel Electrophoresis
Urea-PAGE	Urea-Polyacrylamide Gel Electrophoresis
SAR	Structure-Activity Relationship
CDC	Center for Disease Control

WHO   World Health Organization

TABLE OF CONTENTS

LIST OF FIGURES

LIST OF TABLES

CHAPTER I

INTRODUCTION:

THE TUBERCULOSIS BURDEN

In recent years, tuberculosis has surpassed HIV has the deadliest infectious disease in the World(1). Despite decades-long efforts to eradicate the disease, its global burden has remained somewhat stagnant, with its incidence declining 1.6 % per year during the 2000-2018 period, short of the "End TB Strategy" milestone(1). There are multiple factors contributing to this, including antiquated point-of-care diagnostics, the extensive and lengthy regimen currently used to treat the disease, as well as the rise of antibiotic resistance.

Tuberculosis is the disease associated with a bacterial infection by *Mycobacterium tuberculosis* (Mtb). The earliest signs of tuberculosis can be traced back to Ancient Egypt, where signs of the disease were found in mummies(2). However, since those signs of tuberculosis were only discovered in mummies centuries later, there wouldn't be any writings on the disease until much later. Indeed, the first written descriptions of pathology that could be described as tuberculosis-like were found in India and China approximately 3000 years ago(3). From that point on, signs of tuberculosis could be found at almost any point of human history, being referenced constantly across the globe and various cultures. References to the illness can be found in the Bible(4), in Ancient Greece and in the Roman Empire(3).

Growth of civilization on a previously unseen scale during the Roman Empire era also brought what appears to be the beginning of the tuberculosis pandemic. Although pathological observation of tuberculosis had been found long before Rome was founded, these cases were rare and dispersed. However, during the Roman Empire era, we see these cases increase in frequency as the Empire grew(5). This is nothing particularly surprising, as civilization grows, people live closer to one another and interact more frequently. Roads were built and people started moving further and further. All these factors are well known contributors to the spread of infectious disease and are likely to have driven up the frequency of tuberculosis in Europe.

Over the course of the 17th, 18th and 19th centuries, the tuberculosis pandemic continued to grow, acquiring a few nicknames along the way. In the 18th century it was called "The Robber of Youth", due its elevated mortality rate of 900 per 100 000 each year and the fact that it was even more elevated in young people. Around that same era, it acquired the nickname of "White Plague", this time due to how pale people affected by the disease looked. A century later, tuberculosis had become known as "The Captain of All These Men of Death", as the epidemic had spread throughout Europe and North America, it is believed that it was then responsible for one in four deaths(3).

Over the course of the next few years, more and more became known about the extent of the disease and its possible origins. Scientists started to understand the infectious nature of the illness, as well as its effects on the body. Matthew Baillie first described the cheese-like necrotic granulomas, known as caseum, in 1793. Then, a few years later, in 1810, the generalized nature of the disease was described by Gaspard-Laurent Bayle of Vernet(3). Jean-Antoine Villemin later demonstrated that tuberculosis was indeed an

infectious disease, which had been a quite contested point prior to his 1865 work "Cause et nature de la tuberculose: son inoculation de l'homme au lapin" and 1868 "Études sur la tuberculose. Preuves rationelles et expérimentales de sa spécificité et de son inoculabilité"(6).

However, the most significant step forward in understanding tuberculosis came in 1882, when the German doctor Robert Koch discovered the bacteria responsible for this affliction, Mtb. He sought to look for a foreign agent that could be responsible for the affliction. He made unusual observation from staining of the bacteria he had isolated from patients. Strangely, the bacillus behaved similarly to the causative agent of leprosy(7), which turned out to be *Mycobacterium leprae* a close relative of Mtb. The staining protocol discovered by Robert Koch would later be perfected by Franz Ziehl. This technique would become known as Ziehl-Neelsen stain, commonly referred to as Acid-Fast staining. To this day, Acid-Fast staining remains a crucial method for the identification of Mtb, as will be discussed later(8, 9).

Dr. Koch was able to repeatedly isolate bacilli within lesions of infected patients. To try to further demonstrate the hypothesis that this bacterium was the cause of tuberculosis, Koch isolated it and devised means to propagate it. He was able to show that bacteria isolated from patients was able to grow on lung tissues and that infecting guinea pigs with these isolated bacteria lead to tuberculosis disease. Through these experiments, he was able to convincingly demonstrate that tuberculosis was caused by a single infectious agent; Mtb. For his work, he was awarded the Nobel Prize in Medicine in 1905(8).

Since the discovery of the Mtb bacilli, the pandemic as continued to spread despite available treatments. The current statistics are staggering. An estimated 1.7 billion people are believed to be infected by the mycobacterial pathogen. Although the majority of the infected individuals will never develop the disease, the number of active tuberculosis cases remains high, at approximately 10 million new cases per year, leading to an estimated 1.5 million deaths on an annual basis(1, 10). To place that number into perspective, according to the WHO, the COVID-19 pandemic that brought the world to a halt in 2020 caused 1.3 million reported deaths that year, although the WHO also suggests the true number is likely to be closer to 3 million. Nevertheless, the number of deaths associated with tuberculosis is of similar magnitude as those caused by COVID-19, but has been happening year after year, for decades. Developing countries carry the overwhelming majority of the tuberculosis burden, with 8 countries (India, China, Indonesia, Philippines, Pakistan, Nigeria, Bangladesh and South Africa) accounting for two thirds of the global number of TB cases. As such, tuberculosis is considered a disease of poverty and therefore the global community often fall short of the funding necessary for TB prevention, diagnosis, and care. In 2019, only US$ 6.8 billion was available, while an estimated US$ 10.1 billion was required(1).

Tuberculosis is considered a curable disease. The recommended regimen consists of two phases: intensive and continuation. During the intensive phase, four drugs are administered daily for a total of 8 weeks. These drugs are Isoniazid (INH), Rifampicin (RIF), Pyrazinamide (PZA) and Ethambutol (EMB). After those first 8 weeks of treatment, RIF and INH will continue to be administered daily for an additional 18 weeks. In total, the preferred regiment for the treatment of tuberculosis comprises 182 doses(11). Due to this

exhaustive treatment course, non-adherence is quite frequent, with studies estimating non-adherence to be around 25-30%(12-14).

These anti-mycobacterial agents were all discovered over a period of a few years, from the 1950s to 1970s. Since then, a few more candidates have been studied, but it took until 2012 for a new drug to be approved by the FDA(15). That drug was Bedaquiline, an inhibitor of ATP synthase. Since then, two more drugs received approval Delamanid (EU-only) in 2014(16) and Pretomanid in 2019(17). At the moment, these drugs are only to be used for cases of multi drug resistant TB (MDR-TB).

The emergence of multi drug resistant tuberculosis is also increasingly becoming a concern. A total of 186 772 cases of multi drug resistant tuberculosis were diagnosed in 2018, up from 160 684 cases the previous year(1). Several key countries, such as Russia, Myanmar, South Africa and China, are seeing an increase in Rifampicin resistant tuberculosis infections(18). Recent studies have shown that the majority of drug resistant infections were due to the direct transmission of a drug resistant strain of Mtb rather than acquired resistance due to prior treatment(19), it is thus crucial to reduce and eventually eliminate transmission.

Mtb is spread from person to person primarily by respiratory droplets. The pathogen will then make its way through the pulmonary system to the lower respiratory tract, where it will be ingested by alveolar macrophages. Unlike many pathogens, Mtb does not try to avoid phagocytosis, but in fact promotes it through multiple receptor such as C-type lectin receptors (CLRs)(20), scavenger reporters (SRs)(21) and complement receptors

(CRs)(22). Mtb is an intracellular pathogen able to survive inside infected macrophages by altering its environment and halting phagosome maturation(23). The exact mechanism by which Mtb achieves is not completely understood and is an active area of TB research. Phagosome maturation is regulated by Rab GTPases. The Rab5-Rab7 conversion is a crucial step in maturation from early to late endosome(24), and it is believed that this is one of the mechanisms targeted by Mtb that leads to maturation arrest(25). The phagosomal maturation arrest is a crucial element to Mtb's survival. Indeed, the intracellular nature of the pathogen is one of the reasons it is so difficult to treat. In the macrophage it is exposed to acidic pH, nitric oxide stress, limited nutrients and hypoxic stress(26). These stressors cause the bacteria to enter a latent stage, where many cellular processes are significantly reduced, making drug discovery more challenging.

CHAPTER 2

HIGHLY SENSITIVE DETECTION OF MYCOBACTERIUM TUBERCULOSIS BY

COMBINING MYCOBACTERIOPHAGE TAIL FIBER PROTEINS AND

MAGNETOPHORETIC MICROFLUIDICS

Introduction

The very first step towards eradication of any epidemic is fast and efficient diagnostics. Although there are a variety of methods used for diagnosing patients displaying TB-like symptoms, on the global scale, current diagnostics falls short of our needs, especially in developing countries with limited resources in terms of funding and infrastructures. Testing can be separated into two categories, point-of-care testing, and laboratory testing. In the case of tuberculosis, the laboratory testing methods are accurate and sensitive. They range from cell culturing, chest X-ray, tuberculin skin test and PCR based diagnostics(27). These techniques are often required to be done in some centralized laboratory, due to the expensive equipment used and operating expertise that isn't always available in local clinics.

The chest x-ray (CXR), tuberculin skin test (TST) and Interferon-γ Release Assay (IGRA) methods are very commonly used in the United States to screen immigrants. This is especially prevalent amongst international college students. Indeed, the American College Health Association, which counts 700 higher learning institutions as its members, recommends TST, IGRA to be used to screen all students coming from high-incidence

countries

(https://www.acha.org/documents/resources/guidelines/ACHA_Tuberculosis_Screening
_May2020.pdf). Due to the magnitude of the TB pandemic, that list comprises most
countries, the list of "low-incidence" being much shorter, and populated mainly with the
world's richest countries, and a handful of Caribbean countries.

The Tuberculin Skin Test is one of the preferred screening tests. Per the CDC, TST is
performed by injecting 0.1 milliliter of purified Tuberculin protein into the skin of the
forearm and observing the reaction to the injection(28). The diagnosis is made by
measuring the induration created at the injection site, the larger the induration the
stronger the positive diagnosis is. The biggest downside to TST is the high frequency of
false positives. There are multiple factors that can lead to false positive results by TST,
such as previous exposure to non-tuberculosis mycobacteria, and more significantly prior
vaccination with the bacille Calmette-Guerin (BCG) vaccine(28). Since almost every
country outside the United States and Canada has a BCG vaccination program (or did at
some point)(29), the TST can only be relied on in a narrow set of circumstances.

Interferon-γ Release Assay measures, as the name suggests, measures the release of
interferon by white blood cells when exposed to tuberculosis specific antigens(30). Per
CDC guidelines, this technique is often recommended in situations where TST is
expected to fail, most importantly for anyone who has received the BCG vaccination.
However, IGRA is more expensive, almost 10 times the cost of TST.

The chest X-Ray is commonly used to confirm prior test results, either by TST or IGRA.
It is a radiological imaging test, based on the observations of anterior posterior
radiograph. Tuberculosis creates lung lesions that are visible by X-Ray, and as such, the

presence of lesions in the lungs, coupled with a positive result with either TST or IGRA is a strong indicator of TB disease. However, the presence of lesions alone is not considered by the CDC or the WHO to be a definitive diagnosis of tuberculosis(31).

One of the more recent and sensitive techniques for detection of Mtb is the GeneXpert MTB/RIF system developed by Cepheid. The GeneXpert MTB/RIF is a molecular diagnostics tool relying on nucleic acid amplification. Its main advantage is that it cannot only detect the presence of Mtb, but also detect the presence of the most common Rifampicin resistance mutations located in the *rpoB* gene(32, 33). However, this specific diagnostics tool requires specific instrumentation and single use cartridges. As such the cost per test is much higher than some of the other options. Cost-analysis studies have found this method to be cost-effective despite the higher cost(34). However, the initial investment threshold is much higher, mostly keeping this tool away from point-of-care settings, especially in developing countries(34).

The point-of-care methods are where we are severely lacking in terms of sensitivity and accuracy. Point-of-care diagnosis is a crucial element of the fight against Mtb but is also plagued with significant limitations. These clinics are typically limited in terms of equipment, budget, trained staff, and also stable and robust access to electricity. It is therefore not surprising that to this day, the most widely employed method used for diagnosing possible tuberculosis patients is the sputum smear microscopy test, followed by culture-based diagnosis(35). The sputum test is simple, fast, and cheap. A small fraction of a patient's sputum sample will be placed on a microscope slide and stained

with Ziehl-Neelsen reagent. This will stain all acid-fast bacteria present in the sample which includes all mycobacteria as well as a few other types of microorganisms. Although the selectivity of the test is not optimal, due to the fact that it will stain a few other bacterial species, the low sensitivity is the major issue with this technique. The lack of sensitivity can be explained by the small amount of sample that can be processed at one time. Indeed, although multiple milliliters of sputum can be obtained for each patient, only approximately 10 microliters are used per slide. Furthermore, this small amount of volume still represents 10 000 fields of view when imaged at 100x, which is the magnification used for the test. A standard sputum smear microscopy test will look at 100-300 fields of view, further diluting how much of the sample is actually being tested(36). Because of this, in order to observe a single mycobacterium cell, the bacterial load must be at least 10 000 bacilli per milliliter, which is high. The follow up culture-based test is much more sensitive. However, due to the slow growth rate of the bacteria, it can take up to a month for the laboratory to be able to make a diagnosis.

This lack of sensitivity leads to multiple false negative smear tests, which unfortunately can be propagated through the community. Studies have attempted to quantify how much of the spread of tuberculosis could be attributed to false-negative smear tests. In a 1999 study, it was estimated that smear-negative tuberculosis patients accounted for 17% of the Mtb spread in San Francisco(37). Another similar study published in 2008, attributed approximately 13% of the Mtb spread to smear-negative patients, this time in the Netherlands(38). A third study in the Greater Vancouver area (2004) concluded that at least 1/6 of Mtb transmission came from smear negative patients (39). This is not all that

surprising when considering how long it takes to get further testing done, specifically culture tests. Indeed, in developing countries, although sputum smear microscopy is the first test done at the point-of-care, samples are typically sent to a central lab for culture testing. This has a much higher sensitivity than smear microscopy, however it takes a month to obtain the results due to Mtb slow growth rate. This is compounded by the often-slower means of communication in the developing world, therefore allowing infected individuals to continue to interact within their communities, spreading the pathogen.

Mycobacteriophages are viruses that have the ability to bind and inject their DNA into mycobacteria, followed by viral DNA replication and eventually leading to cell lysis. Bacteriophages are divided into three categories based on their tail morphology seen under electron microscopy. These categories are myoviridae, siphoviridae and podoviridae. The myoviridae have a rigid contractile tail, while the siphoviridae have a long flexible tail and the podoviridae have a short stubby tail. The overwhelming majority of known mycobacteriophages have been siphoviridae, with a few myoviridae and no known podovirdae(40).

All bacteriophages have some form of a tail fiber protein that is responsible for the adsorption of the virus to the bacterial membrane. The nomenclature can become a little confusing, since each morphological bacteriophage classifications uses different names for similar tail fiber structures. Briefly, there are three types of tail fiber-like proteins, short and long tail fiber proteins as well as tail spike. The long tail fibers extend outward from the baseplate. The long tail fiber proteins are usually responsible to the first viral

adsorption step. Short tail fibers are also attached to the baseplate, but in general downward position. As the name suggests, they are typically shorter. The tail spike is primarily seen in podoviridae and is a very short and stubby protein. According to the literature, this binding interaction of tail fiber is weak, and in order for the virus to be irreversibly attached to the cell, multiple tail fibers must be bound at the same time(41). Short tail fibers will then irreversibly bind to the cell before injecting the viral DNA.

The viral will then use the host machinery for replication and protein synthesis to generate more viral particles, which will then be released when the host cell is lysed by the various lysis proteins encoded by the viral genome.

Identification and Binding Specificity of Mycobacteriophage Tail Fiber Proteins

Since sputum smear microscopy remains the most commonly used point-of-care diagnostics in areas where tuberculosis is most prevalent, our approach was to bring improvement to sensitivity without bringing too much change to the current methodology. The biggest obstacle to sensitive diagnostics tools based on microscopy is the amount of sample that can be processed at once. Indeed, regardless of the amount of available sample, only a small fraction can be visualized and analyzed. As such, in order to improve sensitivity of sputum smear microscopy, we must find a way to specifically concentrate large volumes of sample, into a smaller volume, which can later be imaged, quantified and analyzed.

To do this, we decided to use an approach not unlike affinity chromatography, which is used for purification of proteins from cell lysate. Briefly, the lysate is applied to a chromatography column, which contains a biomolecule capable of binding to the protein of interest, typically some kind of tag that was bioengineered onto the recombinant protein of interest. The idea would be that we may be able to specifically concentrate Mtb if we were able to bioengineer a molecule capable of binding whole mycobacterial cells from sputum samples and use it to separate the bacterium from the rest of the sample.

The obvious first step to this approach is to identify such molecules that would be capable of binding to Mtb. Luckily a large reservoir of such molecules exists in Nature and are readily available. These molecules are mycobacteriophage tail fiber proteins. More specifically they are the Receptor Binding Domain (RBD) at the tip of the tail fiber protein,

which is responsible for the binding of the mycobacteriophage to the cell surface of the mycobacterial species the virus can infect.

Unfortunately, in the literature, there were no mycobacteriophage tail fiber proteins previously annotated and experimentally validated for any mycobacteriophage, despite the fact that large databases of mycobacteriophage are readily available(40).

In order to identify a tail fiber protein, we first looked at the literature to find possible similarities between tail fiber proteins identified in other bacteriophages and the gene product of a mycobacteriophage. Using this approach, we obtained our first candidate tail fiber protein, gp232 of mycobacteriophage Bxz1. Although previously annotated as a putative head decoration protein, it was also shown to have similarities to gp204 of phage E3, a myoviridae cable of infecting *Rhodococcus equi*. The annotation of head decoration protein is also a bit unusual and unlikely. Indeed, head decoration proteins are typically small proteins(42), meanwhile gp232 is one of Bxz1's largest proteins with over 1000 residues. This is much more typical of tail fiber proteins, which tend to be one of the larger open reading frames in the bacteriophage genome. One element that could lead one to believe gp232 is a head decoration protein is the immunoglobulin-like domain it contains, which has been found in head decoration proteins such as protein pb10 of bacteriophage T5(42, 43). However, these domains have also been found in tail fiber proteins and other bacteriophage structural proteins(43).

In order to demonstrate that gp232 of Bxz1 is a probable tail fiber protein that can selectively bind to Mycobacteria, we decided to use a confocal fluorescence microscopy approach. We chose this approach because it allows a direct comparison between the binding interactions between the tail fiber protein and different bacteria in a single

14

experiment, virtually guaranteeing identical experimental conditions and identical confocal microscope settings for all bacteria tested. In order to do so we first created a recombinant protein, tagged with Green Fluorescent Protein (GFP) and a hexa-histidine tag, expressed it in *E. coli* and purified it by affinity chromatography. Once we have obtained the purified recombinant tail fiber protein, we assessed its binding selectivity by adding the purified protein to a mixed bacterial culture containing both *Mycobacterium smegmatis*, the bacteria Bxz1 was isolated on, and *E. coli*, a gram-negative bacteria that cannot be infected by Bxz1, and therefore should not be bound by its tail fibers. To better visualize this, and to be able to distinguish between the two bacterial species more easily, the *E. coli* strain used was also expressing a red fluorophore (mCherry). Both bacteria were mixed in a ratio of approximately 1:1. For this experiment, we decided to use a relatively low concentration of tail fiber proteins and used no washing steps. Since the strength of the interaction was unknown, we wanted to avoid disrupting the interaction by using centrifugation to remove excess protein.

The results are in strong accordance with gp232 being a tail fiber protein of Bxz1 (Figure 1, page 22). Under these experimental conditions, we observed no colocalization between the green fluorescence coming from the gp232 fusion protein and the red fluorescence from the mCherry *E. coli*. However, cells that were not expressing red fluorescence, which by process of elimination must be *M. smegmatis,* were readily labelled with green fluorescence, indicating that the fluorescent tail fiber proteins were bound to the cell surface of *M.smeg*, but not *E. coli*. Furthermore, using confocal microscopy's ability to use a narrow focal plane, we observed that the pattern of fluorescent labelling changed. Indeed, when we focused on the middle of the bacteria,

the highest intensity was at the perimeter of the cell (Figure 1B, page 22), however when we moved the focal plane a little higher, focusing on the top of the bacteria, the fluorescence was strongest in the middle (Figure 1C, page 22). Taken together these results suggest that the fluorescent tail fiber protein is bound to the cell surface of *Mycobacterium smegmatis* but is unable to do so with E. coli. These results are strongly consistent with the hypothesis that gp232 is indeed a probable tail fiber protein of Bxz1. Unfortunately for us, the mycobacteriophage Bxz1 is unable to infect Mtb. Like virtually all mycobacteriophages, it was first isolated by enriching with *M. smegmatis*. It is not uncommon for bacteriophages to have the ability to infect multiple species within a genus, but it is not a guarantee. In the case of Bxz1 the host range did not extend to the Mtb(44). We thus shifted our focus towards another mycobacteriophage, one with the ability to infect Mtb. We chose TM4 as the candidate because of its ability to infect Mtb is well documented(45, 46) due to its use as a transduction tool and because its genome is one of the most well annotated of all mycobacteriophages. Despite the relatively complete annotation of TM4, no tail fiber protein had been properly identified. To identify the probable tail fiber protein, we took advantage of some well conserved genome organization features of bacteriophage. Within many phage genomes, the genes are clustered by function. Tail assembly is one of the better examples of this. That structural cluster can typically be found by identifying the tape-measure protein, which determines the length of the major tail of the virus(47). This specific protein is often preceded by a chaperone protein characterized by a -1 translational frameshift(48). Once the chaperone (gp15, gp15-16) and tape-measure protein (gp17) have been identified, we can often find tail fiber proteins in the genes immediately downstream. In the case of TM4 these proteins

had already been annotated has minor tail proteins (gp19-gp26)(46). One of these genes annotated as minor tail protein is likely to be the tail fiber protein responsible for binding to the bacteria.

We also know that tail fiber proteins are typically one of the larger open reading frames in a bacteriophage genome. We could thus further narrow down the likely candidates based on gene size; indeed, well known tail fiber proteins tend to be relatively large, gp17 of T7 is 500 residues(49) while gp37 of T4 is over 1000 residues(50). By only considering genes of at least 350 amino acids, located within the tail assembly cluster, we could narrow down the tail fiber to four potential genes: gp18, gp19, gp21 and gp23. To further narrow down the candidates, we took advantage of another features of bacteriophage tail fiber protein. Although the sequence of two tail fiber protein genes from different bacteriophages can share little to no similarity, their three-dimensional structures tend to be similar. We therefore hypothesized that, although gp232 of Bxz1 may not have much sequence homology to any of the candidate tail fiber proteins of TM4, it is likely that their structures would be similar. We thus decided to use a structure prediction software called I-TASSER(51) to identify which one, if any, of our candidates' genes shared similar structural features than our previously identified probable tail fiber protein (Figure 2, page 23).

The results from gp23 were particularly encouraging. The predicted model of gp232 of Bxz1 and gp23 of TM4 were very similar to one another (Figure 3C, page 25). Additionally, the threading model selected by I-TASSER for both of these genes was the same PDB entry (4OM9) (Figure 3A, page 24). The actual model is not what we were interested in, because it is highly unlikely to be correct, without a very good model. However, the fact

17

that I-TASSER recognized similarities in structural features and used the same PDB entry to build a model strongly suggest that gp232 of Bxz1 and gp23 of TM4 are likely to be structurally similar. Furthermore, the general organization of secondary structural features is highly similar between the two proteins (Figure 3B, page 24). Taken together, these results made gp23 the strongest candidate as a putative tail fiber protein from mycobacteriophage TM4.

In order to confirm this and evaluate the binding specificity of this protein, we used the same confocal microscopy approach as we previously used with gp232. The results were the same as with the other probable tail fiber protein (Figure 4, page 26). There was no colocalization between the green fluorescence of the gp23-GFP fusion protein and the mCherry expressed by *E.coli*. However, just like previously observed with GFP-gp232, cells that were not expressing mCherry, which are presumed to be *M. smegmatis*, were labelled with green fluorescence indicating that our gp23 based recombinant protein was able to bind to the cell surface of mycobacteria. Just like in the previous experiment, adjusting the focal plane of the confocal microscope altered the distribution of the fluorescent signal consistent with labelling of the cell surface.

Furthermore, since TM4 is able to infect Mtb as well as *Mycobacterium smegmatis*, we repeated our mixed bacterial population confocal microscopy experiment, but this time replaced mCherry *E. coli* with mCherry Mtb. We continued using a strain of *M. smegmatis* that does not express any fluorescence. Since we expect the tail fiber protein to be able to bind both bacterial species, we expect to observe GFP labelling of both bacteria in the

mixture, the Mtb expressing red fluorescence as well as the non-fluorescent *M. smegmatis.*

Our results did in fact demonstrate that gp23 of TM4 was able to bind both mycobacterial species. However, our results clearly show a difference in fluorescence intensity between the two species (Figure 5A-D, page 27). Indeed, not all cells expressing mCherry seemed labelled with the tail fiber protein, and those that were, had visibly lower fluorescence intensity. This result is not entirely surprising. Like most mycobacteriophages, TM4 was discovered by enriching with *M. smegmatis*, it is thus likely that this specific mycobacteriophage has higher binding affinity with that specific species.

In order to investigate this further, we repeated the experiment, but this time using a monoculture of Mtb. When compared to the mixed population experiment, the labelling of Mtb was more predominant when *M. smegmatis* was absent (Figure 5E-H, page 27). This suggests a binding preference for *M. smegmatis* over *M. tuberculosis*. The binding dynamics between tail fibers and various host microbes could be an interesting avenue for further studies.

For this approach to be successful, the proteins must be able to bind to the bacteria and remain bound while the rest of the sample is washed away. Therefore, the next step was to evaluate the stability of the binding interaction over time between the recombinant tail fiber protein and the mycobacterial cells. To test this, we decided to use a microfluidics approach. The advantages of microfluidics are relatively straightforward. First, by using

microfluidics, we are able to process relatively large samples (milliliter amounts), while the captured bacteria will remain bound in a very small volume. Secondly, the flow rate can be sped up to increase the processing speed of the sample but can also be reduced to lower the shear force applied to the bound protein. Third, this approach allows the sample to be thoroughly washed without major disruption to the captured cells, as washing solutions can easily be applied to the microfluidic chip to remove as much of the sample contaminants as possible.

We constructed a microfluidic chip, which was capable of capturing bacterial cells due to the shallow height of the device's channels. *Mycobacterium smegmatis* cells were first injected into the device, where the bacteria remained captured, but the media was able to continue flowing towards the outlet. We then injected the GFP-labelled recombinant tail fiber protein of gp23 in the device at 5 µL per hour for 3 hours. We then washed the cell continuously overnight at the same flow rate with 7H9- OADC media. Our results clearly demonstrate that the recombinant tail fiber protein is capable of remaining bound to the mycobacteria over a long period of time in a microfluidics setting as the fluorescence intensity remained high, despite hours of constant washing (Figure 6, page 28).

<u>Sub-Chapter Summary</u>

Taken together, these results strongly suggest that we have identified two probable tail fiber proteins. Both gp232 of mycobacteriophage Bxz1 and gp23 of Mycobacteriophage TM4 display selective binding towards the bacterial species they are able to infect,

consistent with the expected behavior of such proteins. Furthermore, through our confocal microscopy assays we have also shown that these proteins can be recombinantly expressed, purified and that they retain their ability to bind to the cell surface of mycobacteria. Lastly, we demonstrated that in a microfluidics setting, the GFP labelled tail fiber protein is able to bind to *M. smegmatis* and remain bound for long periods of time with constant flow sheer force being applied. We can thus conclude that the probable tail fiber protein gp23 of TM4 possesses all the necessary characteristics to be used as a biomolecule capable of selectively capturing Mtb and to concentrate the bacteria in a microfluidics environment.

Figure 1
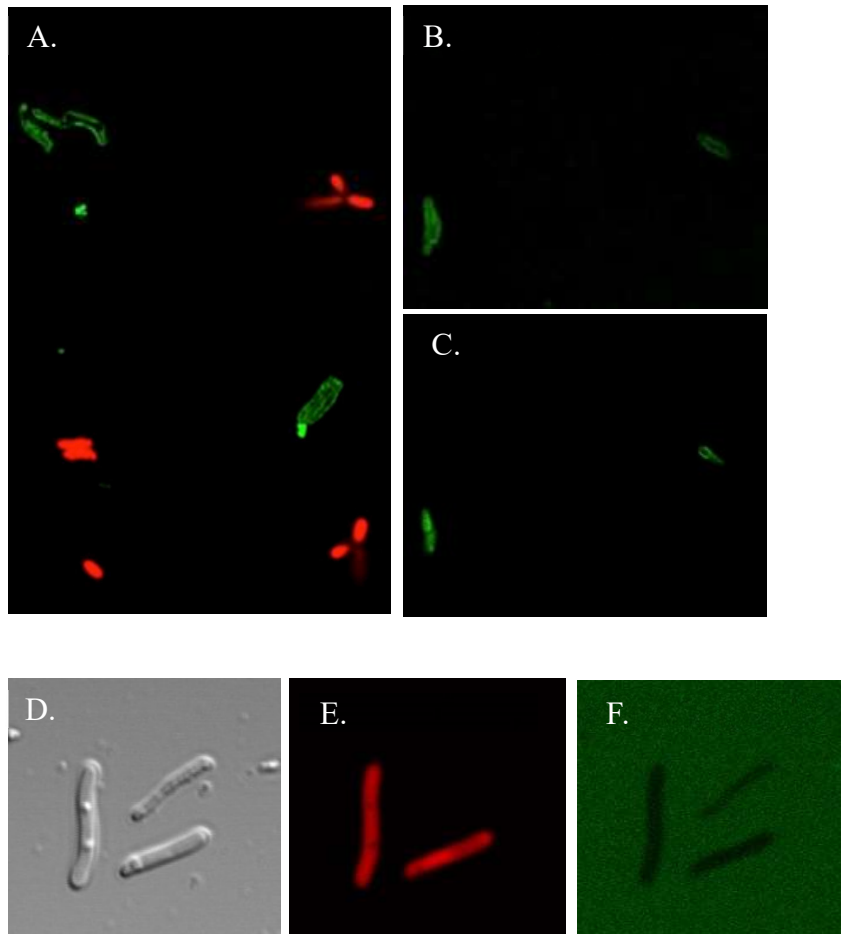
Figure 1 Binding selectivity of gp232 of Bxz1 demonstrated by confocal microscopy

Co-culture of *M. smegmatis* and *E. coli* expressing mCherry in the presence of GFP-gp232. Representative image (A.) shows no colocalization between GFP fusion TFP and *E. coli*, but significant interaction with *M. smegmatis*. Adjustment of the focal plane is consistent with GFP labelling of the bacterial membrane (B and C). Control experiment with GFP alone shows no interaction of fluorophore with either bacteria, strongly demonstrating that interaction is through TFP (D-F).

Figure 2

A.
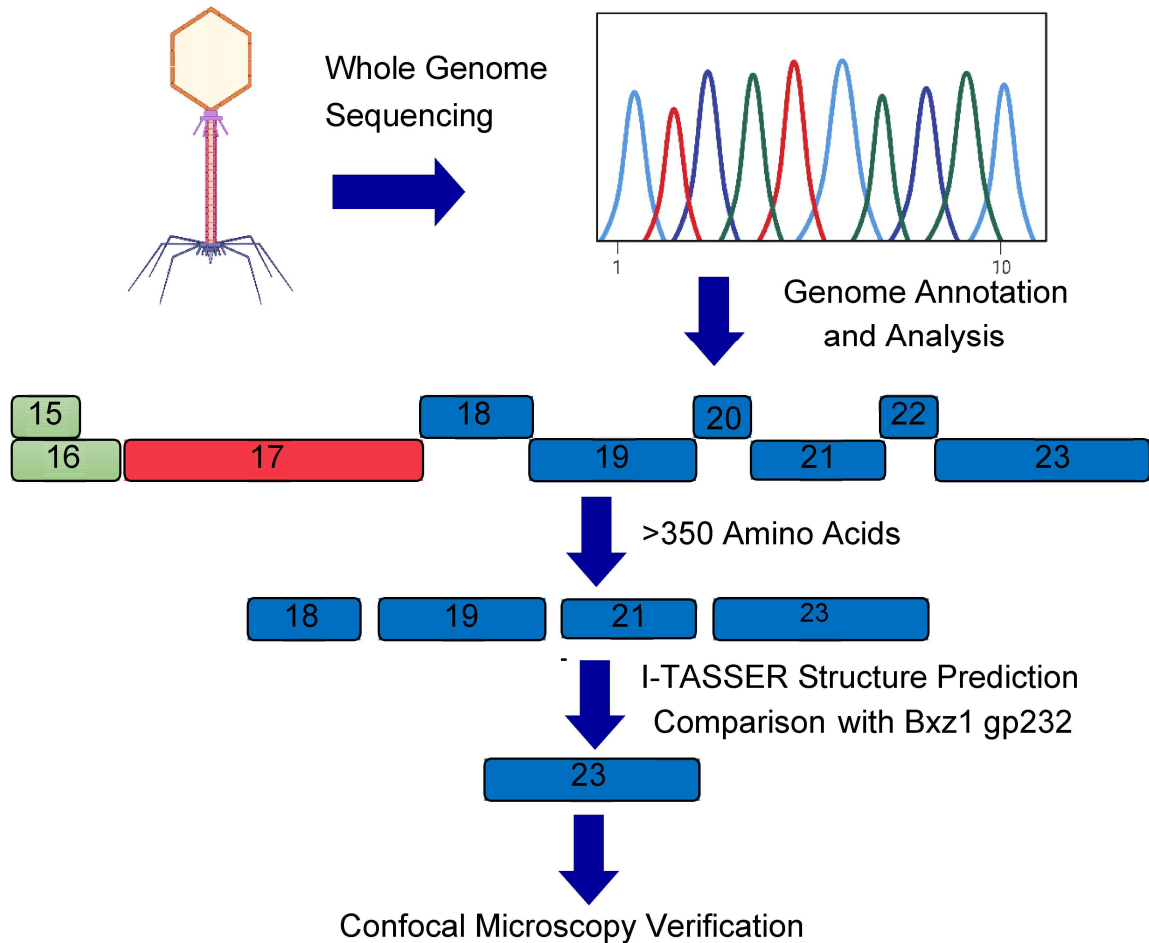
Figure 2. Workflow for the identification of the tail fiber protein of Mycobacteriophage TM4

Workflow explaining the workflow employed to identify gp23 as probable tail fiber protein by sequentially narrowing down candidates based on known aspects of bacteriophage biology and tail fiber proteins themselves. Sequencing and annotation was obtained from the Actinobacteriophage Database(40)

Figure 3

A.

Bxz1 gp232   TM4 gp23

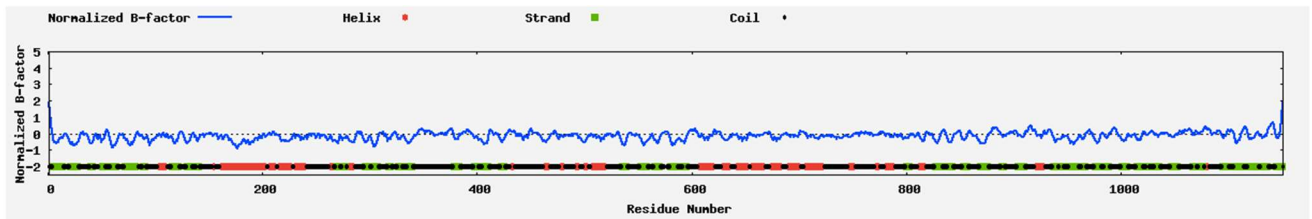I-Tasser structure prediction threading template   I-Tasser structure prediction threading template

Rank	PDB Hit	Iden1	Iden2	Cov	Norm. Z-score
1	4om9A	0.10	0.21	0.97	1.32
2	4d0qA	0.18	0.05	0.18	1.44
3	1vw1A	0.07	0.18	0.90	1.12
4	4d0qA	0.18	0.05	0.18	2.95
5	4d0qA	0.17	0.05	0.18	2.39
6	4om9A	0.08	0.21	0.95	2.19
7	4d0qA	0.18	0.05	0.18	2.19
8	3ecqA	0.12	0.20	0.66	1.72
9	4fxgA	0.12	0.18	0.80	0.71
10	3v0aB	0.10	0.18	0.97	1.24

Rank	PDB Hit	Iden1	Iden2	Cov	Norm. Z-score
1	4om9A	0.10	0.16	0.80	1.66
2	1wxrA	0.11	0.18	0.82	1.90
3	2cseW	0.08	0.19	0.97	3.54
4	4om9A	0.12	0.16	0.81	1.08
5	4om9A	0.08	0.16	0.73	2.74
6	4om9A	0.09	0.16	0.80	1.23
7	4acqA	0.10	0.21	0.99	1.54
8	4om9A	0.10	0.16	0.75	1.77
9	2cseA	0.07	0.18	0.99	3.52
10	3j6qA	0.12	0.17	0.89	1.00

B.

Bxz1 gp232

TM4 gp23
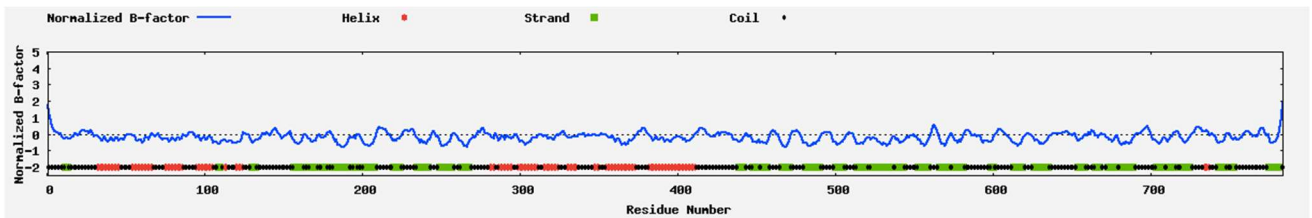
Bxz1 gp232   TM4 gp23
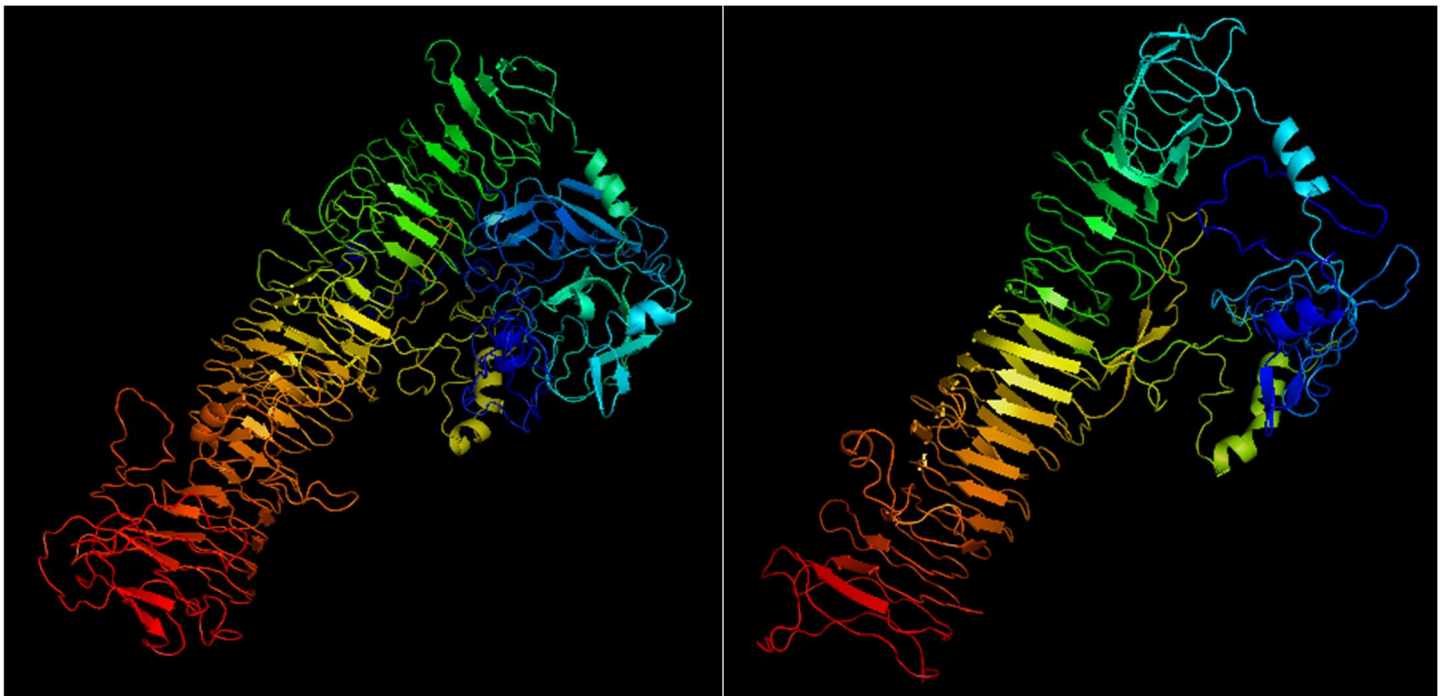
Figure 3. I-TASSER structure prediction software suggests gp23 of TM4 shares structural features with previously identified Bxz1 tail fiber gp232

Based on results of the I-TASSER software gp232 of Bxz1 and gp23 of TM4 share structurally similar features. They share the same PDB entry as the best threading model (A.), have a similar organization of the secondary structure domains (B.) and the predicted models look similar (C.)

Figure 4
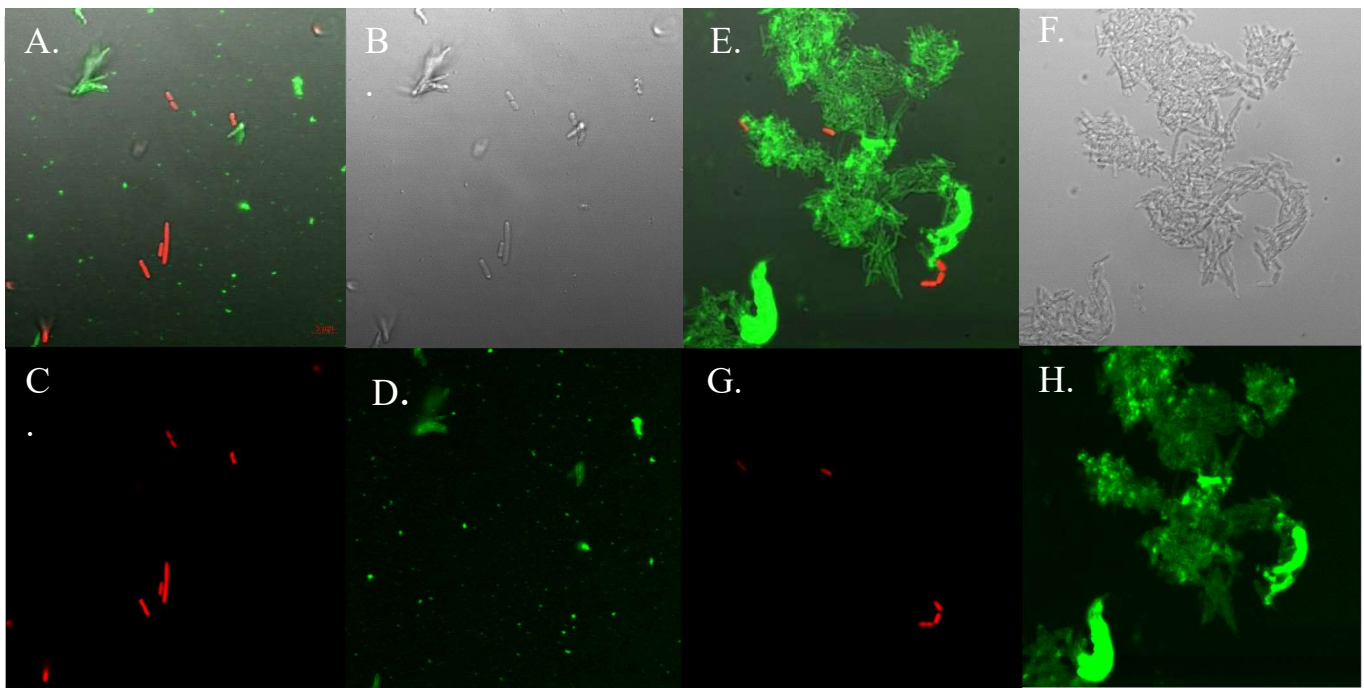
Figure 4. Binding selectivity of gp23 of TM4 demonstrated by confocal microscopy

Representative split channel images of a co-culture of *M. smegmatis* and *E. coli* expressing mCherry shows no co-localization between the mCherry signal of the *E. coli* cells and the GFP fluorescence of the TFP. Merged images (A and E), Bright Field (B and F), mCherry (C and G) and GFP (D and H)

Figure 5
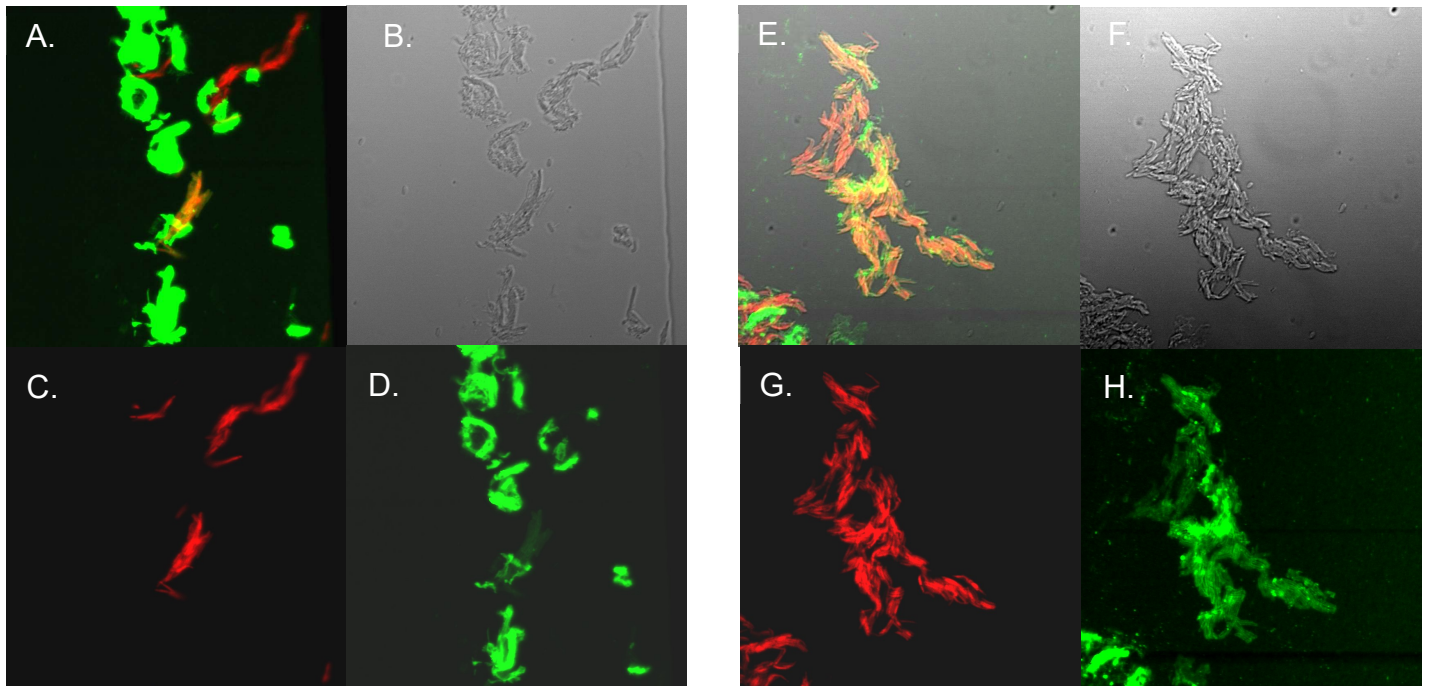
Figure 5. Binding selectivity between Mycobacterial species demonstrated by confocal microscopy.

Representative raw split channel confocal microscopy images of a co culture of mCherry Mtb and M. smegmatis (A-D) or a monoculture of mCherry Mtb (E-H). Tail fiber proteins in a co-culture environment appear to have worse colocalization with mCherry Mtb than in monoculture both in intensity and frequency.

Figure 6
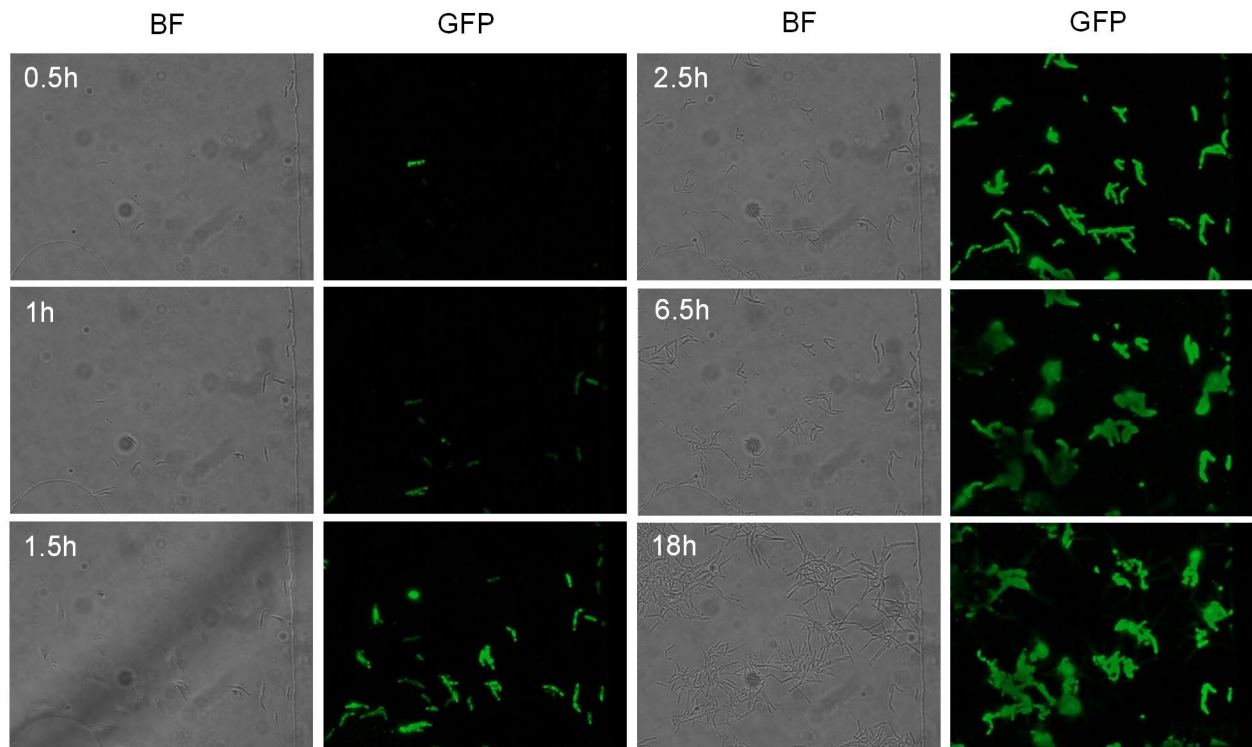
Figure 6 : Time-course imaging in a microfluidic device shows binding stability over time.

Fluorescence microscopy (GFP) and bright field (BF) images of Mtb cell captured in a shallow channel microfluidic device. The device was washed with 7H9 OADC for 18 hours.

Development of a Magnetophoretic Microfluidic Device for the Tail Fiber Dependent Capture of *Mycobacterium tuberculosis*

Once tail fiber proteins were identified and their binding selectivity and stability were experimentally demonstrated by confocal microscopy, we sought to create a device that would be capable of selectively capturing mycobacteria, while allowing other biological material to be washed away. Since microfluidics had already shown promise in a prior experiment, we decided to utilize this approach once more.

We had already shown that tail fiber proteins could remain bound to mycobacteria in a narrow channel design. However, this approach would not be appropriate for a diagnostics application, as this device would capture all material that is the same size as Mtb or larger. Additionally, although tail fibers were able to fluorescently label Mtb cells in this microfluidic chip design, a diagnostics application would require fluorescent microscope, which is unavailable at point-of-care clinics and would be very expensive to acquire.

In order to be able to use light microscopy as a final readout, our approach needed to immobilize the Mtb cells inside the device through immobilization of the tail fiber protein it interacts with, so that non-specific biological material from the sample could freely wash out of the device and that the remaining cells could be stained by Acid-Fast staining and imaged with a light microscope.

In the field of microfluidics, one common approach to immobilize analytes inside of the device is magnetophoresis, which consists of using a magnetic field to pull down the molecule of interest bound to magnetic particles.

For this approach to work, we first had to be able to conjugate our tail fiber proteins onto a magnetic particle. We were able to obtain commercially available magnetic nanoparticles conjugated with nitrilotriacetic acid (NTA), which is a chemical commonly used to purify proteins containing a hexa-histidine tag during affinity chromatography. Since our recombinant tail fibers already contained a hexa-histidine tag capable of binding to an NTA molecule, this was the perfect design for our microfluidic device.

The microfluidic device itself was a fairly simple design (Figure 7A, page 36). It contained a single inlet and a single outlet. Inside the device, the channel would then separate into 4 different channels each containing a capture chamber, which would be place on top of a magnet to pull down the magnetic nanoparticles. The channel height was 20 μm, which is wide enough to allow any sample contaminants to be washed away, while things bound to the nanoparticles would remain at the bottom of the device until the magnetic force is removed. The device was constructed from Polydimethyl Siloxane (PDMS) that is bound to a glass substrate.

The nanoparticles we used were 132 nm in diameter and were coated with NTA and were obtained from MicroMod. We chose to use nanoparticles of that size in order to increase the number of nanoparticles that could be bound to each mycobacterial cell, which measures approximately 5 μm in length (Figure 7B, page 36). Before each experiment, tail fiber proteins would be added to these magnetic beads to create the magnetic bead/tail fiber protein complex (MB-P). Excess tail fiber proteins would then be washed away by using a magnetic microcentrifuge tube holder.

Once the device design was finalized and constructed, we then needed to optimize the various parameters and quantify their effects on capture efficiency. To assess capture efficiency, we decided to use an Mtb strain that was constitutively expressing mCherry. The use of a fluorescent bacterial strain would make both the quantification of bacteria in the starting culture and the quantification of cells captured in the device much easier. Indeed, using fluorescent bacteria allows us to use a lower magnification microscope to image the microfluidic channels and count the number of cells that were captured during the experiment. Furthermore, it also allowed us to quickly quantify the concentration of our starting culture, without having to plate out the culture to count the number of colony forming units (CFUs). Having the ability to rapidly quantify our starting cell concentration was crucial since initial cell concentration is an important parameter for this study. Furthermore, we also decided to use single cells for capture efficiency experiments. Mtb has a tendency to form large bacterial clumps when grown in a liquid culture. However, for quantification of capture efficiency purposes, clumps would be problematic as each area of fluorescence could be a single cell or a clump of a few hundred cells. Therefore, before injecting into the device, each culture was first briefly sonicated, which has been shown to break up clumps, and filtered through a 5µm syringe filter, which should only allow single cells to pass through.

Our experimental design to calculate capture efficiency was straightforward. We would first evaluate the cell concentration of our starter culture by adding 5µL of culture onto a microscope slide. We would then image that slide under a fluorescent microscope (20X) and count the total number of cells on the slide. From that number, we could back calculate the concentration of the starter culture. Since that concentration was typically

higher than the desired concentration for our experiments, we would then dilute into fresh 7H9 to a final volume of 1mL. We would then add the MB-P to the sample containing Mtb cells. After 30 minutes of incubation that mixture would then be injected into the device already placed in a magnetic field. After the sample has been fully injected, we would then wash for 2 hours with fresh 7H9 media. After washing, the entire device would be imaged with a fluorescent microscope and the number of fluorescent cells would be counted. The capture efficiency was calculated by dividing the number of cells found in the device by the number of cells injected.

Before we could evaluate any variable, we first used two control experiments to test the amount of non-specific capture expected from the device. First, we inject Mtb cells without the MB-P present. The primary objective of this control experiment was to assess the non-specific interaction between Mtb and the device itself. We expect the capture of Mtb cells to be dependent on its interactions with MB-P, thus this control approximates how much of the sample could remain trapped inside the device without interacting with MB-P. The second control consisted of injecting MB-P along with mCherry expressing *E. coli*. Not unlike the first experimental control, this one was also evaluating the amount of non-specific capture present. The magnetic beads are physical objects and as such could non-specifically trap bacteria. Since we know that gp23 of TM4 is not capable of binding to *E. coli*, the measured capture efficiency must be attributed to non-specific interactions between the bacteria and the magnetics beads. Our results for both controls show very little cell capture, with capture efficiency of 7±1% for the *E. coli* control and a capture

efficiency of 4±6% for the control with no MB-P. We thus concluded that non-specific interactions are likely to contribute to the experimental capture efficiency only minimally.

The first variable we decided to optimize was the flow rate. There are obvious advantages to higher flow rates, as it can speed up the sample processing time. However, the downsides can also be significant, as higher flow rate can negatively affect capture efficiency in two different ways. The higher flow rate will result in higher sheer force, which could disrupt the binding interaction between the MB-P and the mycobacteria. Since the length of the channel was kept constant, higher flow rate could also affect capture efficiency by reducing the total time the sample spends in the capture chamber and thus how long it is exposed to the magnetic field. We decided to use varying flow rates, between 200 and 500 µL per hour and calculated the capture efficiency under all these conditions. Our results (Figure 8A, page 37) clearly demonstrate that flow rate up to 400µL did not have any significant negative impact, with a calculated capture efficiency around 40% at 200, 300 and 400 µL per hour. There was however a slight decrease in capture efficiency at 500µL per hour, with an average capture efficiency of close to 20%.

Next, we sought to understand the relationship between the initial cell concentration and the measured capture efficiency. In order for this approach to be successful at reducing the limit of detection of sputum smear microscopy, it is incredibly important that the capture efficiency remains high at low cell concentrations. We thus varied the number of cells injected into the device, ranging from 500 bacilli per mL and up to 10 000 bacilli per mL. The results were then plotted and a linear trend was observed (Figure 8B, page 37),

33

indicating that initial cell concentration did not significantly affect the capture efficiency, which remained around 40% throughout the entire range of cell concentration used.

Up to this point our device performed quite well, however each prior experiment was done in a pure Mtb culture. The reality of sputum is quite different, with a large amount of other biological material present in the sample. In order to evaluate the effects of possible contaminants on the capture efficiency, we added excess *E. coli* to the culture prior to injecting into the device. We chose *E. coli*, because it resembles Mtb in terms of shape and size, but as we have demonstrated in prior experiments, it does not interact with the tail fiber proteins. If our method is specific to Mtb, it should not be affected by the presence of other biological substances, such as other bacteria. We tested three different samples, representing three different ratios of Mtb to *E. coli*. The first sample contained 10% Mtb, the second 1% Mtb and the last 0.01% Mtb. Each one of the capture efficiency experiments was done in triplicate. The results show no significant difference between the three different ratios of Mtb to *E. coli* (Figure 8C, page 37), strongly indicating that biological contaminants do not have a significantly negative effect on capture efficiency, and that our capture device is specific to Mtb. This experiment is however not a substitute for testing the capture efficiency in a real sputum sample, but the results are encouraging.

Sub-Chapter Summary

Taken together, these data demonstrate that by combining magnetophoretic microfluidic with our tail fiber proteins we were able to capture approximately 40% of the total number

of cells injected in the microfluidic device. This capture efficiency was constant across multiple flow rates and across a wide range of initial cell concentrations. Furthermore, our control experiment demonstrate that this capture efficiency is dependent on the interaction between the tail fiber protein connected to the magnetic bead and mycobacteria, since very few cells would remain in the device in the absence of MB-P or when evaluating the capture efficiency of a bacterial species that does not interact with the tail fiber proteins such as *E. coli*. We also demonstrated that the measured capture efficiency remained mostly unchanged when contaminants were added to the Mtb sample, even when *E. coli* was in 10 000X excess. Although these results are not definitively applicable to a true sputum sample, our results demonstrate the potential of our microfluidic device and demand further testing.
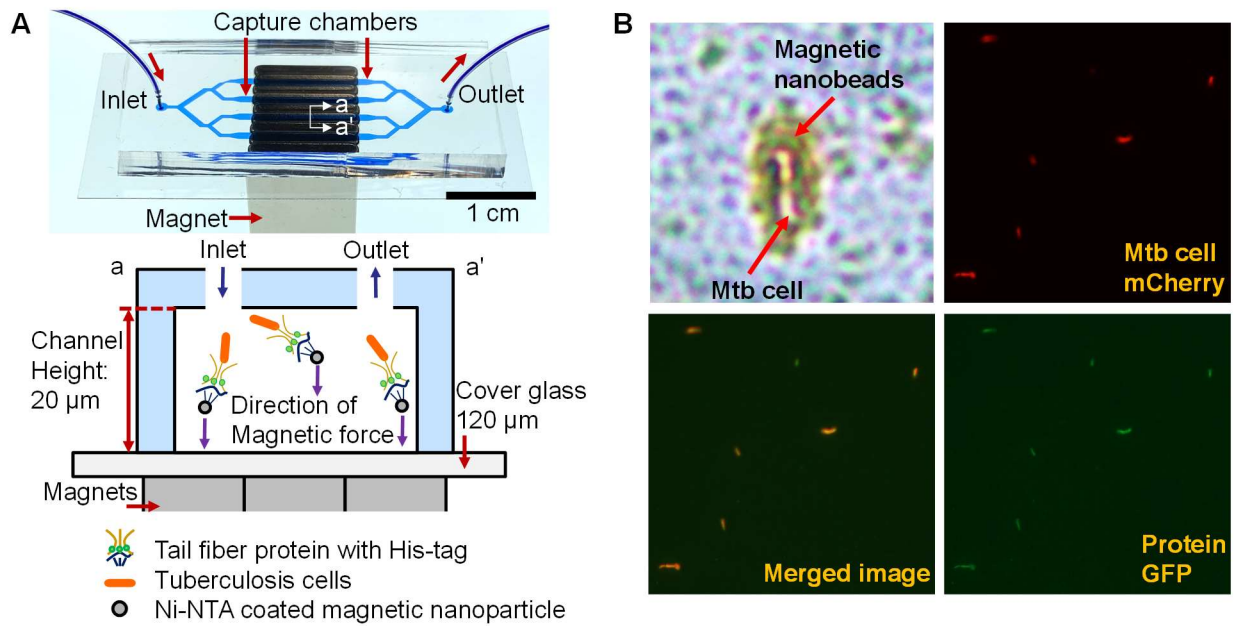
Figure 7 Design of the magnetophoretic microfluidics and MB-P

Design of the microfluidic device (A) shown with the actual device shown on top and a pictorial representation on the bottom. Microscopy images show the MB-P bound to the Mtb cell using a light microscope (B, top left) and a fluorescence microscope (B, top right & bottom)
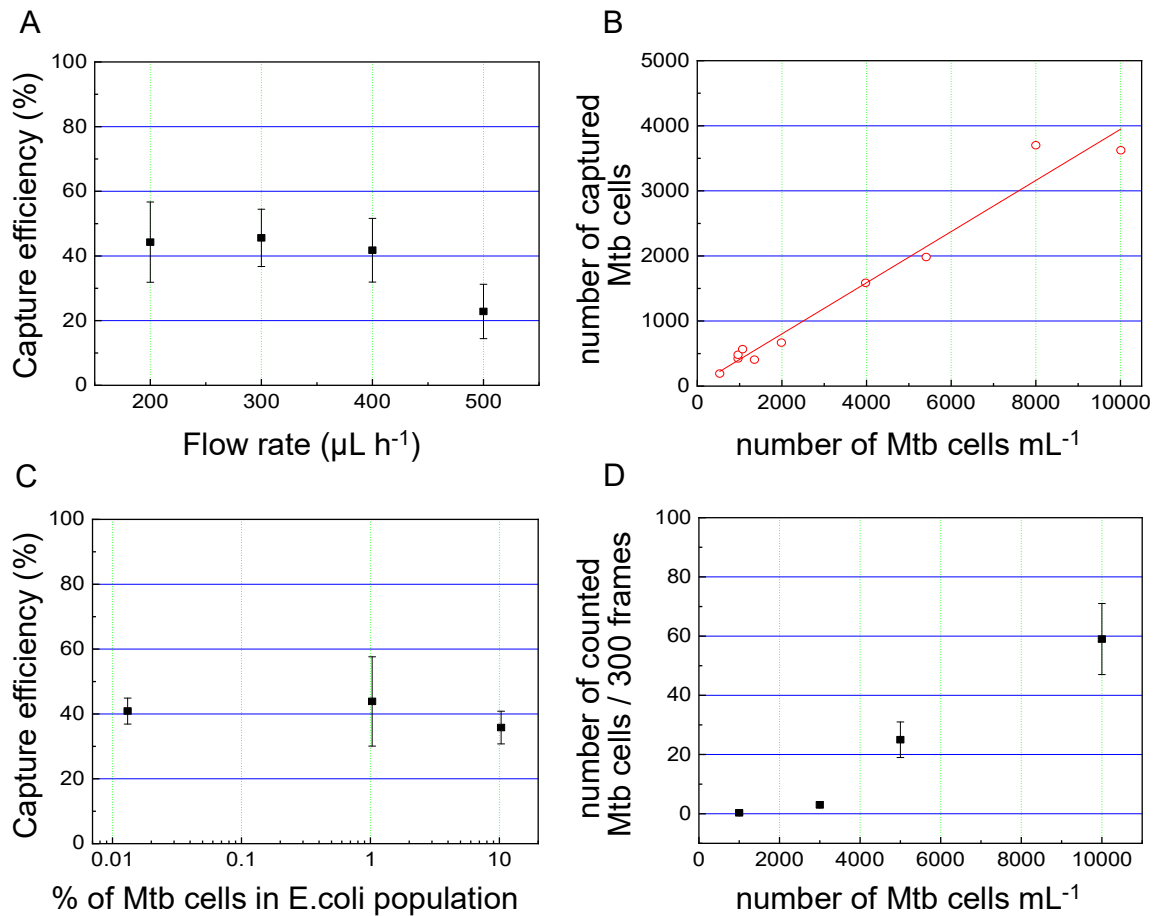
Figure 8. Optimization and characterization of magnetophoretic separation of Mtb cells by MB-P

Effects of flow rate (A.), sample concentration (B.) and non-Mtb bacterial contaminants (C.) on the Mtb capture efficiency of the microfluidic device, measured by fluorescence microscopy. Limit of detection (D) of the microfluidic device in synthetic sputum as measured by acid-fast staining and counted with a light microscope.

<u>Acid Fast Staining of Synthetic Sputum Sample Processed by Magnetophoretic Device</u>

Our prior work clearly demonstrates that our magnetophoretic microfluidics device is capable of consistently capturing mycobacteria in a small volume. Our robust experiment however only used samples that were vastly different from sputum in terms of composition.

Unfortunately, obtaining sputum samples is impossible in a BSL-2 facility, therefore we decided to use synthetic sputum. The synthetic sputum was commercially available from ClaremontBio and was the closest we could get to a true sputum sample in our laboratory. Unfortunately, the capture efficiency experiment previously used was no longer appropriate since the synthetic sputum had significant fluorescence background, which rendered enumeration by fluorescence microscopy impossible.

We thus decided to test the capture efficiency by using another experimental design that most resembles true clinical samples. There are a few significant changes between this series of experiment and the previous capture efficiency. First, we replaced 7H9 media with synthetic sputum obtained from ClaremontBio. Second, we did not filter the bacterial culture before injecting into the device, we did however keep the sonication step. This will break down large clumps of cells to smaller clumps, but we will not completely eliminate them from the sample. The intention for this change was to more closely resemble clinical samples, where Mtb cells form clumps, but these clumps are not as large as those observed when the cells are grown in culture in the lab. Third, the most significant change is how cells would be enumerated.

Because background fluorescence was too high with the synthetic sputum, we decided to use a more clinically relevant acid-fast staining approach. There are a few significant changes required in order to achieve this goal. First, the cell captured in the device must now be taken out of the device. The most effective way to do so was to remove the magnetic field after washing and collect the totality of the contents of the microchannels. However, this created another problem that needed to be addressed. Indeed, by removing the magnetic field, all the contents of the device would be released, which renders staining and imaging very difficult, since the magnetic beads will remain bound to the cell. Furthermore, since the beads were much smaller than the cell itself, the particles were able to coat the bacteria, making the actual microorganism very difficult to distinguish from other particles under a microscope. Our solution to this problem was to treat the ejected sample with high concentration of imidazole prior to staining. Imidazole is used in affinity chromatography to elute Hexahistidine-tagged protein from the Ni-NTA resin it was purified on. Since our tail fiber proteins were attached to the magnetic beads using the same chemistry, the addition of imidazole would cause the tail fiber to be released from the magnetic beads. And since the bacteria was bound to the beads by the tail fiber proteins, this will cause the beads to detach from the bacteria. We then further separated the beads from Mtb by vortexing the ejected sample containing imidazole and used a strong magnet to pull the now detached beads aside.

After the supernatant was removed from the magnetic beads, we took out 10 µL for acid-fast staining. Briefly the sample was placed on a cover slide and air dried on a warm hot plate. After the sample dried, we then heat fixed it to the slide by briefly flaming the glass side. Then, we added a paper towel, trimmed to the right size, on top of the sample and

flooded it with Carbolfuchsin. The slide was then placed above a steaming water bath for 5 minutes, while adding additional Carbolfuchsin as needed to avoid drying. After the time had elapsed, the paper towel was removed, the slide rinsed with water and then destained with an acid alcohol solution containing 1%HCl in 95% ethanol. The slide was rinsed once more after destaining and was then ready for imaging. A typical acid-fast stain would typically have a counterstaining step, however, since our experiment contained only mycobacteria, there was no need for methylene blue counterstaining.

The enumeration process was performed with a light microscope and a 100X objective in a manner that resembles a typical sputum smear microscopy diagnostic. We observed various fields of view at random throughout the entire smear. We counted the number of fields of view required to obtain five images containing at least one acid fast positive bacilli for up to 300 fields of view. Samples with higher concentrations were then extrapolated to the number of positive fields of view that would have been seen in 300 images. For example, if it required 100 images to observe 5 positives, this data point would be recorded as 15 positives in 300 images. This allowed us to directly compare the results between various concentrations of cells in the initial sample.

Before we were able to test any experimental samples, we had to establish a baseline for the sensitivity of the technique. Although the published limit of detection for sputum smear microscopy is often referred to as 10 000 bacilli/mL, this is a bit misleading. The true limit of detection varies wildly between laboratories, due to the skills of the people performing the smear and the evaluation. The published value of 10 000 bacilli/mL represents the best case scenario, but in practice it can be anywhere from 10^4 to 10^5[36]. We thus

decided to first assess the limit of detection using this method, when we performed the experiment, in our own facility. We prepared cell samples containing know quantities of cells and performed our staining and imaging protocols. Our results indicated that our limit of detection is located somewhere between 17 600 and 26 400 per mL. This result was in-line with expectations. Our results fell in the expected range of outcomes, but unsurprisingly was slightly worse than the limit of detection seen at laboratories with extensive experience with such assay.

We tested four different initial cell concentrations; 10 000, 5000, 3000 and 1000 bacilli per mL. Each sample was mixed with MB-P, captured inside the magnetophoretic device, released and stained. From each processed sample we prepared three separate smears for imaging. For the two highest concentrations (10 000 and 5 000 bacilli per mL), cells were easy to find and since we were able to find 5 positive images in less than 300 frames, we extrapolated the results (Figure 8D, page 37 and Figure 9, page 43). We were also able to find a few cells from the sample containing 3000 bacilli per mL originally, however we only observed an average of 3 positive images per smear out of the 300 fields of view that we observed. For the lowest concentration tested of 1000 bacilli per mL, we were able to observe a single positive frame out of the 300 fields of view imaged in one replicate, but unable to detect any bacteria in the other two smears. Since we had to replicate multiple smears in order to get a single positive, we considered 1000 bacilli per mL to be undetectable with our method. As such, we approximate the limit of detection to be somewhere between 1000 and 3000 bacilli per mL.

Our results (Figure 8D, page 37) demonstrate that our sample processing device was able to lower the published detection limit 3.3 to 10-fold. However, when compared to our own detection limit, which takes into account our own experience and skills performing the acid-fast staining, our device shows an improvement of detection limit of 5.87 to 26.4-folds. Importantly, since our device can process any sample volume our limit of detection represents the lowest number of total cells that must be injected into the device. Not necessarily concentration. While all our experiments were performed from a 1mL sample volume, the necessary concentration would be halved if we were to process 2mL of sample. As such the improvement of the limit of detection should be described as 5.87 to 26.4-fold improvement per mL of sample processed.

Figure 9

A.
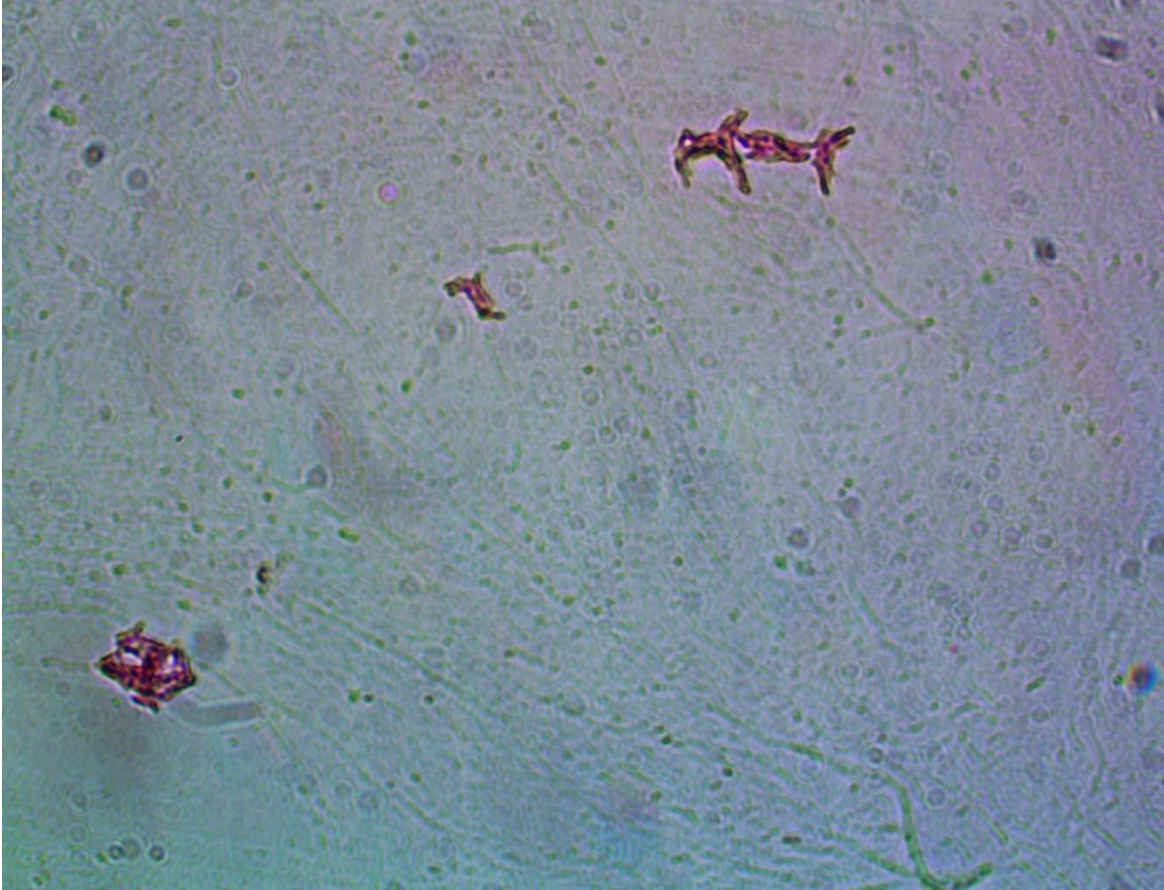
B.
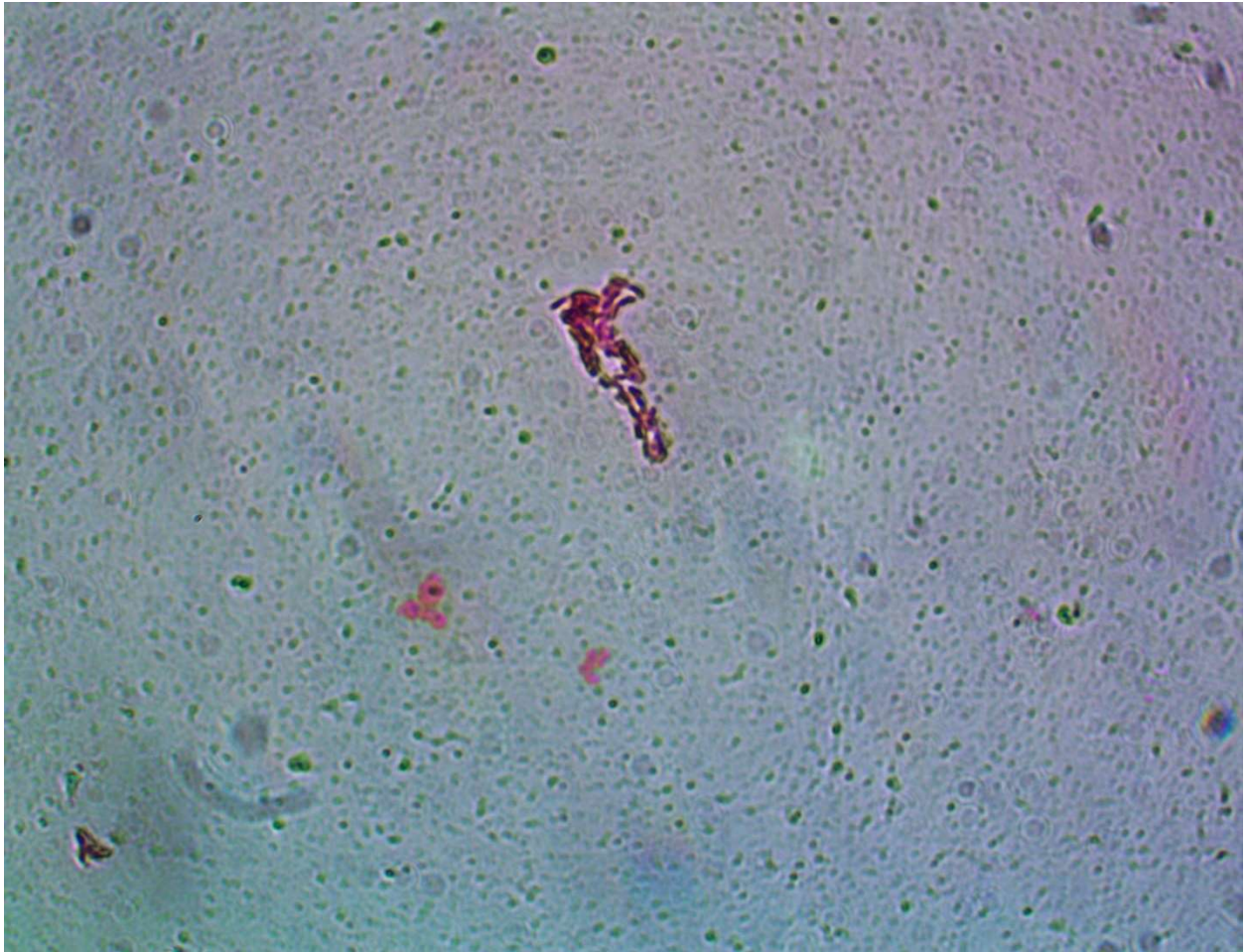
C.
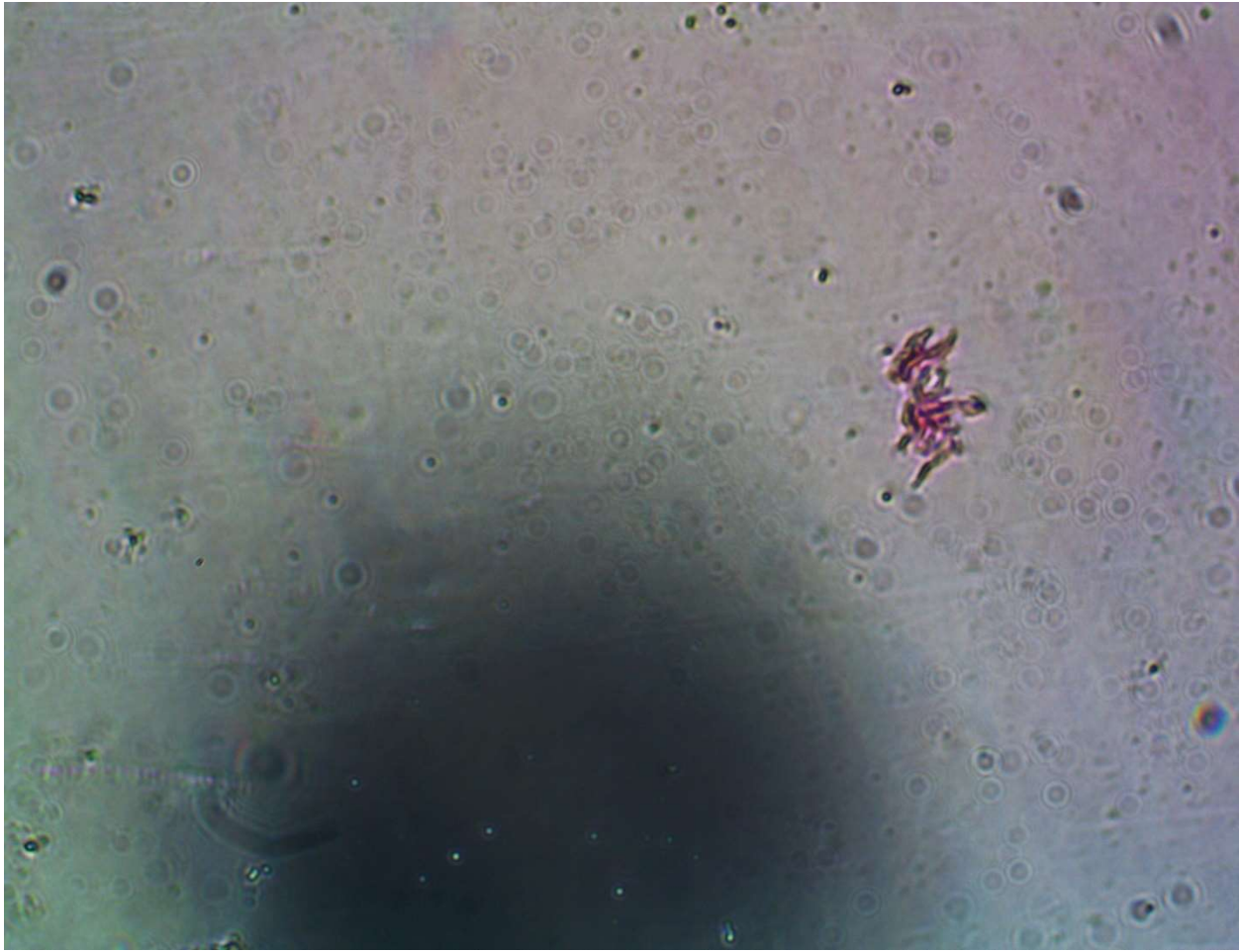
Figure 9 Light Microscopy Images of Acid-Fast Staining used to determine limit of detection

Representative images taken after Microfluidic capture of Mtb,release of contents by removing the magnetic field, removal of beads with imidazole and acid fast staining of the resulting samples. Each image shown is taken from a different initial cell concentration: 10 000 Bacilli per mL (A), 5000 Bacilli per mL (B.) and 3000 Bacilli per mL (C.).

Chapter Summary

Taken together our results show that we were able to identify and purify probable tail fiber proteins from two different mycobacteriophages, Bxz1 and TM4. Our data also demonstrate that each tail fiber is able to bind to its bacterial host in a selective manner and that this binding selectivity is maintained when recombinantly expressed. However, our data cannot absolutely conclude that these proteins are in fact tail fiber proteins, but only that these proteins behave as it would be expected. For the purpose of this work, this is sufficient since the objective was to identify proteins capable of selectively binding to mycobacteria. The magnetophoretic microfluidic device we have designed to take advantage of these probable tail fiber proteins was able to capture approximately 40% of all Mtb cells injected. The resulting processing step, which utilizes magnetophoretic microfluidics and mycobacteriophage tail fiber protein to essentially concentrate Mtb cells in a selective manner, significantly lowered the detection limit of a synthetic sputum sample spiked with Mtb by acid-fast staining and observation under a light microscope. We were able to readily detect samples containing 3000 bacilli per mL, while the published limit of detection for acid fast staining is at around 10 000 bacilli per mL. However, since the true limit of detection can vary significantly between labs and scientists performing the test, we believe our device results should be compared to the limit of detection from our own acid-fast staining experiments. The limit of detection when we performed the experiment was closer to 20 000 bacilli per mL. Furthermore, since our limit of detection is based on total cells injected in the device and not concentration, it can be further lowered by increasing sample volume.

1. Protein Expression and Purification

GFP-gp23 was constructed by cloning a truncation of the C-terminal 365 residues of gp23 into the vector 2GFP-T (Addgene #29716). The N-terminal GFP fusion construct also includes an N-terminal hexahistidine tag. The cloned plasmid was transformed into *E. coli* (BL21 DE3) for protein expression. Cells were grown to an optical density (OD_{60}) of ~0.8, and then induced with 0.5 mM IPTG and cultured overnight at 18 °C for protein expression. Cells were harvested and then lysed by mechanical force (LM20 Microfluidizer) in a lysis buffer containing 50 mM HEPES 7.5, 5% glycerol, 250 mM NaCl, and 5 mM Imidazole. The recombinant GFP-gp23 protein was purified by affinity chromatography using a Ni-NTA Resin (Roche, cOmplete-His) and eluted with 250 mM imidazole. The purified protein was further purified by size-exclusion chromatography (HiPrep 26/60 Sephacryl S-300, Cytiva) using a buffer containing 25 mM HEPES 7.5, 5% glycerol and 150 mM NaCl. The purified protein was concentrated using a centrifugal concentrator (Sartorius Vivaspin Turbo 15).

2. Microbial cell culture

The Mtb strain used was a strain of $Mc^{2}7000$ Mtb(52) and constitutively expressing mCherry constructed on a plasmid with hygromycin resistance. Cells were grown in the

Middlebrook 7H9 media containing OADC and hygromycin. Cells were grown to OD_{600} of 1 before using in the experiments, which typically takes approximately 5 days.

E. coli (BL21 DE3) expressing mCherry was grown on LB media containing carbenicillin to maintain an IPTG-inducible PTXB1 plasmid expressing mCherry. An overnight culture was used to inoculate fresh LB media containing carbenicillin and IPTG, and grown until mid-log phase before imaging.

3. Confocal Microscopy Imaging

Microscopy to image tail fiber protein tagging of microbial cells were conducted using a Zeiss LSM780 confocal microscope with a 63X objective lens (N.A. 1.3) and a 1.6x optical magnification slider. Tail fiber proteins at a final concentration of ~ 0.1 mg mL^{-1} were co-incubated for 15 min at room temperature with microbes (OD_{600} of 1). *M. tuberculosis* cells and *E. coli* cells were tagged separately, and then mixed at va1, before being injected into a low height cell trapping microfluidic device. Excess protein was briefly washed by flowing additional LB media into the channel. Confocal imaging of gp232-GFP fusion protein was carried out on a standard slide with a number 1 coverslip treated with poly-lysine. Images were taken the same way as the gp23-GFP.

4. Fabrication of the microfluidic magnetophoretic Mtb capture device

The microfluidic device consists of a microfluidic channel made of polydimethylsiloxane (PDMS) and a 0.15 mm thick glass substrate (24 by 50 mm^2). The PDMS microfluidic channel is composed of a single inlet, a single outlet, and four parallel microchannels that

connect the inlet and outlet (Fig. S5). The width and length of the microchannel is 1 mm and 14 mm, respectively. The PDMS microfluidic channel was fabricated using a conventional soft lithography process (REF). First, the master mold was made of a 20 μm thick layer of SU-8 2025 photoresist (Kayaku advanced materials, USA) patterned on a 3-inch silicon wafer. This SU-8 master mold was then coated with tridecafluoro-1, 1, 2, 2-tetrahydrooctyl-1-trichlorosilane (United Chemical Technologies, Inc., Bristol PA) to facilitate release of the replicated PDMS microchannel layer (10:1 mixture, Sylgard 184, Dow Corning, Inc., MI). After oxygen plasma treatment of both the PDMS layer and the glass substrate, they were bonded together for 24 h at $80^0 C$.

5. Operation of the microfluidic system for Mtb cell capture

A stack of 10 neodymium-iron-boron (NeFeB) permanent magnets (K&J Magnetics, Inc., USA), generating an external magnetic flux of 1.3 T, was placed underneath the magnetophoretic device and placed in parallel arrangement about the flow direction (Fig. S5(B)). When the prepared sample was flowed into the microchannel, Mtb cells covered with the combination of tail fiber protein and MB were attracted towards the bottom substrate where the magnetic field is strongest and held on the substrate during the separation process. Other debris and undesirable substances in the sample were washed away during the washing process. A Zeiss Axio Observer Z1 microscope (Carl Zeiss Micro Imaging, LLC) with a 20x magnitude lens was used to count the number of Mtb cells in the microchannel using mCherry (excitation: 587 nm, emission: > 610 nm).

6. Bacterial cell enumeration for the measurement of the capture efficiency of the microfluidic device

The Mtb (mCherry MC^{2}7000) cells were grown in a shaker incubator for one week at 37°C in 7H9/OADC media. In order to obtain a single-cell suspension, bulk culture was sonicated for 10 s, filtrated using 5 µm filter (VWR), and centrifuged at maximum rpm. The cell pellet was suspended in 1 mL of 7H9-ADC media and then diluted 100 times. 5 µL of the cell solution was dropped on a glass slide and a cover glass (18 by 18 mm) was placed on the solution. A Zeiss Axio Observer Z1 microscope with a 20x magnitude lens was used to count the number of Mtb cells using mCherry. After cell counting, cell concentration with 1000 cells mL^{-1} was prepared and plated on agar for off-chip cell counting. This experiment was repeated three times and we confirmed that about 1000 cells were found on each agar plate, which demonstrates that the cell counting is quite accurate to be used for the sample preparation with different cell concentrations. A certain amount of the prepared Mtb cell solution was added in 1 mL of 7H9-ADC media, which have different initial cell concentrations from about 500 to 10000 cells mL^{-1}. The Mtb cell clumps used for Ziehl-Neelsen staining were prepared separately by sonication for 10s and vortex for 10s without filtration. After that, the prepared Mtb cell clumps with different concentrations of about 1000, 3000, 5000, and 10000 cell clumps mL^{-1} were added in 1 mL of an artificial sputum solution (ClaremontBio). In the case of cell counting of *E. coli*, after *E. coli* overnight culture, the cell concentration was measured using an optical density meter (600 nm, OD$_{600}$). Based on the assumption that OD$_{600}$ of 1.0 has an *E. coli* concentration of 10^9 colony-forming unit (CFU) mL^{-1}, the cells with about 10^4, 10^5, and 10^7 cells mL^{-1} were prepared for test.

7. Ziehl-Neelsen Staining

250mM Immidazole was added to the sample collected from the microfluidic device to separate tail fibers from magnetic beads. The beads were pulled asides with a magnetic microcentrifuge rack and the remainder of the sample was collected. 10μl was smeared on a slide and air dried. The smear was then flooded with Ziehl-Neelsen Carbolfuchsin solution (Sigma Aldrich) and heated above a steaming water bath for five minutes.. The slide was then rinsed with water and decolorized with acid-alcohol (1% HCl in 95% etOH).Since our samples only contained Mtb cells the counter stain was omitted. . Slides were imaged with a 100X optical lens on a Nikon Diaphot-TMD Microscope. Images were captured with an Omax A3RDF50 Camera using ToupView software. For the sensitivity experiments, up to 300 random fields of view were observed, and the number of frames containing Acid fast positive cells were counted. For higher cell concentrations the number of frames to observes five positive fields of views were counted and extrapolated to 300 frames.

8. On-chip binding stability test

The device fabrication was described above. Here, the master mold made of a 0.9 μm thick layer of SU-8 2002 photoresist was used. *M. smegmatis* with the cell concentration of 10^7 cells mL^{-1} was injected into the device at a flow rate of 5 ul h^{-1} for an hour and trapped in a 0.9 μm channel. Next, the tail fiber protein with 0.25 mg mL-1 was injected

into the device at a flow rate of 5 ul h^{-1} for 3 h, and then 7H9-ADC media was injected into the device at the same flow rate to remove dead cells, debris and residue of tail fiber protein. The cells were incubated in the channel overnight at 37℃. A Zeiss Axio Observer Z1 microscope with a 100x magnitude lens was used for time-lapse imaging using GFP (excitation: 488 nm, emission: > 510 nm).

9. On-chip TB cell separation

A syringe pump continuously provided controlled flow through the inlet to the microchannel and the sample flow rate was set to be 200, 300, 400, and 500 μL h^{-1}. A magnet was placed underneath the device and high-gradient magnetic fields were generated in the microchannel, Subsequently, the prepared Mtb cells suspended in 1 mL^{-1} of 7H9-ADC media or the artificial sputum solution were flown through the device, captured on the microchannel, and imaged with a microscope for cell counting.

CHAPTER 3

SYNTHETIC LETHALITY OF PEPCK INHIBITORS DURING BEDAQUILINE

EXPOSURE

Introduction

Central carbon metabolism is a crucial biochemical pathway in most living things. Its role is to convert nutrients into energy, most commonly in the form of ATP, or into biomass. It comprises of multiple pathways, each contributing to the cell's metabolism based on its environment and nutrients. Some of the more important central carbon metabolism pathways are Glycolysis (Entner-Doudoroff Pathway), Gluconeogenesis and the citric acid cycle (also known as TCA or Krebs cycle). Understanding these pathways, and their role within Mtb is crucial in order to develop inhibitors that could have anti-mycobacterial activity.

Glycolysis is a multi-enzyme pathway that breaks down glucose into two pyruvate molecules, while generating two net ATP molecules and two NADH molecules, which will be used to generate additional ATP molecules through oxidative phosphorylation. Glucose is believed to play a role *in vivo* since a double mutant of Mtb's glucokinase, which renders the bacteria unable to utilize exogenous glucose, reduced the ability of the infection to persist in the lungs(53). Glycolysis is also the pathway of central carbon metabolism where glycerol enters. Glycerol is a common carbon source used for growing Mtb cells in cultures as it grows the fastest in its presence(54). The biological relevance

of glycerol as a carbon source is however disputed. While the evidence that a gene critical for the utilization of glycerol as a carbon source is non-essential for Mtb growth in murine model(55) supports the notion that glycerol is not an important carbon source, there is also evidence suggesting that glycerol can be found in human-like lung lesions in mice(56), indicating that the bacteria could have access to its preferred *in vitro* carbon source. Glycolysis is a biochemical process that can typically operate aerobically or anaerobically. In the absence of Oxygen, pyruvate will be fermented into lactate by the enzyme lactate dehydrogenase (LDH). However, Mtb does not have a fermentative LDH, capable of interconversion between pyruvate and lactate. Rather, Mtb contains a putative quinone dependent LDH enzyme, able to irreversibly oxidized L-lactate into pyruvate(57).

The citric acid cycle is most commonly known as the TCA or Krebs cycle. When combined with oxidative phosphorylation, it is the most energetically efficient pathway of central carbon metabolism. The TCA cycle is a multi-enzyme cyclic pathway which generates NADH that can later be used to create ATP by the electron transport chain and ATP synthase, using oxygen as a terminal electron acceptor.

The TCA cycle does have a few alternative branches than the "standard" cycle. One of such variations that is very prominent in Mtb is the glyoxylate shunt. The shunt is essentially a shortcut between isocitrate and malate/succinate. The enzyme isocitrate lyase (Icl1) is responsible for breaking down isocitrate into succinate and glyoxylate. While the succinate can re-enter the TCA cycle, the resulting glyoxylate will be used as substrate for malate synthase, which will convert the glyoxylate into malate, which in turn can re-enter the TCA cycle. The glyoxylate shunt allows the cell to bypass two NADH and

carbon dioxide producing steps of the citric acid cycle. This allows the bacteria to reduce production of NADH, which can cause redox imbalance in low oxygen, yet still allow gluconeogenesis to occur and utilization of fatty acid carbon sources for biomass production. There is also evidence suggesting that glyoxylate accumulation is toxic to the bacteria, indicating that both ICL and MS have critical roles(58).

While even chain fatty acid can be metabolized via β-oxidation into acetyl-CoA, catabolism of odd chain fatty acids and cholesterol both result in the production of propionyl-CoA, which unlike acetyl-CoA cannot enter the Krebs cycle directly. Indeed, propionyl-CoA requires another alternative branch of the TCA cycle known as the methylcitrate cycle. Interestingly, the enzyme Icl1 participates in both the glyoxylate shunt and the methylcitrate cycle, acting as both an isocitrate lyase (ICL) and a methylisocitrate lyase (MCL), which is otherwise lacking in the Mtb genome(59). Birefly, the cycle starts with methylcitrate synthase, which catalyzes the reaction between oxaloacetate and propionyl-CoA, producing methylcitrate and CoA. The final step of this cycle is carried out by the MCL enzyme, resulting in the production of succinate and pyruvate. Similarly to the glyoxylate shunt, the methylcitrate cycle utilizes and produces molecules involved in the TCA cycle, thus making both of these distincts pathways connected to the citric acid cycle.

Gluconeogenesis is a multi-enzyme pathway responsible for the generation of glucose from fatty acid carbon sources. Many of the enzymes that are part of this pathway are bi-directional and are therefore shared between glycolysis and gluconeogenesis. There are

however some key enzymes in glycolysis that are non-reversible and must be bypassed in gluconeogenesis. These enzymes are hexokinase, phosphofructokinase and pyruvate kinase. They are bypassed by glucose-6-phosphatase, fructose-1,6-bisphosphatase and phosphoenolpyruvate carboxykinase (PEPCK) respectively.

PEPCK is the first committed step of this process and is a crucial enzyme for this biochemical process to occur. Although it is primarily known for its central role in gluconeogenesis, PEPCK is capable of catalyzing the interconversion of oxaloacetate and phosphoenolpyruvate and is thus reversible. In Mtb, phosphoenolpyruvate carboxykinase (pckA) has been shown to be essential for growth on strict fatty acid carbon source. Additionally, it has also been demonstrated to be essential to establish and maintain infection in murine model(60). Fatty acid is believed to be a primary carbon source utilized by Mtb *in vivo*. This was demonstrated by Segal and Bloch in 1956 when they discovered that bacteria isolated from infected lungs preferentially grew on fatty acid *ex vivo*. Additional research demonstrated that genes involved in fatty acid metabolism were significantly upregulated during infection(61, 62), solidifying the hypothesis that fatty acids play a significant part in Mtb metabolism.

Additionally, PEPCK has been linked to a variety of other important cellular pathways that may be contributing to its essentiality. One of such pathway is the GAS pathway, named as such because it relies on the Glyoxylate shunt, Anaplerotic fixation of carbon dioxide and eventual generation of succinyl CoA by Succinyl CoA synthase(63). The GAS pathway is believed to be responsible for pyruvate dissimilation. Another pathway implicating PEPCK is the Reductive TCA cycle. The reductive TCA cycle pathway is believed to mainly be utilized under hypoxia(64). Although Mtb is an obligate aerobe, it is

able to survive at very low oxygen concentration and the reductive TCA pathway could be a contributing factor. When oxygen is low, oxidative phosphorylation slows down, because there is a lack of terminal electron acceptor and this leads to an accumulation of NADH. This accumulation is deleterious to the cell as the NADH:NAD$^+$ ratio is critical for cell to maintain proper redox balance and viability. In fact, redox imbalances are used in many *in vitro* cell viability assays such as Alamar Blue (Rezasurin). The reductive TCA cycle is believed to reduce the NADH:NAD$^+$ ratio by utilizing enzymes that convert NADH to NAD$^+$ such as malate dehydrogenase, fumarate reductase and malic enzyme(64). The reductive TCA pathway ultimately leads to the secretion of succinate, which has been observed under low oxygen tension. Interestingly, both the GAS pathway and Reductive TCA explain accumulation of secreted succinate, which is believed to play a role in maintaining membrane potential(64).

For all these reasons, PEPCK has become a very attractive target for the development of anti-mycobacterial drugs. Prior work in our laboratory has laid the groundwork for further development of inhibitors(65). Our lab established a biochemical assay to measure PEPCK enzyme activity *in vitro*. We were also able to identify a potent lead molecule that showed significant enzyme level inhibition, despite a lack of whole cell activity, even on a strict fatty acid carbon source (Figure 10, page 62). The lead molecule consisted of a previously identified inhibitor of human cytosolic phosphoenolpyruvate carboxykinase (cPEPCK), known as Axon 1165. The discovery of this inhibitor was made by a group of scientists at Roche, published in three sequential papers(66-68). The

xanthine-based molecule was previously shown in our lab to also be active on Mtb PEPCK, and thus became the backbone for structure activity relationship studies (SAR). One area of major concern with the Axon 1165 compound is that it was developed as an inhibitor of human cPEPCK, meaning that although it can also inhibit the mycobacterial enzyme, it will most definitely have off target effect on the human orthologues, which could lead to cytotoxicity of the compound. Creating specificity was thus a crucial element of the work performed prior to this dissertation.

Our group was able to create this specificity by taking advantage of slight variations in the protein sequence, specifically in the active site. Since the lead molecule is a GTP competitive inhibitor, this is where it will bind. When the structures of human cPEPCK and Mtb PEPCK are overlaid we can notice very little variation between the two orthologues, but one significant difference is that the residues corresponding to methionine 296 of the human enzyme is replaced by leucine 281 in the mycobacterial enzyme (Figure 11, page 63). The methionine residue is much bulkier than the leucine residue from the mycobacterial orthologue. As such this difference was exploited to increase inhibitor specificity towards the bacterial target. This was achieved by expanding of the N1 functional group, thus creating steric hindrance between the inhibitor and the human cPEPCK. Using this approach, inhibitor PEPCK-0057 displayed an IC_{50} 16 times lower towards the pathogenic orthologue than its human counterpart(65) (Figure 11, page 63). Unfortunately, up to this point, none of the inhibitors in our collection displayed any whole cell activity, despite the restricted carbon source present in the culture media. Multiple factors could contribute to this phenotype. Some targets require a very high level of inhibition in order to cause cell death. Some other possibilities include a lack of

bioavailability of the molecule, preventing it from reaching a high enough cellular concentration to kill the mycobacteria. Whatever the case may be, expanding our collection of PEPCK inhibitors was crucial in order to help us understand what is going on, and potentially obtain whole-cell active compounds.

Expanding the Collection of PEPCK Inhibitors

The lack of whole-cell activity of the inhibitors of PEPCK that were previously identified in the laboratory was concerning, but not entirely unexpected. We thus needed to continue the lead optimization of the xanthine-based inhibitor series in order to push both potency against the enzyme, as well as specificity towards the Mtb orthologue of PEPCK.

The enzyme assay was previously established in our laboratory. Briefly, the assay is a pyruvate kinase (PK) and lactate dehydrogenase (LDH) coupled assay, where PEPCK is the rate limiting step. We measured the decrease of absorbance at a 340nM wavelength, which is the absorbance peak for NADH. Since LDH converts pyruvate to lactate while producing NAD^+ from NADH, the rate of decrease of absorbance at 340nM correlates with the rate of activity of the LDH enzyme. As the coupled enzymes are in excess, the activity level of LDH is dependent upon the amount of pyruvate, which in turn depends on the amount of PEP. Since the conversion of Oxaloacetate (OAA) to PEP is catalyzed by PEPCK, and that it is the rate limiting step of the whole reaction, the rate of decrease of absorbance at 340nM is correlated with the level of activity of PEPCK. As such, reduction of the negative slope represents inhibition of PEPCK.

We expanded our collection of PEPCK inhibitors by testing 44 additional compounds that were based around the Axon-1165 lead molecule (Table 1, page 64). The compounds were designed in collaboration with the TB Alliance and synthesized by Wuxi. To measure the level of inhibition for each compound we used a dose response in order to calculate the IC_{50} of the molecule. The highest concentration used was 20μM and the compounds were diluted 2-fold between concentrations. The lowest concentration was approximately

20nM. Since each compound was part of the same series, which had already shown significant inhibition, most compounds tested retained inhibitory activity against Mtb PEPCK. The most potent IC_{50} values calculated were around 40nM. Seven compounds tested had IC_{50} below 100nM, with an additional 14 displaying sub micromolar IC_{50} (Table 1, page 64). Unfortunately, the activity against the human cPEPCK correlated closely with activity against the mycobacterial enzyme. Although the selectivity remained present for most compounds, the magnitude of the selectivity remained similar to that of previous compounds, ranging between 5 and 30-fold specificity. Table 2 (page 67) provides structural information for some of the PEPCK inhibitors that are used or referenced in this work.
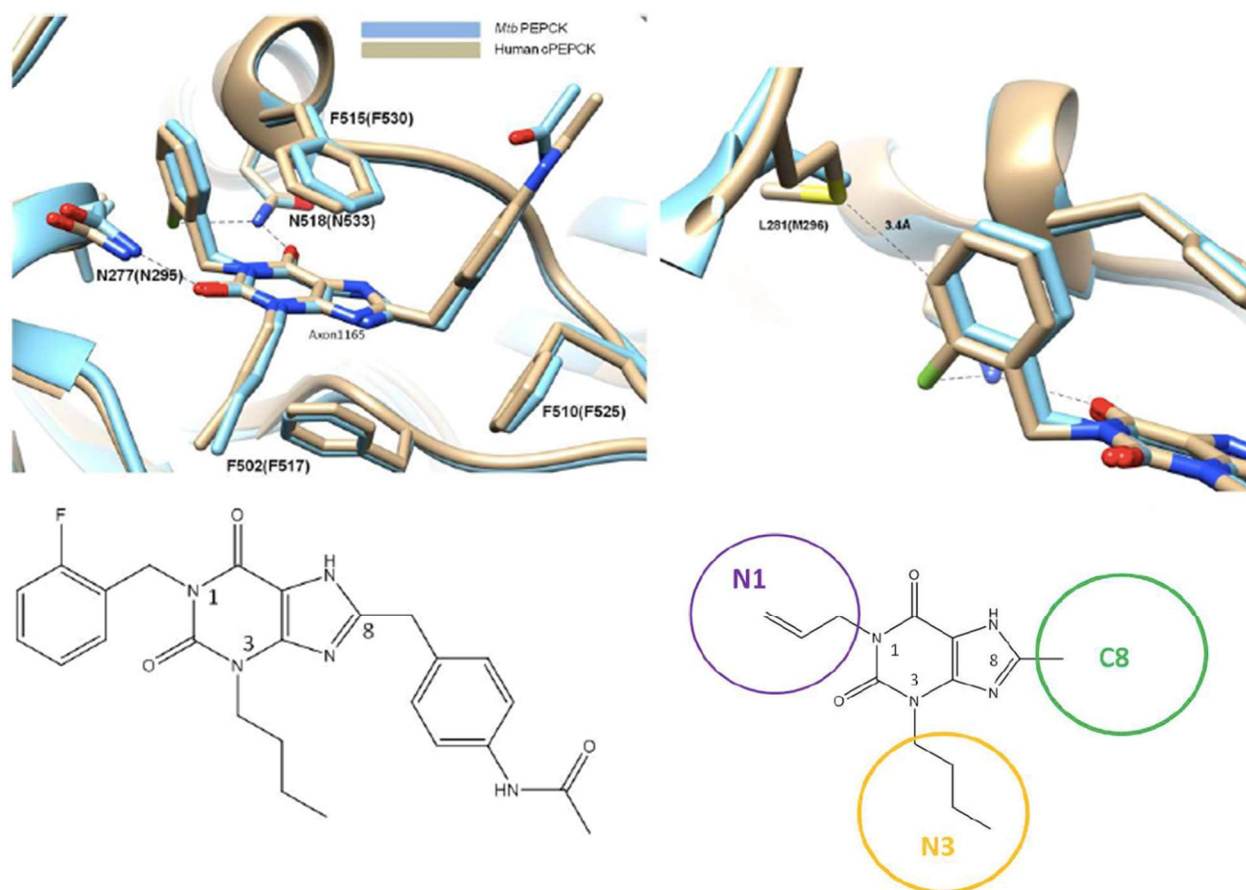
Figure 10 Development of lead PEPCK inhibitor molecule, based on Axon-1165, an inhibitor of cytosolic PEPCK

Crystal structures of Mtb PEPCK (A&B, Light Blue) and Human PEPCK (A&B, Beige) bound with Axon 1165 (C). Xanthine core of the PEPCK inhibitor lead molecule, with identified groups used for SAR studies. (D)

*Reprinted from the doctoral thesis of Haelee Kim, "Structure-guided Inhibitor Design of Mycobacterium Tuberculosis Drug Targets from Central Carbon Metabolism", 2016, Department of Chemistry, Texas A&M University
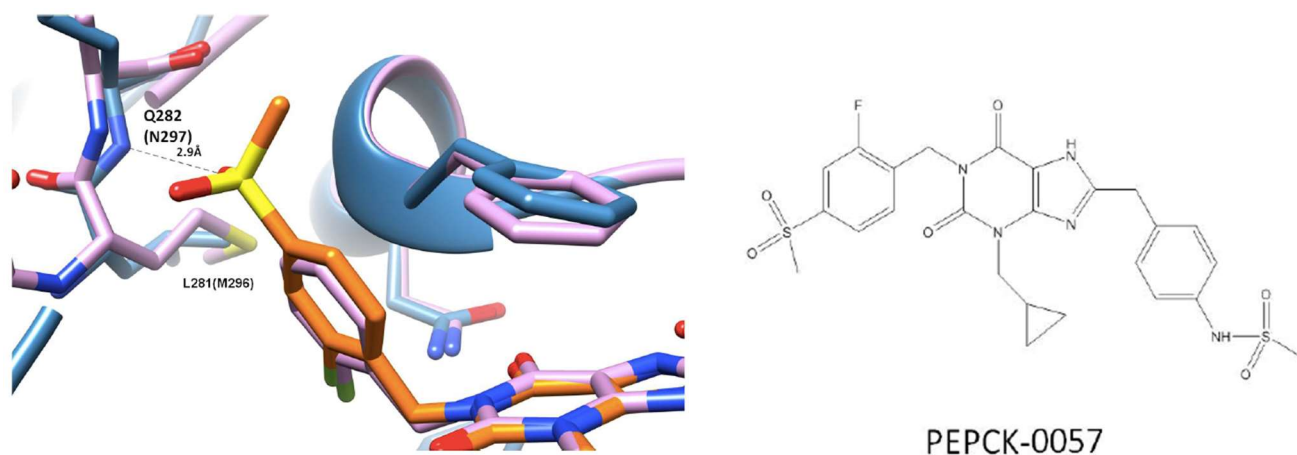
PEPCK-0057

IC$_{50}$ (nM)	Human PEPCK	Mtb PEPCK
PEPCK-0057	3394	200

Figure 11 Development of inhibitory specificity towards mycobacterial PEPCK through modification of N1 group

Crystal structure of Mtb PEPCK (A, Blue) bound with PEPCK -0057 (B), overlayed on the crystal structure of Human cPEPCK (A, Light Pink), shows potential steric hindrance between PEPCK inhibitor and Methionine 296 of human cPEPCK, creating inhibitor specificity as shown in C.

*Reprinted from the doctoral thesis of Haelee Kim, "Structure-guided Inhibitor Design of Mycobacterium Tuberculosis Drug Targets from Central Carbon Metabolism", 2016, Department of Chemistry, Texas A&M University

Table 1.

Compound ID	IC$_{50}$ Mtb PEPCK(nM)	IC$_{50}$ Human cPEPCK(nM)
PEPCK-0087	702.5	680.7
PEPCK-0088	3548	1625
PEPCK-0093	2017	>20000
PEPCK-0106	854.7	9350
PEPCK-0107	389.9	>20000
PEPCK-0108	1567	>20000
PEPCK-0109	373.6	16288
PEPCK-0109A	2578	>20000
PEPCK-0113A	4389	>20000
PEPCK-0114	10894	>20000
PEPCK-0115	>20000	>20000
PEPCK-0120	1047	>20000
PEPCK-0121	>20000	>20000
PEPCK-0121	169476	>20000
PEPCK-0123	3403	>20000
PEPCK-0125	1670	>20000
PEPCK-0126	70.81	937.4
PEPCK-0127	41.28	538.5

Table 1 Continued

Compound ID	IC$_{50}$ Mtb PEPCK(nM)	IC$_{50}$ Human cPEPCK(nM)
PEPCK-0128	94.64	411.1
PEPCK-0129	44.25	606.7
PEPCK-0130	106.7	3618
PEPCK-0131	40.13	1251
PEPCK-0132	630.9	6727
PEPCK-0133	1086	>20000
PEPCK-0135	280.3	5411
PEPCK-0136	336.5	2200
PEPCK-0137	1226	5356
PEPCK-0138	5600	>20 000
PEPCK-0139	17564	>20000
PEPCK-0140	15134	>20 000
PEPCK-0141	>20000	>20000
PEPCK-0142	63.5	522.7
PEPCK-0143	93.33	931
PEPCK-0144	272	2077
PEPCK-0145	527.6	2392
PEPCK-0146	816.5	10202
PEPCK-0147	12093	>20000

Table 1 Continued

Compound ID	IC$_{50}$ Mtb PEPCK(nM)	IC$_{50}$ Human cPEPCK(nM)
PEPCK-0148	7369	>20000
PEPCK-0149	3538	>20000
PEPCK-0150	>20000	>20000
PEPCK-0151	>20000	>20000
PEPCK-0152	>20000	>20000
PEPCK-0153	197.7	2483
PEPCK-0154	157.4	1600

Table 1. Enzyme inhibition Data of compounds against *Mycobacterium tuberculosis* PEPCK and human cytosolic PEPCK

IC$_{50}$ measured by enzymatic assay for compounds derived from the lead molecule Axon 1165. Each IC$_{50}$ was calculated by Graphpad Prism, from duplicate data. Light green represents sub micromolar IC$_{50}$ against Mtb PEPCK, dark green represents IC$_{50}$ below 100μM against Mtb PEPCK, Red represents sub micromolar IC$_{50}$ against human cPEPCK. Highest concentration tested was 20μM, therefore were represented as >20μM.
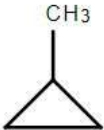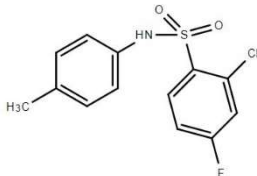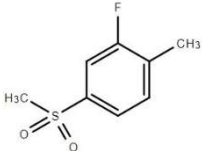
Table 2.
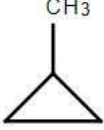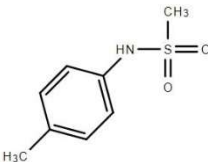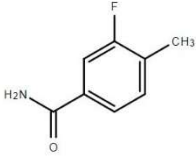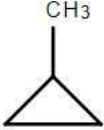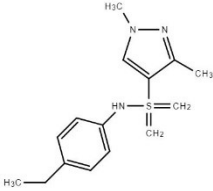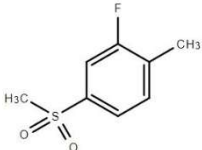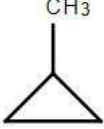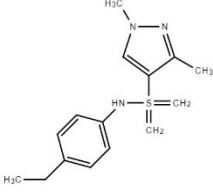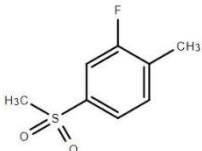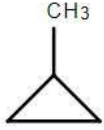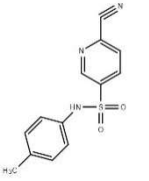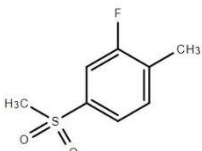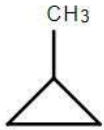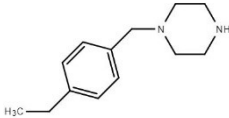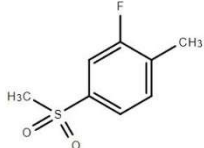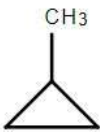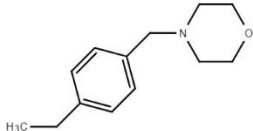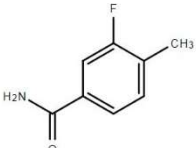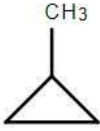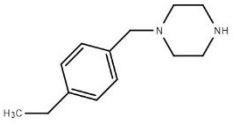
Compound ID	N1	N3	C8	Mtb PEPCK IC$_{50}$(nM)	Human cPEPCK IC$_{50}$(nM)
PEPCK-0001				440	200
PEPCK-0057				200	3394
PEPCK-0128				94.64	411.1
PEPCK-0129				44.25	606.7
PEPCK-0131				40.13	1251
PEPCK-0135				280.3	5411

Table 2 Continued

Compound ID	N1	N3	C8	Mtb PEPCK IC_{50}(nM)	Human cPEPCK IC_{50}(nM)
PEPCK-0136				336.5	2200
PEPCK-0144				277	2077

Table 2. Structure Activity Relationship of PEPCK Inhibitors

Structure of PEPCK inhibitors used or mentioned in the thesis. The structural information of each compound is broken down to the three groups identified previously (N1, N3, C8), while the xanthine core remains intact. The IC_{50} was calculated by the enzyme assay described in the thesis and is represented in nM.

Whole-Cell activity of PEPCK inhibitor in the presence of Bedaquiline

Unfortunately, despite compounds showing high potency against the target enzyme, whole-cell activity remained elusive, even on strict acetate carbon source. We thus decided to test the efficacy of the compounds on whole cells in combination with Bedaquiline (BDQ), an FDA approved anti-mycobacterial drug which inhibits ATP synthase. The wide-ranging effect of BDQ exposure on other central carbon metabolism and oxidative phosphorylation pathways had previously been found(69, 70). We thus hypothesized that if compounds were able to enter the bacteria and inhibit PEPCK, we may be able to see an effect in the presence of BDQ.

We tested this hypothesis by using a drug combination checkboard assay, where one drug is serially diluted along the x axis of the plate, while the other drug is serially diluted along the y-axis. We used the Resazurin/Resorufin viability reporter dye. Briefly, resazurin, which is blue, is converted to resorufin, which is pink, by NADH. Since NADH production is connected to cellular respiration, this technique is a well validated assay to test for bacterial cell growth. We first selected the original lead molecule Axon-1165 for this checkboard experiment. The results (Figure 12, page77) showed, as expected, that any concentration of the PEPCK inhibitor failed to show any whole cell growth inhibition. Meanwhile, the dose response to BDQ alone also behaved as expected and displayed sigmoidal inhibition response. The most intriguing part of the results was that at lower concentrations of BDQ (50nM and 25nM) we could see a clear dose response to increasing concentrations of PEPCK inhibitor until approximately 6.125µM of Axon-1165.

The growth inhibition fell back down at higher concentrations, indicating solubility issues with the compound at those concentrations. These results seem to indicate that BDQ exposure leads to synthetic lethality of PEPCK inhibitors. However, from this experiment alone, we could not eliminate the possibility that this phenotype was due to off-target effect of the inhibitor and was unrelated to the compound's inhibitory activity against PEPCK.

In order to test whether this observation was due to the chemical inhibition of PEPCK with Axon-1165, we decided to measure the whole cell potency of various compounds from our collection. Our hypothesis was that if this phenotype was due to inhibition of PEPCK, the potency of the compound against the whole cell in the presence of BDQ should strongly correlate with its *in vitro* potency against the enzyme. We selected five inhibitors with IC_{50} ranging from 40nM to 1.5µM. Each PEPCK compound selected was serially diluted with the highest concentration being 100µM. To each serial dilution we either added DMSO or 20nM BDQ. We chose this concentration of BDQ for our experiment because, based on the previous results, it is a concentration at which BDQ alone seems to have very little activity on cell growth, but growth inhibition was visible when PEPCK inhibitors were added.

Using the same resazurin dye as previously used, we measured the growth inhibition for each individual well and used these results to calculate the whole cell MIC_{50} in the presence of 20nM BDQ. We were then able to compare the previously established IC_{50} value of each compound with their newly obtained MIC_{50}. The results (Figure 13, page 78-80) clearly showed a strong linear correlation between the two inhibition measurements (R^2 = 0.966). Taken together, these results strongly suggest that the

potency of the observed synthetic lethality is proportional to the level of inhibition of PEPCK and is therefore consistent with a causal relationship.

Although synthetic lethality of PEPCK inhibitors can be seen in the presence of BDQ by using the resazurin viability assay, this does not necessarily mean that cells are actually dying. Indeed, resazurin is only a reporter of cell viability and, although generally considered to be well validated, it can sometimes lead to false positives or false negatives. To confirm that cell growth was truly inhibited by the combination of the two drugs, we decided to use the gold standard of whole cell growth inhibition assays: CFU-based time-kill kinetics. Briefly, a single concentration of each drug is added to a liquid bacterial culture and grown for 21 days. At predetermined time intervals, a small volume is taken out of the culture bottle and plated on nutrient rich plates containing no drug. These plates are then incubated for 4 weeks, or until colonies become visible. The colonies are then counted, and the cell concentration of the initial sample is calculated. This approach has two major advantages over resazurin based assay. Firstly, this method is based on colony forming units, as such the number of viable bacilli is not inferred, but actually counted. This eliminates any false positive or negative based on interference with the reporter dye. Secondly, the resazurin assay can only measure inhibition of growth. The initial concentration of cells in the assay is too small to provide a detectable signal, therefore we cannot differentiate between bacteriostatic activity (Inhibition of growth) and bactericidal activity (Decrease in viable cells i.e.. killing cells).

There is however one very significant downside to this approach, and that is the extensive nature of this method. Time-kill kinetics required each time point to be plated out for colony enumeration. However, since the actual number of colonies expected is unknown

at the time of plating, each time point must be serially diluted to insure at least one countable plate (Typically 50-400 colonies per plate). Furthermore, such experiment must be done at least in triplicates due to the significant variability of such experiment. Additionally, since we were mostly interested in the effect of the combination of two drugs, each single drug experiment also had to be performed in addition to the drug combination. The experiment thus consisted of 12 different cultures, each one was counted at 5 different time points (Day 0, 3, 7,14 and 21) and each data point was plated from three different culture dilutions for a total of 180 plates per experiment. Additionally, because Mtb grows very slowly, the experiment takes over 2 months to complete.

We performed the time-kill kinetic experiment at two different concentrations of BDQ; 50nM and 150nM (Adding an additional 90 plates). These concentrations were chosen because they respectively represent sub-inhibitory and inhibitory concentrations of BDQ, allowing us to evaluate the effect of our PEPCK inhibitor under two different levels of BDQ exposure. We chose to use PEPCK-0136 for this experiment due to the fact that it's pharmacokinetic/pharmacodynamic properties, which were performed by our collaborators at the TB Alliance, were relatively good compared to other compounds (data not shown). Due to the work intensive nature of the time-kill kinetic approach, we wanted to select one of the compounds that had the best PK/PD profile which could then eventually be used in a potential efficacy study in animals.

Before the experiment could be performed, we also had to select the right concentration of PEPCK-0136 to use. We decided to assess the effect of various concentration of the PEPCK inhibitor on the potency of BDQ by using resazurin viability assay. Briefly, we measured the MIC_{50} of BDQ in the presence of 0, 0.5, 1, 5 and 10 μM of PEPCK-0136

and compared the dose response curves. What the results (Figure 14, page 81) show is that there is a slight shift in BDQ potency at 5 and 10µM, while the dose response curve of BDQ in the presence of 0.5 and 1 µM closely matched the BDQ dose response curve when no PEPCK-0136 is present. Although the results from this experiment alone do not allow us to make conclusions about the synergistic interactions between these two drugs, which was not the intent, we believe it provided us with a good starting point in terms of how much PEPCK-0136 we should use in the time-kill kinetic experiment. Indeed, since the shift in dose response curve seems to happen between 1 and 5 µM, while further increase to 10 µM seem to have no additional effect, we decided to use a concentration of 5 µM.

The results from the 150nM BDQ experiment (Figure 15, page 82) show that without BDQ, PEPCK-0136 had no effect of growth, as the arm containing only PEPCK inhibitor grew exponentially at the same rate as the DMSO control. The results also seem to show an increase in bactericidal activity due to the addition of PEPCK-0136 inhibitor. By day 7, the number of CFU in the drug combination arm was on average 10 fold lower than in the BDQ alone arm of the experiment. This trend remained unchanged at day 14, with the drug combination once again having on average 10 times less CFUs. By day 21 both cultures, BDQ and BDQ/PEPCK-0136, had fallen below the detection threshold. Asides from day 3, where the drug combination had on average 3.5 times fewer CFUs than BDQ alone, statistical analysis was unable to find statistically significant differences between the two arms. Unfortunately, we cannot make any definitive conclusions from this experiment, as it was underpowered, which is not unusual for this type of assay, which has intrinsically high variance in the data, which can be difficult to overcome. That being

said, at day 14, the replicate with the most CFUs from the drug combination arm still had 4 times less CFUs than the replicate with the fewest CFUs from the BDQ alone arm. Taken together, these results seem to indicate that addition of 5µM PEPCK-0136 enhances bactericidal activity of inhibitory concentrations of BDQ, despite PEPCK inhibitors having no effect on growth on their own. However, no definitive conclusions can be made from these results alone, as the study was underpowered and could not establish definitive statistical significance.

In the experiment with sub-inhibitory concentrations of BDQ, the arm containing BDQ alone, unlike the prior experiment, was able to grow. The results (Figure 16, page 83) seem to show a slight lag period in the first 7 days, however by day 14 it had grown to the same concentration as the control arm. This was expected, as the concentration of BDQ was greatly reduced and was below the threshold required for BDQ to inhibit cell growth. The interesting part of this experiment comes from the combination of the two drugs. In the first 7 days, each triplicate behaved similarly, seemingly inhibiting bacterial growth, but without any cell death. However, at days 14 and 21, the replicates had seemingly started to diverge from one another. By day 21, the number of CFUs of the first replicate had gone down ~10 fold, the second replicate ~100 fold and the last replicate ~1000 fold from the original concentration. Meanwhile the BDQ alone had continued to grow, with the number of CFUs 100 fold greater at day 14 than on day 0. Unfortunately, the plates containing CFUs for day 21 were contaminated and could not be counted. The very large variability between the experimental replicates of the drug combination and the lack of results for day 21 of BDQ only arm made statistical analysis a little more

complicated. However, despite the large variation between replicates, the drug combination showed a statistically significant (P=0.0053) reduction in CFUs when compared to BDQ alone on day 14. Additionally, we believe the divergence of the triplicates could provide additional insight. The large divergence between the experimental replicates is somewhat strange but could potentially be explained in a few different ways. It has been shown with other drugs that the size of the inoculum can significantly affect the efficacy of drugs. In other words, if replicate had slightly different original concentration, it could affect not only the starting point, but also drug potency. Furthermore, we could have selected a drug concentration that corresponds to the inflection point of the dose response curves. If this was the case, a very small difference in drug concentration between the replicates could have a large effect of growth inhibition, which could potentially explain the observations in Figure 16 (page 83).

Sub- Chapter Summary

Taken together, these results support the hypothesis that chemical inhibition of PEPCK is synthetically lethal to cells exposed to low doses of Bedaquiline. We were able to demonstrate that, in the presence of 20nM BDQ, PEPCK inhibitors were able to inhibit growth of Mtb cells in a dose dependent manner. The potency of these inhibitors on whole cells was proportional to the potency of these inhibitors on the PEPCK enzyme, strongly suggesting that the observed phenotype was at least partially caused by inhibition of PEPCK, as with any chemical inhibition, some level of off-target effect cannot be dismissed. We also demonstrated that at inhibitory concentrations of BDQ, addition of

PEPCK-0136 was seemingly able to further reduce CFUs by 10-fold, however the experiment was underpowered and our results were not found to be statistically significant. Our results did however demonstrate that addition of PEPCK-0136 to sub-inhibitory concentrations of BDQ was able to significantly reduce the number of CFUs in liquid culture and that the combination of the two drugs at the concentrations used was bactericidal, despite both drugs having no effect on growth when used individually.
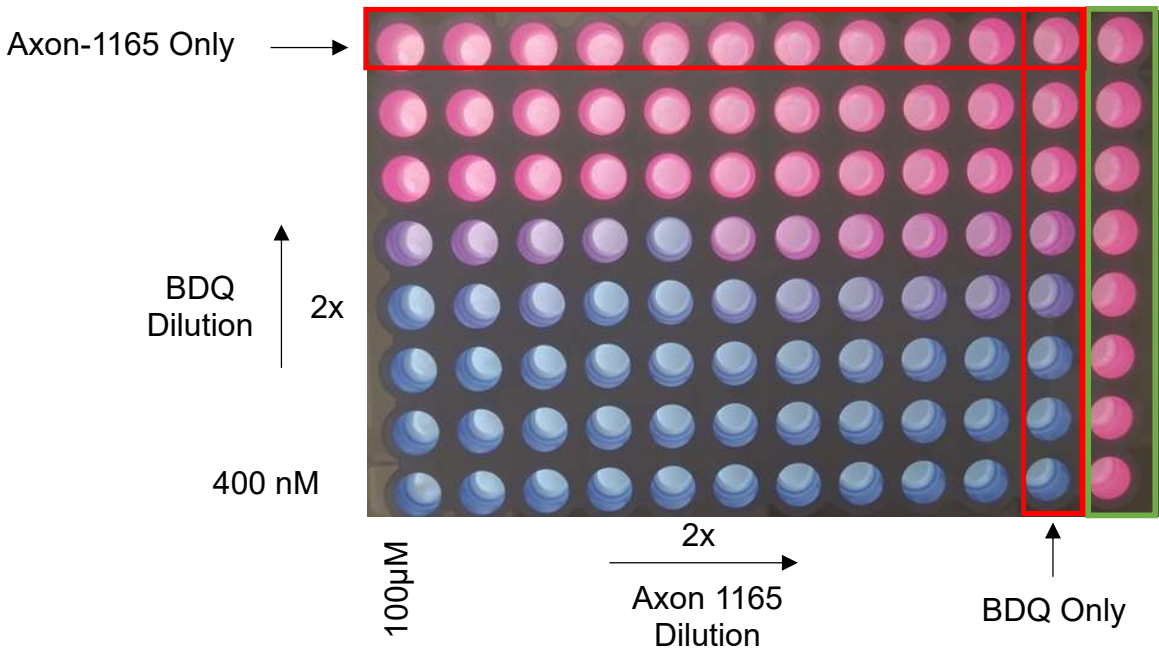
Figure 12. Checkboard Assay Shows Dose-Dependent Whole Cell Growth Inhibition of Axon-1165 in the Presence of BDQ

Checkboard assay using resazurin as viability reporter. Growing cells convert resazurin (blue) into resorufin (pink). Each drug was serially diluted along one axis, Axon 1165 horizontally and BDQ vertically. Green marked column is a DMSO control, Red Column is a BDQ only control, horizontal Red column is the Axon-1165 only control. Highest BDQ concentration was 400nM, starting at the bottom of the plate and diluted 2X upwards. The highest concentration of Axon-1165 was 100µM, starting on the left side of the plate and diluted two-fold towards the right.
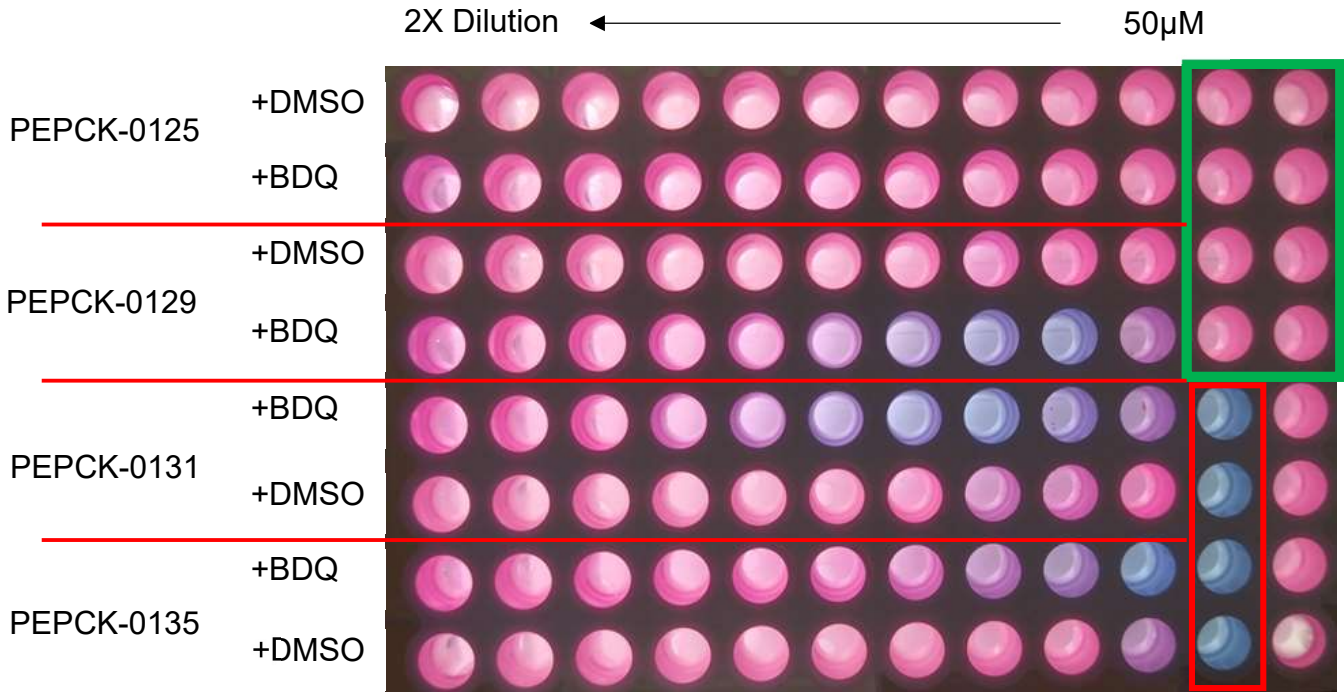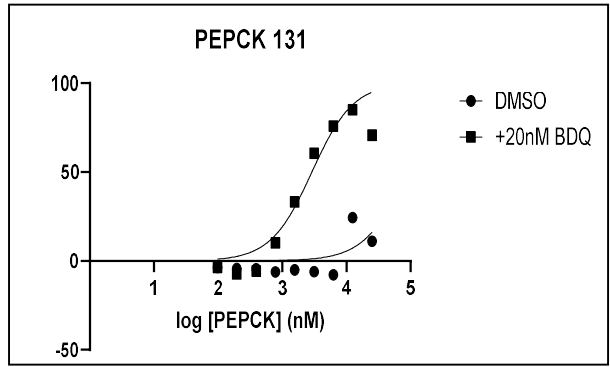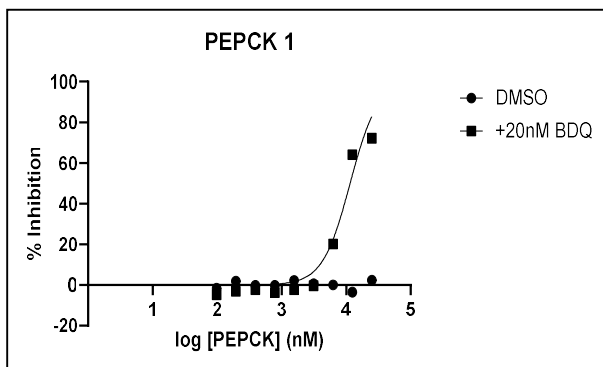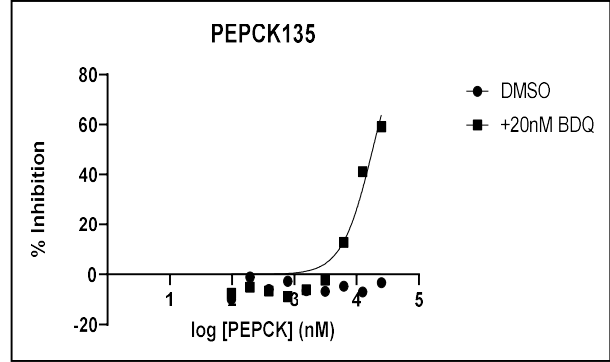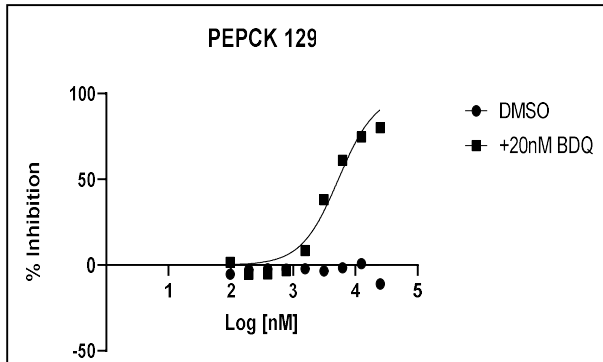
C.

PEPCK Inhibitor	Enzyme IC50	Whole Cell MIC50
PEPCK-0131	40nM	2.89 uM
PEPCK-0129	44 nM	5.35 uM
PEPCK-0001	440 nM	11.5 uM
PEPCK-0135	712nM	18.12 uM
PEPCK-0125	1500nM	>50uM

D.

Correlation between Enzyme Inhibition and Whole Cell Activity of PEPCK Inhibitors in the presence of sub-inhibitory BDQ

$y = 31.048x + 582.4$
$R^2 = 0.9662$

Whole-Cell MIC$_{50}$ (nM)

Enzyme IC$_{50}$ (nM)
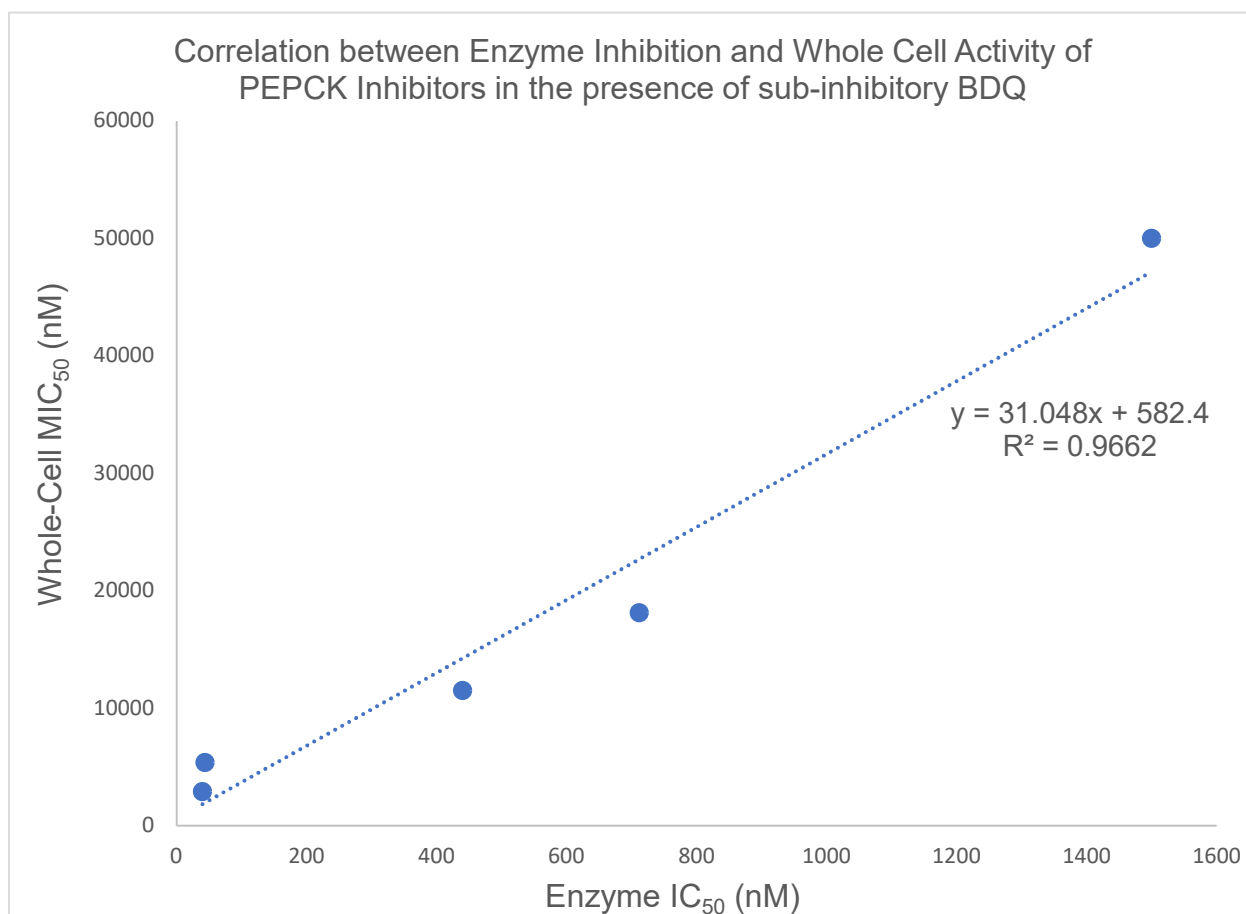
Figure 13 Whole cell potency of PEPCK inhibitor in the presence of sub-inhibitory concentration of BDQ strongly correlates with inhibitor potency against enzyme Whole cell activity was assayed (A.) using the resazurin viability reporter dye, in the presence or absence of 20nM Bedaquiline. Each PEPCK inhibitor was serially diluted (2X towards left) from a starting concentration of 50µM. The wells marked in green represent the DMSO controls, while the wells marked in red are 20µM Rifampicin control (Total growth inhibition). The growth inhibition was then plotted and fitted with Graphpad (B.) to calculate a whole cell IC$_{50}$ denoted as MIC$_{50}$. That calculated MIC$_{50}$ was then compared to the previously obtained enzyme level IC$_{50}$ (C.). The MIC$_{50}$ was then plotted against the enzyme IC$_{50}$ and fitted (D.). The plotted data was fitted with a linear trend line, which showed a strong correlation between the two (R^2=0.9662)
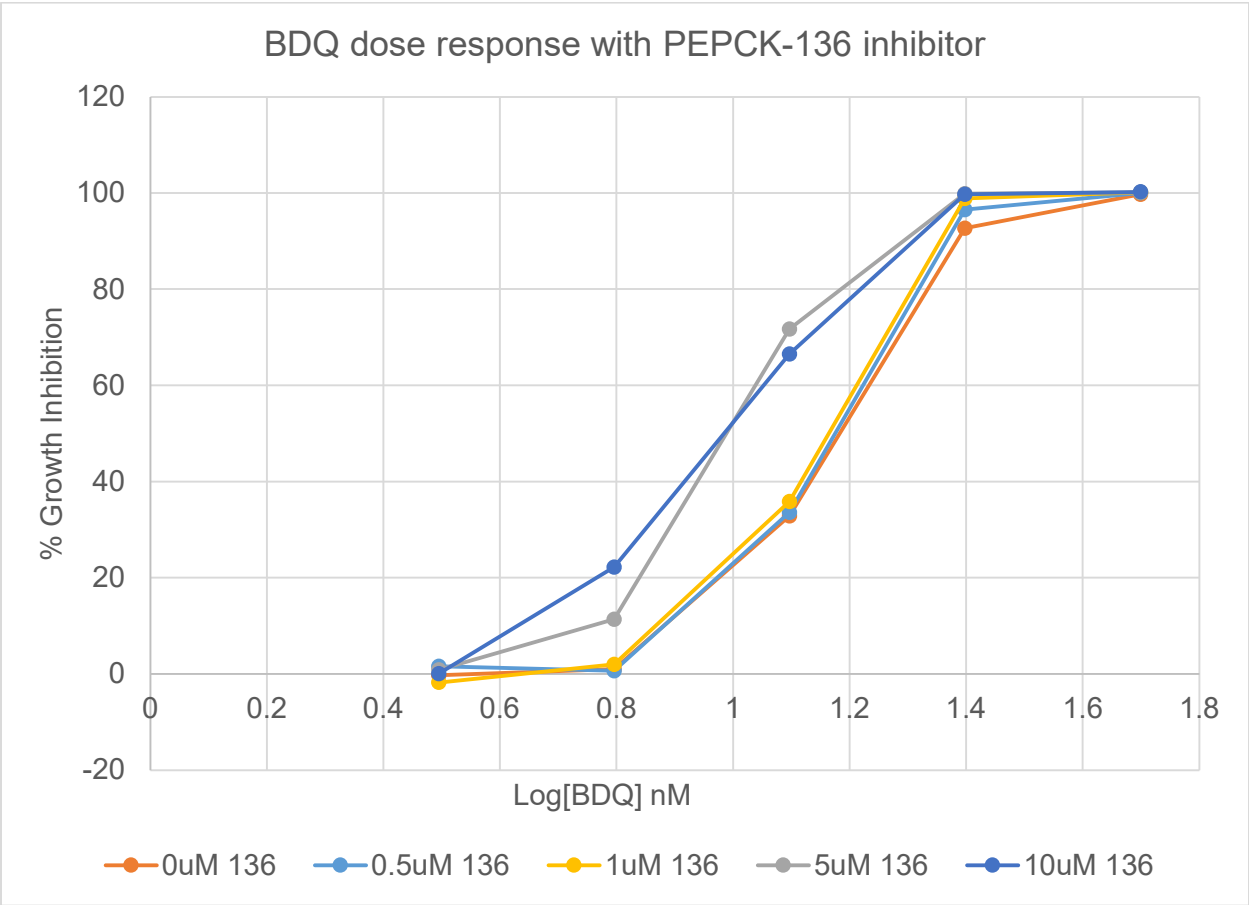
Figure 14 Bedaquiline Dose Response in the presence of PEPCK-0136

Comparison of BDQ dose response curves measured by resazurin viability reporter in the presence of 0, 0.5, 1, 5 or 10 µM of PEPCK-0136.

Time-Kill Kinetics: 150nM BDQ with and without 5uM PEPCK-0136
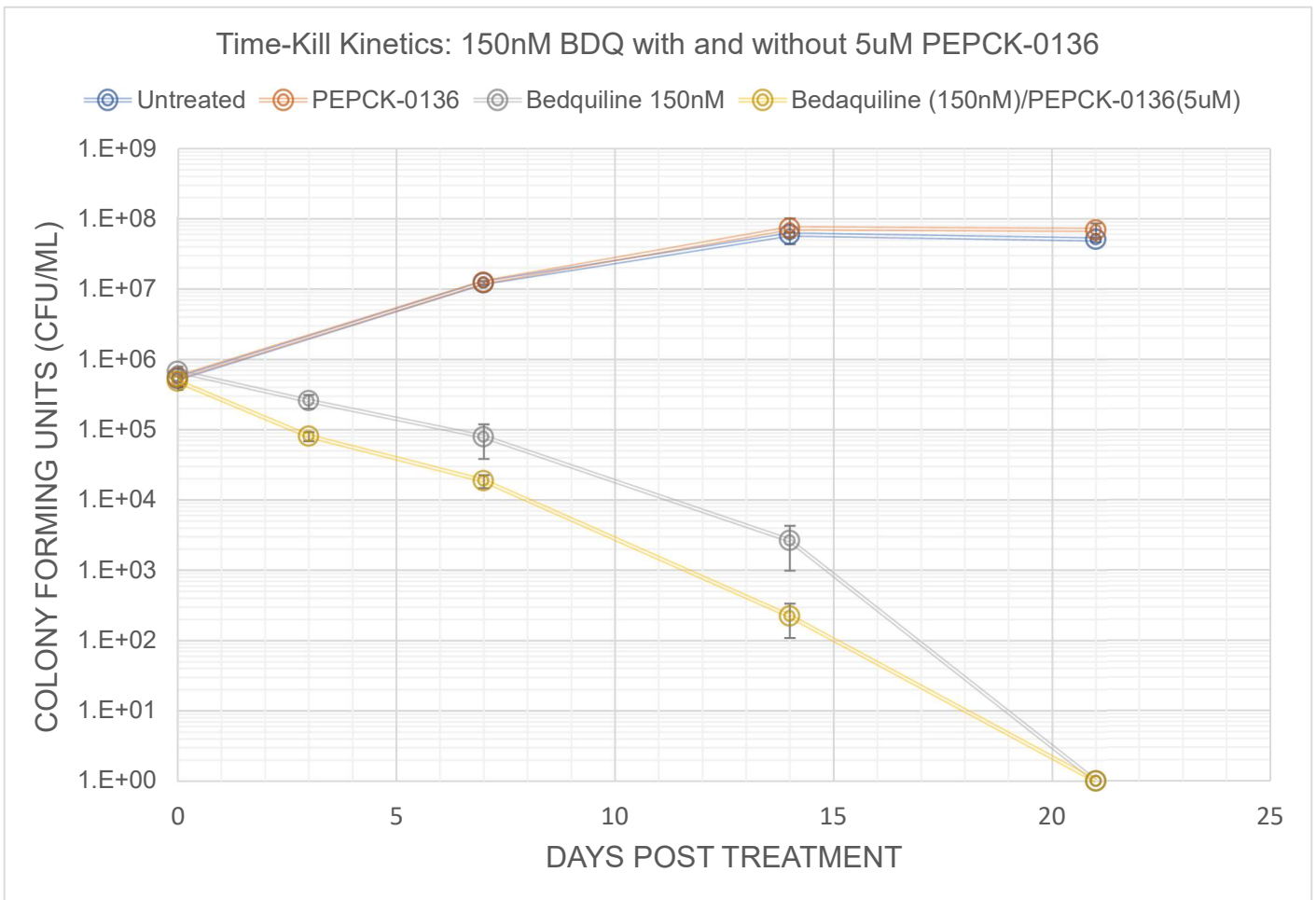
Figure 15 Time-kill kinetics shows increase bactericidal activity of inhibitory concentrations of BDQ in the presence of PEPCK-0136

Time-kill kinetic curves of DMSO control, 150nM BDQ, 5µM PEPCK-0136, 150nMBDQ/5µM PEPCK-0136. CFU counted (± SD) from out plating triplicate cultures after (0,3,7,14 and 21 days). BDQ alone and drug combination were below detection threshold at day 21.
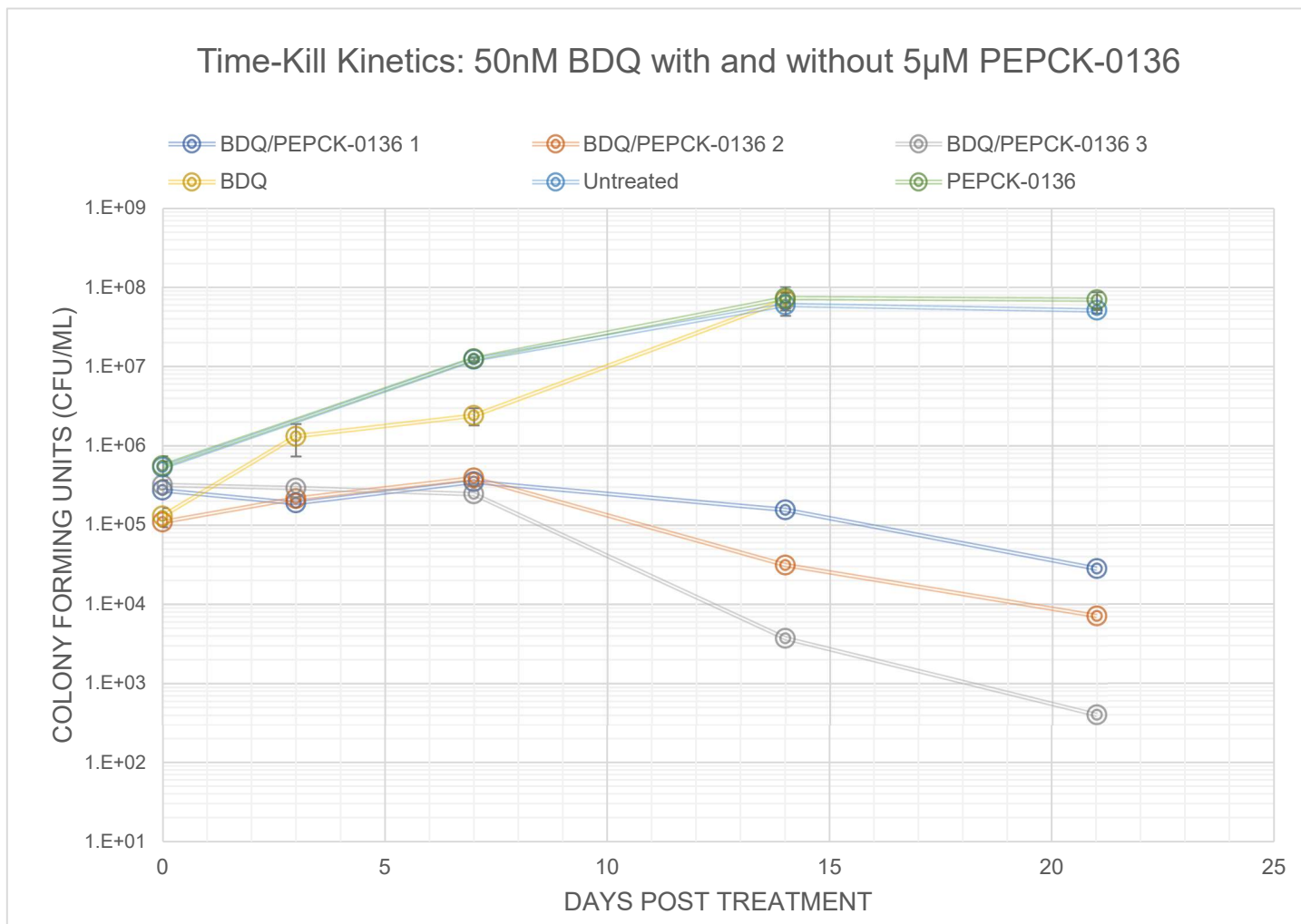
Figure 16 Time-kill kinetics show synthetic lethality of PEPCK-0136 in the presence of sub-inhibitory concentration of BDQ

Time-kill kinetics of DMSO, 5 µM PEPCK-0136, 50nM BDQ and 5µM PEPCK-0136/50nM BDQ. CFUs counted by out plating cultures at days 0,3,7,14 and 21. DMSO, BDQ and PEPCK curves are represented as mean CFUs ± SD, while the drug combination curves are show as individual replicates to show the divergence of the three replicates after day 7.

Understanding the relationship between PEPCK and Bedaquiline

Our previous results strongly suggest that our PEPCK inhibitors are synthetically lethal in the presence of Bedaquiline. However, all of the previous studies were conducted with glucose as the primary carbon source. Therefore, gluconeogenesis, which is believed to be the enzyme's primary function, should not be a very essential pathway. We thus hypothesized that under BDQ exposure, PEPCK had a secondary essential function unrelated to gluconeogenesis. A review of the literature has identified two possible pathways that could

These pathways, as previously mentioned are the GAS pathway and the reductive TCA Cycle. Both of these pathways rely on the anaplerotic reaction of PEPCK, converting PEP to OAA, utilizing NADH and CO_2 in the process. Utilization of CO_2 has been demonstrated in both low oxygen as well as when exposed to BDQ(70). Although other reactions could be responsible for fixation of CO_2, such as pyruvate carboxylase and malic enzyme, PEPCK is a likely candidate, based on our previous chemical inhibition data.

We hypothesized that if inhibition of the reductive TCA cycle was the mechanism responsible for the synthetic lethality of PEPCK inhibitors in the presence of BDQ, inhibitors of other enzymes in the pathway should have a similar effect. One of such enzymes is Fumarate hydratase, which had been previously identified as a potential drug target for hypoxic environment(64). Furthermore, a subsequent publication identified an inhibitor of fumarate hydratase(71), which was readily commercially available.

We thus decided to compare the whole cell activity of that inhibitor in the presence and absence of 20nM BDQ. Our results (Figure 17, page 87) strongly supported our hypothesis as the addition of 20nM reduced the MIC_{50} of the fumarate hydratase inhibitor by more than 15 folds.

We then hypothesized that if the function of the reverse TCA cycle is to maintain membrane potential, as it has been speculated in the literature(64), exposure to sub-inhibitory concentration of BDQ may increase the potency of an inhibitor capable of disrupting membrane potential. The novel drug SQ109, has been shown to act as an uncoupler, capable of collapsing membrane potential and pH gradient, although this is not believed to be its only mode of action(72, 73). We thus decided to measure the potency of SQ109 in the presence or absence of 20nM BDQ, once again using the resazurin viability assay. We observed a similar result (Figure 18, page 89) as with the inhibitor of fumarate hydratase, whereas in the presence of sub-inhibitory concentrations of BDQ (20nM) the MIC_{50} of SQ109 reduced 10-folds.

Chapter Summary

Our data shows that although our PEPCK inhibitor series does not inhibit growth of Mtb cells on their own, they display dose-dependent growth inhibition in the presence of BDQ. We have demonstrated that the potency of a PEPCK inhibitors under exposure to low dose BDQ is highly correlated with its potency at the enzyme level, suggesting at least some element of causality. We also demonstrated that the combination of sub-inhibitory concentration of BDQ and PEPCK-0136 is bactericidal to Mtb cells, even though cultures treated with each individual drug grew exponentially. We hypothesized that the synthetic lethality of PEPCK inhibitors in the presence of sub-inhibitory concentration may be due to the enzyme's role in the reductive TCA cycle. Indeed, we know from literature that under BDQ exposure, succinate is secreted and carbon from CO_2 is added into biomass(70), both are consistent with increased flux through the reductive TCA cycle. Additionally, we demonstrated that this increase in potency can be seen with other targets relating to this metabolic pathway, namely fumarate hydratase. We also demonstrated that BDQ exposure significantly increases the potency of SQ109, a drug capable of collapsing membrane potential, while maintaining the membrane potential is the proposed function of the reductive TCA cycle.

Although this data is consistent with the hypothesis presented, further studies need to be performed to conclusively elucidate the mechanism by which PEPCK inhibitors are synthetically lethal under sub-inhibitory concentration of BDQ. However, we believe our work makes a strong case for the development of drug regimen, specifically designed around their synergistic interactions

A.

B.

Whole cell dose response of Fumarate Hydratase Inhibitor (FHI) with or without 20nM BDQ

C.
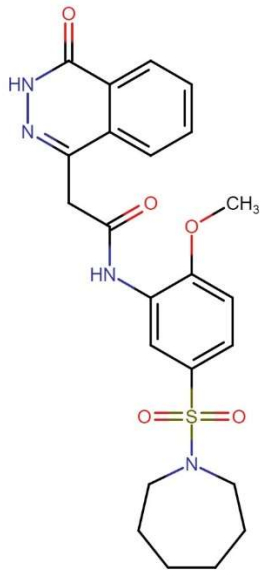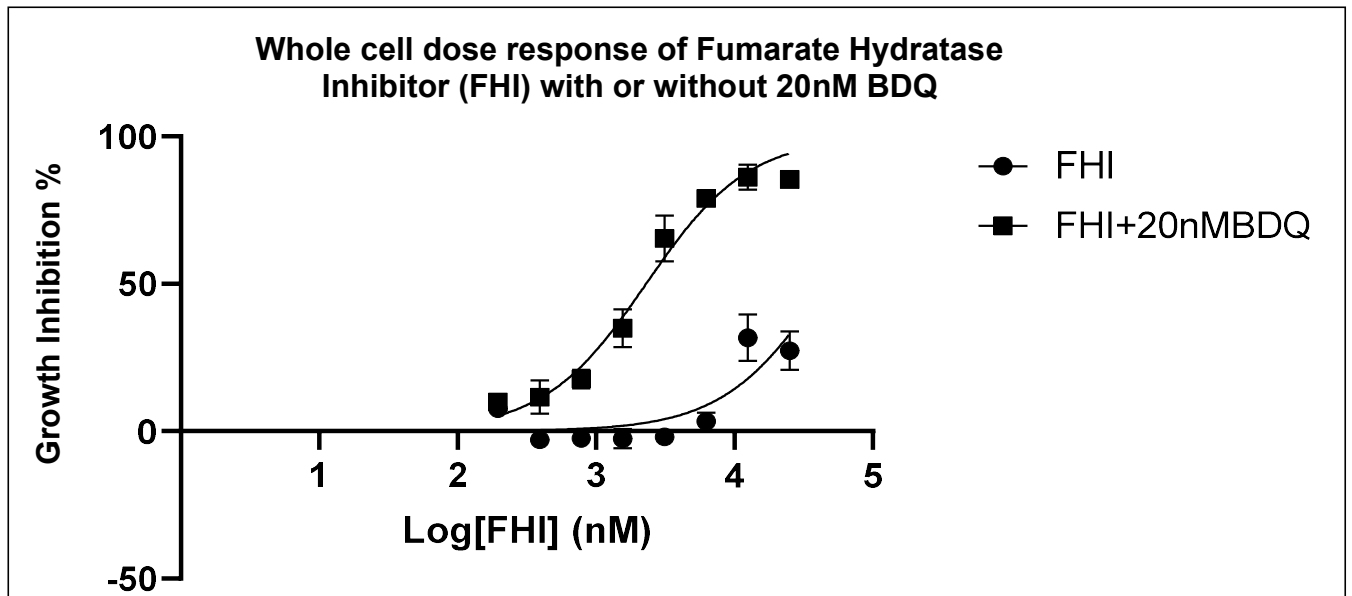
Compound	MIC$_{50}$ (95%CI)
Fumarate Hydratase Inhibitor (FHI)	31-100uM
FHI + 20nM BDQ	1.99-2.65uM

Figure 17 Inhibitor of Fumarate Hydratase has increased potency in the presence of 20nM BDQ

Whole cell growth inhibition data of a previously published(71) and commercially available Fumarate Hydratase Inhibitor (A.) by resazurin viability reporter. Percent Growth Inhibition dose response curves of triplicates, with or without the addition of 20nM BDQ (B). Comparison of MIC$_{50}$ values with and without BDQ shows large increase in potency

A.

B.

Whole cell dose response of SQ109 with or without 20nM BDQ

C.
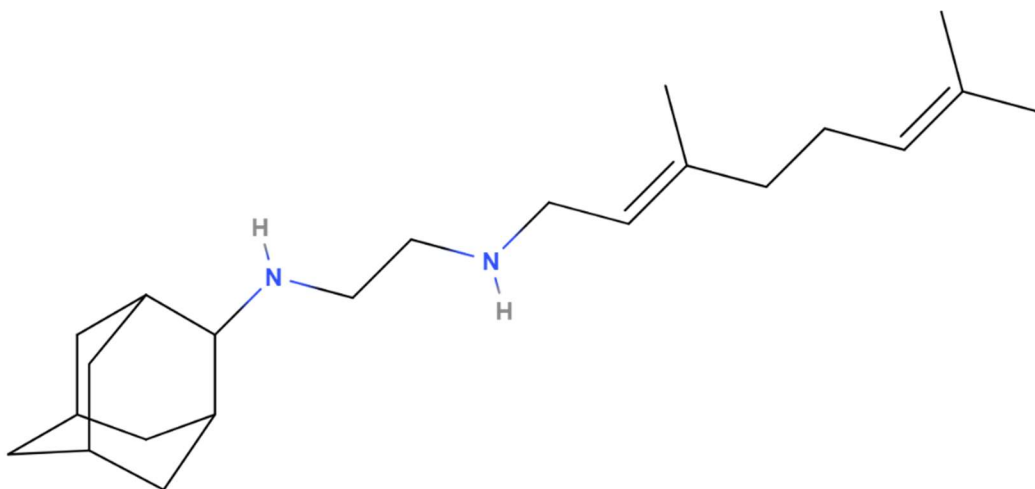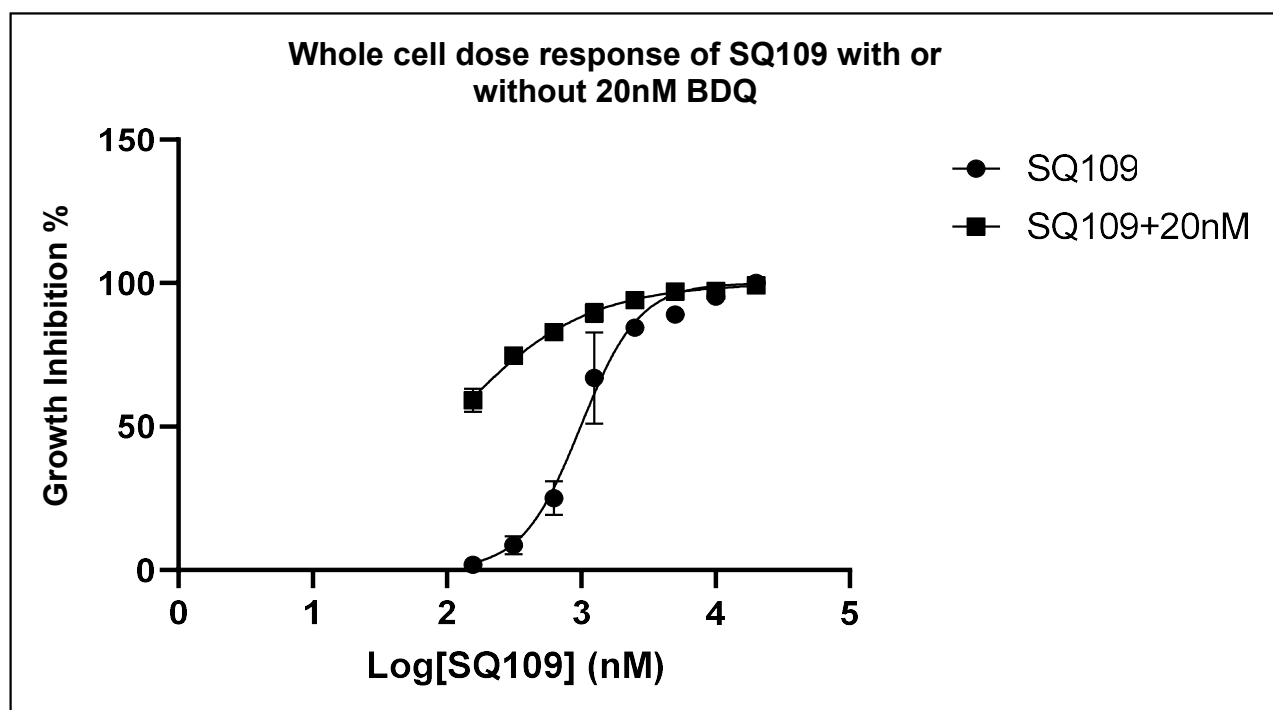
Compound	MIC$_{50}$ (95%CI)
SQ109	884-1109 nM
SQ109 + 20nM BDQ	84-109.8nM

Figure 18

SQ109 has increased potency in the presence of 20 nM BDQ

Whole cell growth inhibition data of SQ109(A.) by resazurin viability reporter dye . Dose

response cruves, with or without the addition of 20nM BDQ (B) and comparison of MIC$_{50}$

values with and without BDQ shows large increase in potency

Materials and Methods

1. Protein Expression and Purification

PckA was cloned into a pET28b vector and transformed into E. coli BL21(DE3) and selected on Carbenicillin. PEPCK was expressed by inoculating two 1L flasks containing LB and Carb. Cells were grown at 37C in an orbital shaker until the O.D. reached ~0.8. Once the cells reached the correct O.D. flasks were moved to an 18C orbital shaker for one hour before being induced with 500μM IPTG and allowed to go overnight before harvesting. Cells were harvested by centrifugation then resuspended in lysis buffer containing 50mM Tris (pH 7.5), 5% glycerol, 250mM NaCl and 5mM Imidazole. The cell suspension was lysed in a microfluidizer for at least 3 passages. Lysate was then suspended at 17000 RPM for 45 minutes at 4C. The supernatant was filtered through a 0.45μm syringe filter before being applied onto a cOmplete Ni-NTA Resin (Roche) and incubated for 10-20 minutes. The column was washed with 300mL of lysis buffer before eluting the protein with 25mL of lysis buffer containing 250mM Imidazole. The eluate was further purified on an S-200 size exclusion chromatography equilibrated with a buffer containing 25mM Tris (pH 7.5), 5% Glycerol and 150mM NaCl. Size Exclusion Chromatography can be omitted for applications that do not require high purity.

2. Enzymatic assay

The PEPCK enzyme assay was coupled with Pyruvate Kinase (PK) and Lactate Dehydrogenase (LDH). Absorbance at 340nm was measured by a Multiskan Go plate reader (Thermo Scientific), which corresponds to the peak absorbance of NADH. The assay was performed in a half-area 96 well flat bottom plate (Greiner). The enzyme assay reaction buffer was 20mM Tris-HCl (pH 7.5) containing 0.3mM GTP, 2mM $MgCl_2$, 0.1 mM $MnCl_2$, 1mM DTT, 1 mM ADP, 2 units PK/LDH, 0.25mM NADH and 2µg/mL of Mtb PEPCK. Inhibitors were first added to the reaction mixture and incubated for 20 minutes before adding 0.2mM of OAA to start the reaction. Inhibition was calculated by subtracting the quotient of the slope of absorbance decrease divided by the slope of the DMSO control.

3 Resazurin Whole Cell Assay

For whole cell assays, we used a strain of $mc^2 7000$ Mtb cell containing luciferase reporter maintained with Kanamycin resistance. For the starter culture. cells were grown in 7H9 media containing OADC, Tyloxapol, Pantothenic Acid, Malachite Green and Kanamycin until the culture reached an O.D. of 0.8-1.0. The assay media was 7H9 with 0.5% Dextrose, 0.085%NaCl, 0.05% Tyloxapol, 25µg/mL Pantothenic acid, 0.50µg/mL Kanamycin. Cells were added to the assay media to a final OD of 0.01.The cells were then added into a flat bottom 96 well plate (Costar) along with the desired Inhibitor or DMSO (4% DMSO) for a final volume of 200µL. The plates were sealed and placed at

37ºC for 7 days. After 7 days, Resazurin was added to a final concentration of 5µg/mL (5µL of 0.2mg/mL). After 24 hours, absorbance at 570 was measured and the percent growth inhibition was calculated by subtracting the quotient of Experimental/Negative Control (Rif) divided by Positive Control (DMSO)/Negative Control (Rif). The growth inhibition was then plotted into GraphPad Prism and fitted with a sigmoidal growth inhibition curve for MIC_{50} calculations. All drug combinations followed a similar protocol, only changing the inhibitor control based on the specific experiment. These include Checkerboard Assay, PEPCK inhibitor dose response in the presence of BDQ, BDQ dose response in the presence of PEPCK-0136, Fumarate Hydratase and SQ109 dose response in the presence of BDQ

4. Time-Kill Kinetics

18 7H9 cultures (15mL) were prepared with 0.5% Dextrose, 0.085% NaCl, 0.05% Tyloxapol, 25µg/mL Pantothenic acid and 0.50µg/mL Kanamycin. The cultures were separated in the following groups, each containing three replicates: DMSO, 5µM PEPCK-0136, 50nM BDQ, 150nM BDQ, 5µM PEPCK-0136/50nM BDQ and 5µM PEPCK-0136/150nM BDQ. The percent DMSO was kept constant in all cultures (4%). Each culture was inoculated with the same volume of the same starter culture (Prepared as previously described). At predetermined time points (Day 0, Day 3, Day 7, Day 14 and Day 21) a small volume (100µL) was taken out of the culture, diluted (More or less depending on result expectations) and plated on 7H10 agar containing OADC, glycerol, kanamycin and pantothenic acid. The plates were incubated at 37C until

93

colonies became visible (~4 weeks). The plate with the most countable number of CFU

(Ideally 50-400) was selected and CFU were counted using the OpenCFU software(74).

The number of CFU per plate was used to back calculate the cell concentration per mL.

The average number of bacilli per mL for each experimental condition was then plotted

as a function of time, with the error bars representing the standard deviation.

CHAPTER IV

DEVELOPMENT OF A FLUORESCENCE POLARIZATION ASSAY FOR PEPTIDYL

tRNA HYDROLASE

Introduction

Translation is one of the major pillars of the central dogma of biology. It is the process

by which mRNA is turned into proteins by the ribosome. The Ribosome is a large

complex made from both protein and ribosomal RNA (rRNA). Its function is to interact

with the messenger RNA (mRNA), recruit the correct transfer RNA (tRNA) to the

ribosome and catalyze the formation of the peptide bond that connects amino acid and

ultimately produces all proteins. The ribosome has three sites, the A-site (Aminoacyl

Site), the P-site (Peptidyl site) and the E-site (Exit site) The mRNA is recognized by the

small subunit of the ribosome via a ribosome binding site, such as the Shine-Delgarno

sequence. This ribosome binding site is typically located a few base pairs upstream of

the start codon sequence, which codes for the first amino acid. The start codon is most

commonly ATG (or AUG on the mRNA). However, in Mtb, GTG (GUG) is also very

common (33%), and TTG (UUG) is also sometimes used (4.5%) as a start codon(75).

The small subunit of the ribosome, initiation factors (IF1, IF2 and IF3), mRNA and

initiator fMet-tRNA, already positioned in the P-site) then forms the pre-initiation

complex, which will later be docked by the 50S subunit of the ribosome and form the

70S initiation complex. After the formation of the initiation complex, the tRNA with the

anticodon corresponding to the second amino acid will be recruited to the A-site, since the start codon is already positioned in the P-site. The ribosome then catalyzes the formation of a peptide bond between the amino acid on the tRNA in the A-site and the polypeptide chain in the P-site. Upon formation of the peptide bond, the mRNA will translocate by three base pairs. The tRNA that was in the P-site will translocate into the E-site and be ejected from the ribosome, while the tRNA that was in the A site, which now contains the nascent polypeptide chain will translocate to the P-site. A new tRNA, corresponding to the new codon, will then be recruited to the A-site. This cycle will repeat itself until a stop codon is reached. The stop codon will be recognized by release factors (RF1 and RF2) which will cause dissociation of the translation complex and release of the peptide chain(76).

The ribosome can stall(77) for reasons that can be grouped into two separate groups. These are known as non-stop mRNA and no-go translation events(78). Non-stop mRNA is self-explanatory and consists of mRNA that does not contain a stop codon allowing the release of the polypeptide chain. Non-go mRNA typically arises from erroneous transcription resulting in an mRNA lacking a proper stop codon. In order to rescue non-stop mRNA stalled ribosomes, the cell is able to use trans-translation mediated by transfer-mRNA (tmRNA) and the protein SmpB(79). This process recognizes the empty A site of the ribosome and utilizes the tmRNA SmpB complex along with Elongation factor EF-Tu to restore translation, ejects the mRNA lacking a stop codon and labels the nascent peptide for degradation. Upon recognition of the stalled ribosome and empty A site, the tmRNA complex will enter the A site and the polypeptide chain will be

transferred onto the tmRNA, as it translocates into the P site. Translation is thus able to continue with tmRNA as a new template. The tmRNA encodes for a protein degradation tag which alerts the cell that this polypeptide chain needs to be degraded. The tmRNA also contains a stop codon, therefore allowing translation to be properly completed. Trans-translation thus resolves the stalled ribosome and labels problematic biomolecules for degradation(80).

The no-go translation events occur when the ribosome stalls before reaching the stop codon. There are multiple events or conditions that can lead to no-go translation. For example, the presence of a rare codon in the mRNA, can cause the ribosome to stall due to a lack of properly charged tRNAs for this rare codon. Additionally, poor growing conditions can lead to amino acid starvation, which in turns reduces the number of available charged tRNA, thus causing the ribosome to stall during translation. There are also motifs within the nascent peptide chain that can cause the ribosome to stall(81), which can play a role in translational regulation of some proteins.

More importantly for this work, no-go translation events can also be caused by the use of some antibacterial compounds. Macrolides, such as erythromycin, are a well-known example of antibiotics causing the ribosome to stall. The mechanism by which it accomplishes that task is quite straightforward, since the macrolide binds directly into the nascent peptide exit tunnel.

There are a few mechanisms by which the cell can resolve no-go translation events. One of such mechanisms consists of cleaving the mRNA in the A site, which in turn creates an empty A site in the ribosome, essentially converting the no-go event into a non-stop mRNA. As previously described, non-stop translation events can then be

97

resolved by trans-translation. Additionally, sometime stalled ribosomes can also be remobilized by EF-4, thus restoring normal protein synthesis machinery.(82) Another common mechanism to resolve no-go translation events is simply by premature peptidyl tRNA drop-ff, which is the predominant outcome in cases of macrolide induced ribosome stalling. This allows the ribosome to return to its normal translation function, but also results in a free peptidyl tRNA, which must be dealt with. Because of the finite quantity of tRNA in the cell, it's crucial for the cell to be able to recycle those peptidyl tRNA. The first step to achieve tRNA recycling is to remove the incomplete peptide that is still bound to the tRNA molecule itself. This is carried out by peptidyl-tRNA hydrolase (PTH)(78).

Recent findings showed a very interesting relationship between the PTH enzyme and macrolides. Indeed, results presented in a Master's thesis from a group of collaborators(83) showed that upon depletion of PTH, Mtb became re-sensitized to macrolides. This finding is very significant as Mtb is naturally resistant to macrolides. This resistance is achieved by the methylation of the 23S rRNA in the area where macrolides bind inside the nascent peptide by the erm methyltransferase. The mechanism by which PTH depletion leads Mtb cells to be re-sensitized to macrolides is still being investigated, however this finding makes PTH a very interesting drug target.

Not only has PTH been shown to be essential for Mtb growth(84-87), but these new findings also indicate that an inhibitor of PTH could also allow us to use macrolides in the treatment of tuberculosis. Macrolides are a large category of antibiotics, being able

to use these inhibitors in combination with PTH inhibitors could unlock a multitude of

potential new drug combinations that could be effective at treating the disease.

Design of a fluorescence polarization assay for PTH and synthesis of fluorescently labelled lysyl-tRNAs

For the reasons previously discussed, Peptidyl-tRNA hydrolase became a very interesting drug discovery target. Its inhibition could lead to cellular death on its own, due to the enzyme being essential for growth, but it also unlocked the use of macrolides in a combination therapy.

Just like with any other enzyme target, we first needed to develop a robust enzyme assay that would allow us to screen for potential inhibitor molecules, which we would later be able to improve through lead-optimization. The development of a PTH assay is quite challenging because its reaction does not utilize or produce any by-product that could be directly measured or easily coupled with another enzyme that produces such by-product. Bonin and Erickson(88) developed an assay that could, according to their results, measure the activity of PTH by fluorescence polarization. Briefly, fluorescence polarization is a biophysical assay that can measure the tumbling rate of a fluorophore and since the tumbling rate of any molecule is related to the size of the molecule, this technique allows us to measure the change in size of a fluorescently labelled molecule. The design for the PTH assay was straightforward. We would label aminoacylated tRNA with a BODIPY fluorophore with an excitation and emission spectrum similar to fluorescein and containing an N-Hydroxysuccinimide ester (NHS FL BODIPY). The NHS ester allows us to label the primary amine of the amino acid charged onto the tRNA. Although the substrate of PTH is peptidyl-tRNA and not aminoacyl-tRNA, Bonin and

Erickson(88) previously demonstrated that the addition of BODIPY to the α-amine of the lysine aminoacyl-tRNA allowed PTH to use it as a substrate. We would then measure the change in polarization as PTH cleaves off the BODIPY labelled amino acid.

Unfortunately, the substrate used by the authors in the paper, lysyl-tRNA, was no longer available for us to purchase. Commercially available tRNA was only available as a pooled fraction of uncharged amino acids. Pooled fraction of tRNA synthetases was also available for purchase. Unfortunately, both pooled tRNA and tRNA synthetase had very little information on the actual composition of the pool, and how much of each tRNA was present in the reagent. This is highly problematic because each BODIPY labelled amino acid would have a different fluorescence polarization signal. While it is true that size is a major factor for polarization, the shape and rigidity of the molecule also plays a part. This effect is most commonly referred to as "propeller effect" and can have a significant effect on the polarization(89). Furthermore, some amino acids (Lysine) contain multiple primary amines, which would both be labelled by NHS FL BODIPY, creating increased variability in the assay

For all these reasons we decided that it would be best to use a single BODIPY labelled aminoacyl-tRNA. This meant that we would have to synthesize the substrate ourselves. The basic principle for synthesis of aminoacylated tRNA isn't complicated. tRNAs are RNA molecules with a stable secondary structure. Just like any other RNA molecule, we can synthesize them by T7 *in vitro* transcription and fold them by heating and cooling. The properly folded tRNA can then be aminoacylated in vitro by tRNA synthetase, which

can be recombinantly expressed in a laboratory environment. Once aminoacylated tRNA are made, following manufacturer's instructions for the labelling of primary amines with NHS FL BODIPY should be relatively simple. We decided to use lysyl tRNA for our assay since Bonin and Erickson(88) had good results using that specific aminoacyl tRNA.

The first challenge we came across was the generation of template DNA for T7 *in vitro* transcription. According to the MEGAshortscript™ T7 transcription kit we used for the generation of RNA, we needed 1µg of template DNA in a maximum volume of 8µL, which corresponds to a concentration of 125ng/µL, which is quite high. Furthermore, many commercially available PCR cleanup kits have a cutoff threshold of 100bp, while our template DNA was ~75 nucleotides long. We tested multiple polymerases and PCR cleanup kits to optimize the yield of template DNA. The best results were obtained with 100µL PCR reactions with Phusion and cleanup using the MinElute PCR purification kit by Qiagen. This specific kit has the advantage of eluting in smaller volumes than most competitors and has a cutoff threshold of 70 nucleotides. We were also able to increase the amount of template DNA we could use in the *in vitro* transcription step by using another solution containing nucleotides than the ones provided in the kit. By using a solution containing 100mM of each nucleotide as opposed to four separate solution of 75mM nucleotides, we were able to reduce the volume of nucleotide reagents from 8µL down to 1.5µL, which allowed us to use 14.5µL of template DNA per 20µL of reaction.

Through this protocol we were typically able to obtain template DNA at around

100ng/µL, which corresponds to approximately 1.5µg of template DNA per 20µL of T7 *in vitro* transcription.

The *in vitro* transcription reactions were generally quite successful by simply following the protocol provided with the MEGAshortscript™ T7 transcription kit, which is already optimized for short transcripts like tRNAs. The product of the transcription reaction was then treated with RNAse-free DNAse to remove the template DNA from the sample and purified with an RNA cleanup kit.

The purified tRNA were folded in a thermocycler by heating them to 95ºC for 2 minutes, then cooling to 20ºC for 3 minutes and finally placed at 37ºC for another 5 minutes. The folded tRNA were then aminoacylated by tRNA synthetase or stored at -80ºC until the aminoacylation reaction was done.

The aminoacylation of tRNA is done by the tRNA synthetase. Each individual tRNA/amino acid pair has its own unique tRNA synthetase. We thus cloned the Mtb gene encoding the lysyl tRNA synthetase (LysS) containing a hexa-histidine tag for affinity chromatography on Ni-NTA resin.

Unfortunately, purification of LysS was challenging, with affinity chromatography resulting in a low purity product. Further purification through size exclusion did not show great separation between LysS and contaminant (Figure 19A, page 108), but we were

nonetheless able to obtain protein that was pure enough for enzymatic reaction by pooling fewer fractions from the size-exclusion chromatogram peak, furthest from the major contaminant peak (Figure 19B, page 108).

To test the aminoacylation reaction of LysS we designed an enzyme assay that would be able to measure the enzyme activity and demonstrate that the purified enzyme is active. Briefly the assay was couple with pyrophosphatase, which converts the pyrophosphate generated by the tRNA synthetase into free phosphate, which can then be measured by the addition of BioMol green, a reagent which turns green when phosphate is present, which can then be measured by a spectrophotometer at a wavelength of 620 nm. The major drawback to this enzyme assay is that pyrophosphate is released after the first half-reaction of the aminoacylation reaction. Although our data confirms that the purified LysS is indeed active (Figure 20, page 110), it only confirms the creation of the half-reaction intermediate but cannot by itself definitely confirm that the tRNA was charged with lysine. This was, however a good enough indication of enzymatic activity to continue the synthesis of our lysyl-tRNA substrate.

After the aminoacylation reaction was carried we performed phenol/chloroform extraction of nucleic acid. This step was crucial for removing the LysS enzyme as well as the remaining free lysine. BODIPY NHS FL (lumiprobe) labelling of the primary amines was performed according to the manufacturer's directions, except that the reagents were incubated on ice for 4 hours, as opposed to room temperature as directed by the manufacturers protocol. The reason being that at alkaline pH or 37ºC

aminoacylated tRNA are not very stable and have a half-life of less than 2 hours. Since the BODIPY labelling reaction is done at pH 8.5 the reaction time must be minimized(90). After BODIPY labelling, tRNA were precipitated with ethanol, and further purified with a RNA cleanup kit. This last step proved to be crucial to remove significant amounts of unreacted BODIPY.

To confirm that we have indeed synthesized BODIPY labelled lysyl-tRNA, we ran the product on a Urea-PAGE gel. We first imaged the gel without staining and imaged using the signal for fluorescein, which has similar excitation and emission spectra as BODIPY FL (Figure 21A, page 111). Our results show a clear band at the appropriate size that represents the proper labelling of lysyl tRNA (lanes 1-6). The well containing unreacted lysyl tRNA (lane 7), at a similar concentration, is not visible on the urea-PAGE gels, confirming that the signal observed is not due to RNA autofluorescence. To prove this point further, after imaging with the fluorescein filter, we stained the urea-PAGE gel with the nucleic acid stain gel green and imaged again using the appropriate filter (Figure 21B, page 111). With the nucleic acid stain, the unreacted lysyl-tRNA (lane 7) was now clearly visible with an intensity like that of the BODIPY labelled samples. Additionally, various amounts of PTH were added to some samples and allowed to react for 15 minutes before being run on the gel. Densitometric analysis of the gel image (Figure 22, page 113) shows that increasing the amount of PTH decreases the fluorescence intensity of BODIPY at the tRNA band. In order to test whether this decrease was due to hydrolysis of the BODIPY-lysine from the tRNA or the tRNA themselves being affected; we also performed the same image analysis of the fluorescence intensity of Gel Green. Although the results still show a slight decrease with increasing levels of PTH (Figure

105

22, page 113), it is much smaller. After a 15-minute incubation with 1μM PTH, the fluorescence intensity of BODIPY was 44% of the no PTH control, while the fluorescence intensity of gel green was 90% of the no PTH control. The decrease in fluorescence intensity of gel green could be interpreted in a few different ways. First, PTH could have caused some tRNAs to crash out of solution, effectively reducing the amount of tRNA in the gel. Second, each well could have been loaded with slightly different amounts of tRNA solution, and the linear decrease is just coincidental. Third, since both Fluorescein and gel green have similar excitation/emission spectra, the decrease in gel green fluorescence could simply be due to a decrease in BODIPY signal. We also performed a densitometric analysis of the band we believe represents free BODIPY-lysine. Our results show an increase in BODIPY fluorescence, although this increase is only significant for the highest PTH concentration. Taken together these results strongly suggest that we synthesized the BODIPY lysyl-tRNA that could be used as a substrate in a fluorescence polarization assay for PTH. We also demonstrated that the substrate can be hydrolyzed by PTH.

Chapter Summary

Taken together our results demonstrate that we were able to synthesize the substrate necessary for the development of a fluorescence polarization assay of PTH. We clearly demonstrated through analysis of urea-PAGE RNA gel, that we were able to create fluorescently labelled tRNAs, which upon addition of PTH can be hydrolyzed, resulting in a loss of fluorescence intensity from BODIPY localized at the tRNA band. Through fluorescence polarization, we believe this hydrolysis could potentially be assayed allowing for the screening of potential inhibitors. These results also confirm that all previous steps were successful. In order to make this observation on the urea-PAGE gel, *in vitro* transcription, tRNA folding, aminoacylation of tRNA by LysS and BODIPY labelling all had to be successful. Failure at any of those steps would have resulted in a lack of BODIPY signal at the mRNA band. Indeed, BODIPY labels the primary amine of lysine, therefore for the BODIPY signal to co-localize with the tRNA signal, the tRNA has to be aminoacylated. For the tRNA to be aminoacylated, LysS must be active and capable of catalyzing this reaction, as it does not occur spontaneously. In addition to LysS being active, this also tells us that tRNA had to be properly folded, as the substrate for LysS is folded tRNA. Lastly, if tRNA were properly folded, it also shows that *in vitro* transcription worked as intended and synthesized the correct RNA. This work lays the foundation for the development of a peptidyl tRNA hydrolase assay necessary for a drug discovery campaign to be initiated.

A.
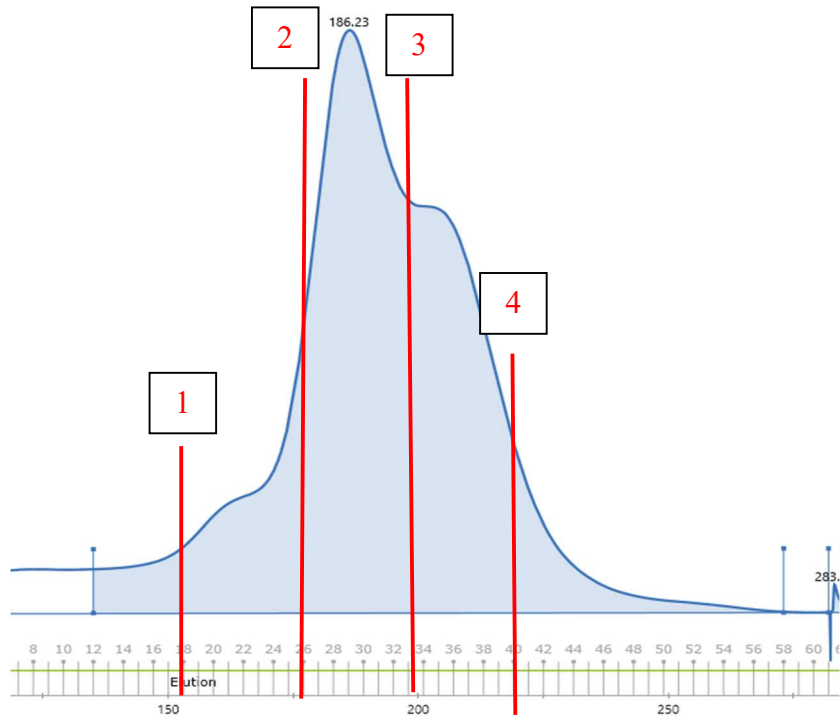
B.
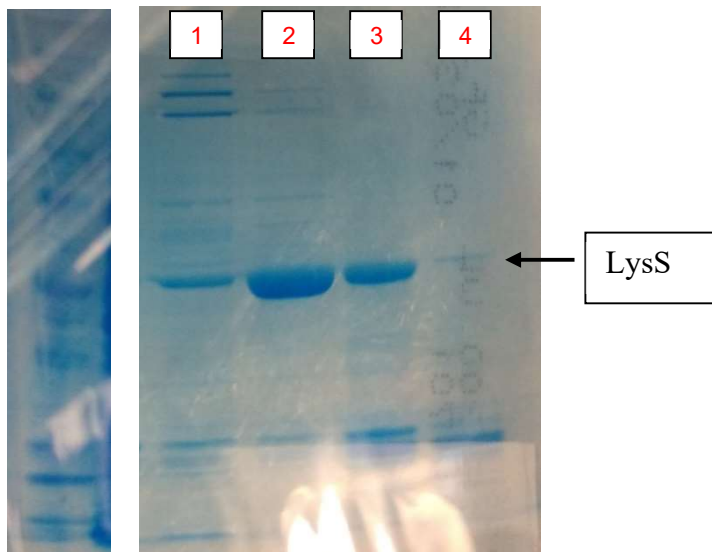
Figure 19. LysS can be purified to an acceptable level of purity by affinity chromatography and size exclusion chromatography.

Size exclusion chromatogram (A) shows two major peaks corresponding to LysS and an unknown major contaminant protein. The numbers indicate the fractions collected and evaluated by SDS-PAGE(B). Fractions from the leading edge of the LysS peak (Fraction 2) show the best LysS purity.
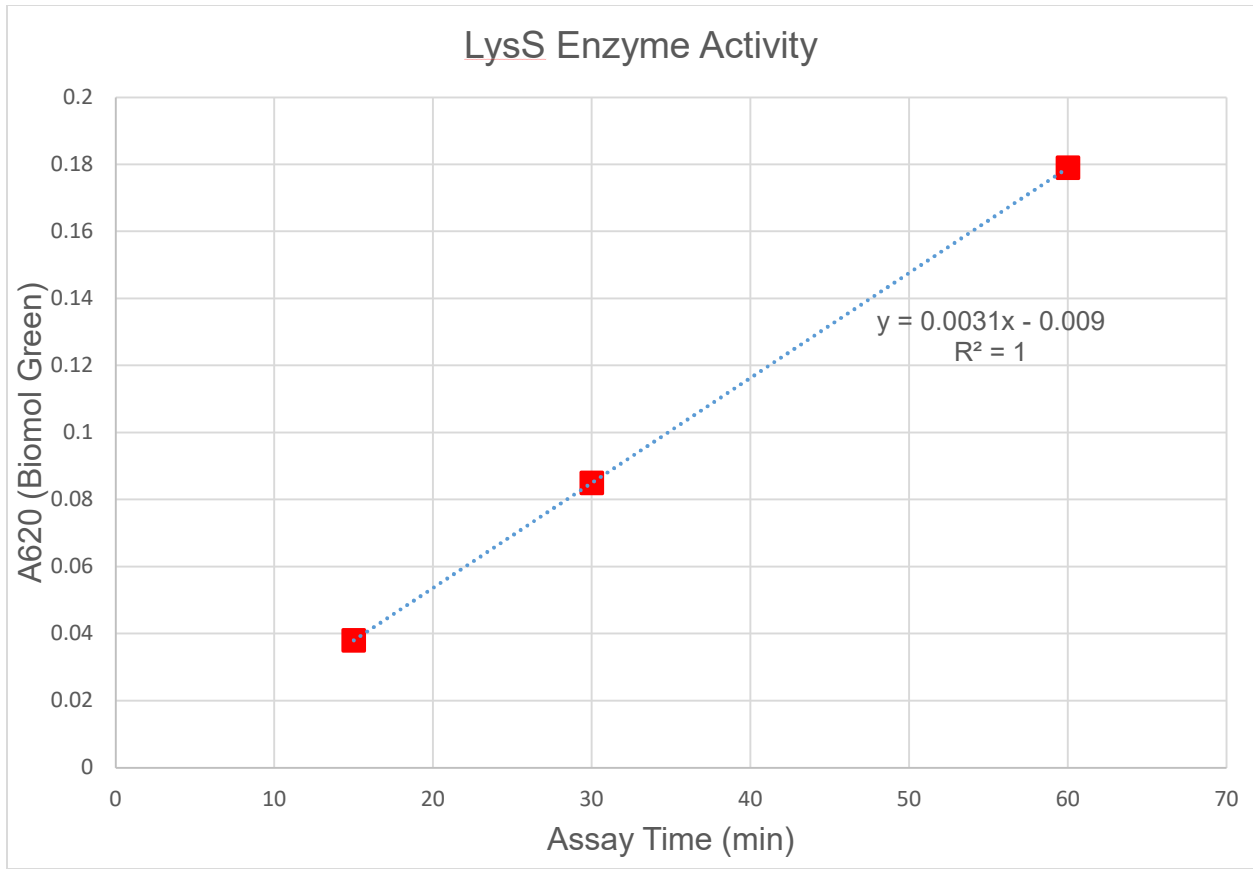
Figure 20. LysS Enzyme assay suggests recombinant LysS is active

Biomol Green based LysS/pyrophosphatase coupled enzyme assay shows increase in absorbance at 620nm over time, indicative of an increase of free phosphate, which should correlate to LysS activity of the first half reaction of its aminoacylation reaction. Each data point is the difference of the A620 of the no-enzyme control subtracted from the A620 of the experimental control.

A.

BODIPY-Lys-tRNA
(75 nucleotides)

Dye Front (40
Nucleotides)

Dye Front (20
Nucleotides)

B.

BODIPY-Lys-tRNA
(75 nucleotides)
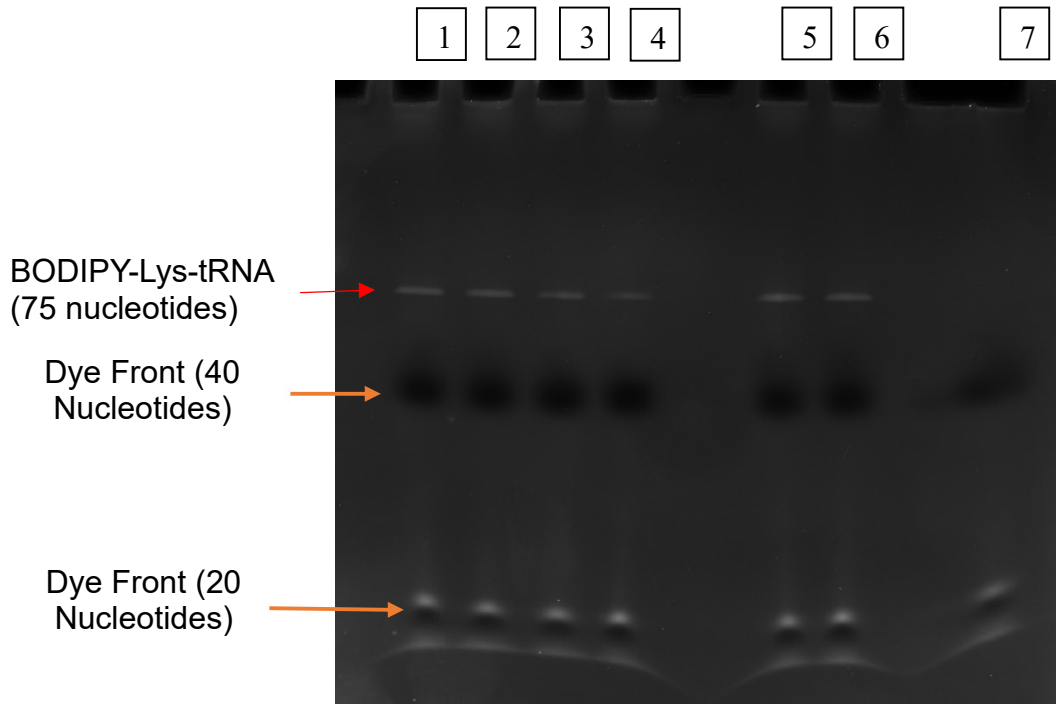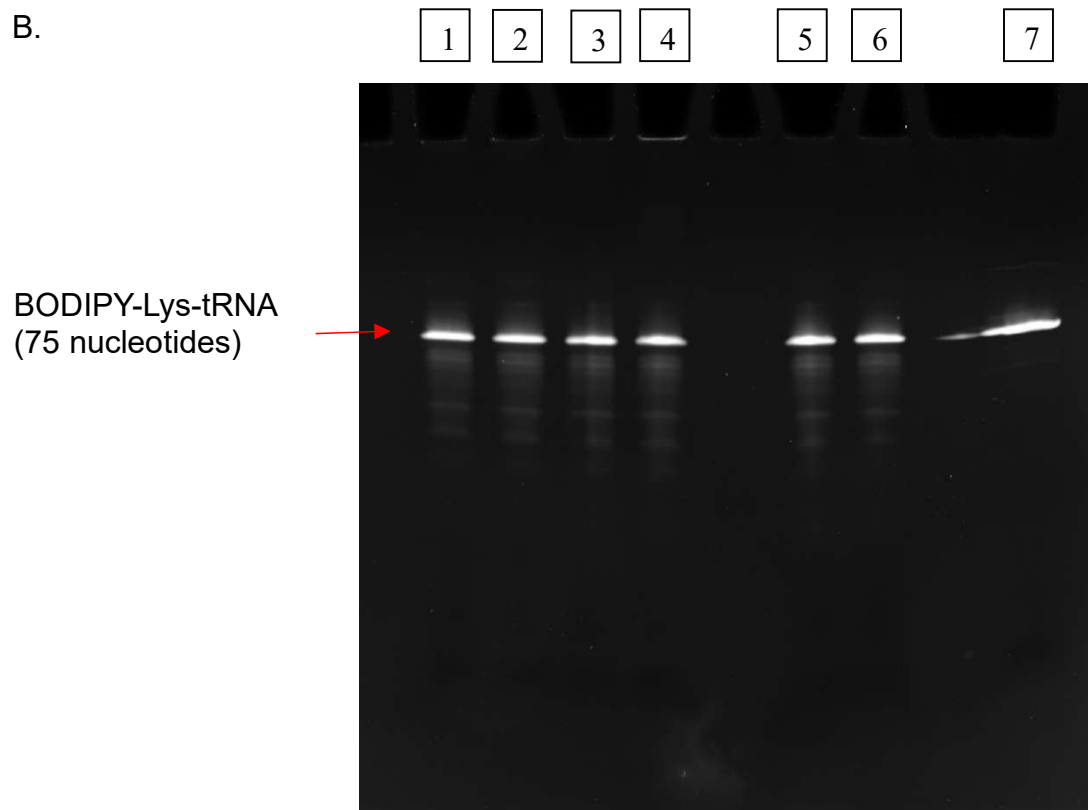
Figure 21. Imaging of urea-PAGE RNA gel demonstrate BODIPY labelling of lysyl-tRNA

Imaging of urea-PAGE RNA gel using fluorescein signal of the gel prior to staining with nucleic acid dye (A) and gel green fluorescent signal after staining with Gel Green (B). In lanes 1-4, BODIPY-lysyl-tRNA was incubated for 15 minutes at 37ºC with 1, 10, 100 and 1000 nM PTH enzyme respectively. In lanes 5 BODIPY-lysyl-tRNA was placed at 37ºC for 15 minutes without PTH. Lane 6 was BODIPY-lysyl-tRNA that was not incubated at 37ºC, and was directly loaded into the RNA gel. Lane 7 contains lysyl-tRNA prior to BODIPY labelling.

Relative BODIPY and Gel Green Fluorescence Intensity of the tRNA band after PTH treatment
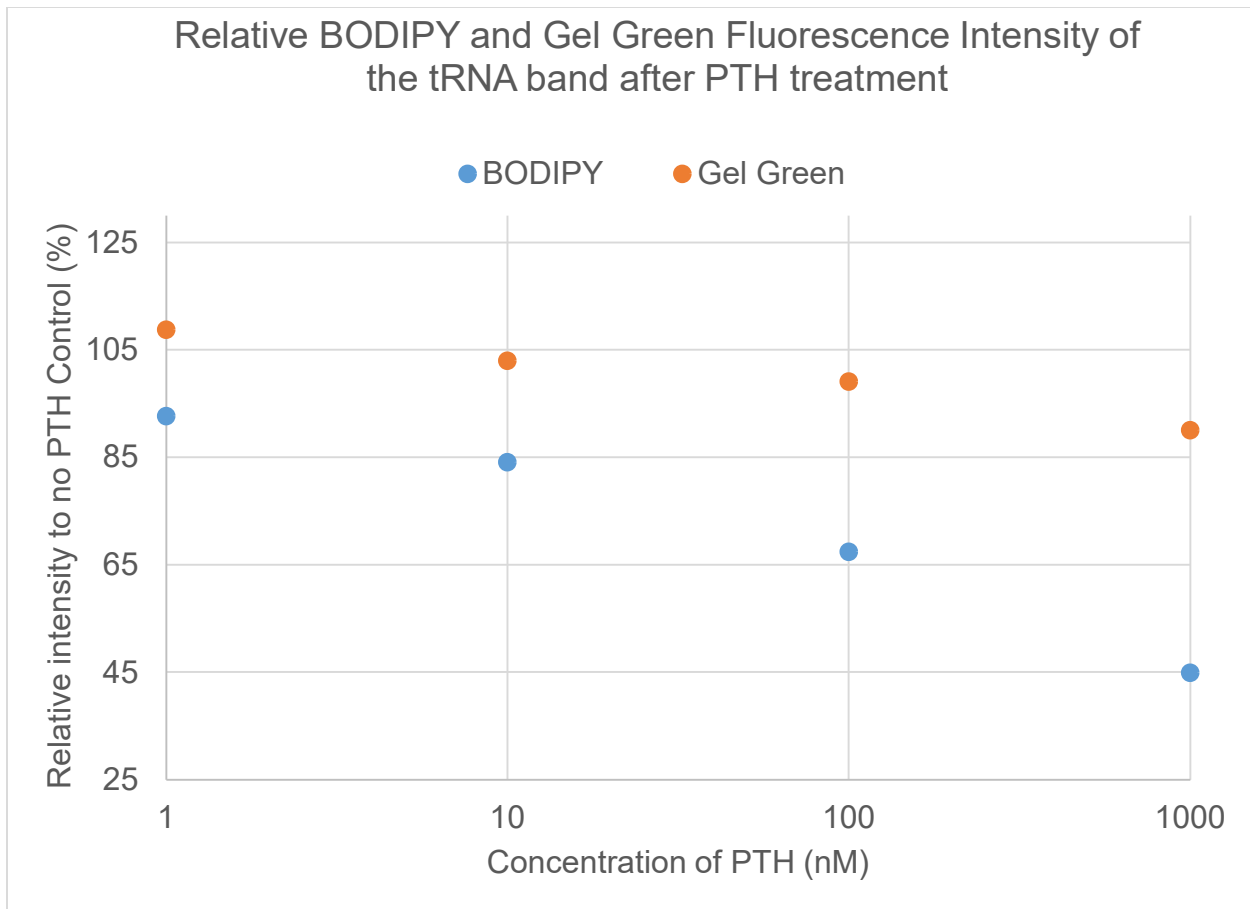
Figure 22. Densitometric analysis of urea-PAGE shows that increasing PTH concentration results in a reduction of BODIPY intensity of the tRNA band

Amount of fluorescence intensity relative to the no-PTH control for BODIPY (orange) and gel green (blue) measured at the tRNA band with ImageJ. The decrease of BODIPY signal was more significant, suggesting that PTH is hydrolyzing the Lysyl-tRNA, thus releasing the BODIPY fluorophore.

Materials and Methods

1.tRNA Preparation

tRNAs were prepared by *in vitro* transcription overnight using the MEGAShortscript™

T7 kit (Thermofischer) following the manufacturer's instructions. The provided protocol

was altered by using a NTP mixture containing each NTP at 100µM instead of 4 solution

of 75µM. Final NTP concentration was the same as the manufacturer's protocol. The

product was then treated with RNAse free DNAse (NEB) to remove template DNA and

purified with purified with Monarch RNA Cleanup Kit (NEB). Purified tRNAs were folded

in a thermocycler, by heating to 95ºC for 2 minutes, cooling to 20ºC for 3 minutes,

followed by another 5 minutes at 37ºC. The amount of RNA was then quantified with a

nano drop and stored at -80ºC.

2.Aminoacylation of tRNA by LysS

The tRNA were aminoacylated in by mixing 8µM tRNA, 3.3 mM ATP, 14µM Lysine,

1.5µM LysS and 1X of reaction buffer (10X buffer was 500mM HEPES buffer (pH7.5),

250mM KCl, 150mM $MgCl_2$, 1mM DTT). The aminoacylation reaction was incubated at

37ºC for 2 hours.

For each 150µL of aminoacylation reaction, add 250µL of 100mM NaOAc, 1mM EDTA

(pH 4.8) and mix with 400µL of Phenol/choloroform (5:1). Adjust volume if necessary.

Vortex the mixture and centrifuge at max speed for 5 minutes at 4ºC. Remove the aqueous phase and add 1/10th volume of 3M NaOAc (pH 5.0). Add 3.5 Volume of Ice-cold ethanol to precipitate the tRNA. The solution was then centrifuged at maximum speed for 10 minutes to pellet the tRNA. The supernatant was removed by pipetting and allowing residual ethanol to evaporate.

3.BODIPY-labelling of tRNA Lysyl-tRNA

0.1 mg of BODIPY FL NHS was dissolved in 10 μL DMSO. 10μL of 1M Sodium Bicarbonate (pH 8.5) and 80μL of RNAse free water was added to the dissolved fluorophore. The resulting solution was used to resuspend the tRNA pellet prepared in the previous step. The resuspended tRNA were incubated on ice for 2 hours. The tRNA were precipitated with ice cold ethanol and further purified using the Monarch RNA Cleanup Kit(NEB).

4.Urea-PAGE Electrophoresis

Various concentration of PTH were combined with 800ng of BODIPY labelled lysyl-tRNA. 2X TBE Urea-PAGE loading dye (Invitrogen) was added to each sample before being placed in a heating block following the manufacturer's direction. The samples were then loaded in a TBE Urea-PAGE gel (Invitrogen). Current was applied until the dye front had nearly reached the bottom of the gel. The gel was then imaged in a

chemidoc (Bio-Rad), using fluorescein filter settings. The gel was then stained with Gel Green (Biotium) nucleic acid stain following manufacturer's instructions, before being imaged in a Chemidoc (Bio-Rad) using the gel green filter settings.

REFERENCES

1.   World Health O. GLOBAL TUBERCULOSIS REPORT 2019. [S.I.]: WORLD

HEALTH ORGANIZATION; 2019.

2.   Zimmerman MR. Pulmonary and osseous tuberculosis in an Egyptian mummy.

Bull N Y Acad Med. 1979;55(6):604-8. Epub 1979/06/01. PubMed PMID: 380700;

PMCID: PMC1807652.

3.   Barberis I, Bragazzi NL, Galluzzo L, Martini M. The history of tuberculosis: from

the first historical records to the isolation of Koch's bacillus. J Prev Med Hyg.

2017;58(1):E9-E12. Epub 2017/05/19. PubMed PMID: 28515626; PMCID:

PMC5432783.

4.   Daniel VS, Daniel TM. Old Testament biblical references to tuberculosis. Clin

Infect Dis. 1999;29(6):1557-8. Epub 1999/12/10. doi: 10.1086/313562. PubMed PMID:

10585812.

5.   Eddy JJ. The ancient city of Rome, its empire, and the spread of tuberculosis in

Europe. Tuberculosis (Edinb). 2015;95 Suppl 1:S23-8. Epub 2015/03/17. doi:

10.1016/j.tube.2015.02.005. PubMed PMID: 25771202.

6.   Villemin JA. On the virulence and specificity of tuberculosis. Int J Tuberc Lung

Dis. 2015;19(3):256-66. Epub 2015/02/17. doi: 10.5588/ijtld.06.0636-v. PubMed PMID:

25686129.

7.   Ziehl F. Zur Färbung des tuberkelbacillus. DMW-Deutsche Medizinische

Wochenschrift. 1882;8(33):451-.

8.   Cambau E, Drancourt M. Steps towards the discovery of Mycobacterium tuberculosis by Robert Koch, 1882. Clin Microbiol Infec. 2014;20(3):196-201. doi: 10.1111/1469-0691.12555. PubMed PMID: WOS:000331024400011.

9.   Koch R. Die aetiologie der tuberkulose2010.

10.   Furin J, Cox H, Pai M. Tuberculosis. Lancet. 2019;393(10181):1642-56. Epub 2019/03/25. doi: 10.1016/S0140-6736(19)30308-3. PubMed PMID: 30904262.

11.   Nahid P, Dorman SE, Alipanah N, Barry PM, Brozek JL, Cattamanchi A, Chaisson LH, Chaisson RE, Daley CL, Grzemska M, Higashi JM, Ho CS, Hopewell PC, Keshavjee SA, Lienhardt C, Menzies R, Merrifield C, Narita M, O'Brien R, Peloquin CA, Raftery A, Saukkonen J, Schaaf HS, Sotgiu G, Starke JR, Migliori GB, Vernon A. Executive Summary: Official American Thoracic Society/Centers for Disease Control and Prevention/Infectious Diseases Society of America Clinical Practice Guidelines: Treatment of Drug-Susceptible Tuberculosis. Clin Infect Dis. 2016;63(7):853-67. Epub 2016/09/14. doi: 10.1093/cid/ciw566. PubMed PMID: 27621353; PMCID: PMC6366011.

12.   Gube AA, Debalkie M, Seid K, Bisete K, Mengesha A, Zeynu A, Shimelis F, Gebremeskel F. Assessment of Anti-TB Drug Nonadherence and Associated Factors among TB Patients Attending TB Clinics in Arba Minch Governmental Health Institutions, Southern Ethiopia. Tuberc Res Treat. 2018;2018:3705812. Epub 2018/04/20. doi: 10.1155/2018/3705812. PubMed PMID: 29670768; PMCID: PMC5835254.

13.   Iweama CN, Agbaje OS, Umoke PCI, Igbokwe CC, Ozoemena EL, Omaka-Amari NL, Idache BM. Nonadherence to tuberculosis treatment and associated factors among patients using directly observed treatment short-course in north-west Nigeria: A cross-

sectional study. SAGE Open Med. 2021;9:2050312121989497. Epub 2021/02/23. doi: 10.1177/2050312121989497. PubMed PMID: 33614034; PMCID: PMC7871291.

14.   Mekonnen HS, Azagew AW. Non-adherence to anti-tuberculosis treatment, reasons and associated factors among TB patients attending at Gondar town health centers, Northwest Ethiopia. BMC Res Notes. 2018;11(1):691. Epub 2018/10/05. doi: 10.1186/s13104-018-3789-4. PubMed PMID: 30285907; PMCID: PMC6167840.

15.   Mahajan R. Bedaquiline: First FDA-approved tuberculosis drug in 40 years. Int J Appl Basic Med Res. 2013;3(1):1-2. Epub 2013/06/19. doi: 10.4103/2229-516X.112228. PubMed PMID: 23776831; PMCID: PMC3678673.

16.   Ryan NJ, Lo JH. Delamanid: first global approval. Drugs. 2014;74(9):1041-5. Epub 2014/06/14. doi: 10.1007/s40265-014-0241-5. PubMed PMID: 24923253.

17.   Keam SJ. Pretomanid: First Approval. Drugs. 2019;79(16):1797-803. Epub 2019/10/05. doi: 10.1007/s40265-019-01207-9. PubMed PMID: 31583606.

18.   Ismail NA, Mvusi L, Nanoo A, Dreyer A, Omar SV, Babatunde S, Molebatsi T, van der Walt M, Adelekan A, Deyde V, Ihekweazu C, Madhi SA. Prevalence of drug-resistant tuberculosis and imputed burden in South Africa: a national and sub-national cross-sectional survey. Lancet Infect Dis. 2018;18(7):779-87. Epub 2018/04/25. doi: 10.1016/S1473-3099(18)30222-6. PubMed PMID: 29685458; PMCID: PMC6800151.

19.   Shah NS, Auld SC, Brust JC, Mathema B, Ismail N, Moodley P, Mlisana K, Allana S, Campbell A, Mthiyane T, Morris N, Mpangase P, van der Meulen H, Omar SV, Brown TS, Narechania A, Shaskina E, Kapwata T, Kreiswirth B, Gandhi NR. Transmission of Extensively Drug-Resistant Tuberculosis in South Africa. N Engl J Med.

2017;376(3):243-53. Epub 2017/01/19. doi: 10.1056/NEJMoa1604544. PubMed PMID: 28099825; PMCID: PMC5330208.

20.   Goyal S, Klassert TE, Slevogt H. C-type lectin receptors in tuberculosis: what we know. Med Microbiol Immunol. 2016;205(6):513-35. Epub 2016/11/04. doi: 10.1007/s00430-016-0470-1. PubMed PMID: 27469378.

21.   Schafer G, Guler R, Murray G, Brombacher F, Brown GD. The role of scavenger receptor B1 in infection with Mycobacterium tuberculosis in a murine model. PLoS One. 2009;4(12):e8448. Epub 2009/12/31. doi: 10.1371/journal.pone.0008448. PubMed PMID: 20041149; PMCID: PMC2794535.

22.   Velasco-Velazquez MA, Barrera D, Gonzalez-Arenas A, Rosales C, Agramonte-Hevia J. Macrophage--Mycobacterium tuberculosis interactions: role of complement receptor 3. Microb Pathog. 2003;35(3):125-31. Epub 2003/08/21. doi: 10.1016/s0882-4010(03)00099-8. PubMed PMID: 12927520.

23.   Vergne I, Fratti RA, Hill PJ, Chua J, Belisle J, Deretic V. Mycobacterium tuberculosis phagosome maturation arrest: mycobacterial phosphatidylinositol analog phosphatidylinositol mannoside stimulates early endosomal fusion. Mol Biol Cell. 2004;15(2):751-60. Epub 2003/11/18. doi: 10.1091/mbc.e03-05-0307. PubMed PMID: 14617817; PMCID: PMC329390.

24.   Rink J, Ghigo E, Kalaidzidis Y, Zerial M. Rab conversion as a mechanism of progression from early to late endosomes. Cell. 2005;122(5):735-49. Epub 2005/09/07. doi: 10.1016/j.cell.2005.06.043. PubMed PMID: 16143105.

25.   Spano S, Galan JE. Taking control: Hijacking of Rab GTPases by intracellular bacterial pathogens. Small GTPases. 2018;9(1-2):182-91. Epub 2017/06/21. doi: 10.1080/21541248.2017.1336192. PubMed PMID: 28632996; PMCID: PMC5902217.

26.   Rustad TR, Sherrid AM, Minch KJ, Sherman DR. Hypoxia: a window into Mycobacterium tuberculosis latency. Cell Microbiol. 2009;11(8):1151-9. Epub 2009/04/25. doi: 10.1111/j.1462-5822.2009.01325.x. PubMed PMID: 19388905.

27.   Leylabadlo HE, Kafil HS, Yousefi M, Aghazadeh M, Asgharzadeh M. Pulmonary Tuberculosis Diagnosis: Where We Are? Tuberc Respir Dis (Seoul). 2016;79(3):134-42. Epub 2016/07/20. doi: 10.4046/trd.2016.79.3.134. PubMed PMID: 27433173; PMCID: PMC4943897.

28.   CDC. Tuberculin Skin Testing [Fact Sheet]. In: Control CfD, editor. https://www.cdc.gov/tb/publications/factsheets/testing/skintesting.pdf2020.

29.   Zwerling A, Behr MA, Verma A, Brewer TF, Menzies D, Pai M. The BCG World Atlas: a database of global BCG vaccination policies and practices. PLoS Med. 2011;8(3):e1001012. Epub 2011/03/30. doi: 10.1371/journal.pmed.1001012. PubMed PMID: 21445325; PMCID: PMC3062527.

30.   CDC. TB Elimination Interferon-Gamma Release Assays (IGRAs) - Blood Tests for TB Infection [Fact Sheet]. In: Control CfD, editor. https://www.cdc.gov/tb/publications/factsheets/testing/IGRA.pdf2011.

31.   WHO. Chest Radiography in Tuberculosis Detection. In: Organization. WH, editor. https://www.who.int/tb/publications/Radiography_TB_factsheet.pdf2016.

32.   Zeka AN, Tasbakan S, Cavusoglu C. Evaluation of the GeneXpert MTB/RIF assay for rapid diagnosis of tuberculosis and detection of rifampin resistance in

pulmonary and extrapulmonary specimens. J Clin Microbiol. 2011;49(12):4138-41. Epub 2011/10/01. doi: 10.1128/JCM.05434-11. PubMed PMID: 21956978; PMCID: PMC3232962.

33.   Tomaz APO, Raboni SM, Kussen GMB, da Silva Nogueira K, Lopes Ribeiro CE, Costa LMD. The Xpert(R) MTB/RIF diagnostic test for pulmonary and extrapulmonary tuberculosis in immunocompetent and immunocompromised patients: Benefits and experiences over 2 years in different clinical contexts. PLoS One. 2021;16(3):e0247185. Epub 2021/03/04. doi: 10.1371/journal.pone.0247185. PubMed PMID: 33657113; PMCID: PMC7928506.

34.   Pooran A, Theron G, Zijenah L, Chanda D, Clowes P, Mwenge L, Mutenherwa F, Lecesse P, Metcalfe J, Sohn H, Hoelscher M, Pym A, Peter J, Dowdy D, Dheda K. Point of care Xpert MTB/RIF versus smear microscopy for tuberculosis diagnosis in southern African primary care clinics: a multicentre economic evaluation. Lancet Glob Health. 2019;7(6):E798-E807. doi: Doi 10.1016/S2214-109x(19)30164-0. PubMed PMID: WOS:000467822500024.

35.   Parsons LM, Somoskovi A, Gutierrez C, Lee E, Paramasivan CN, Abimiku A, Spector S, Roscigno G, Nkengasong J. Laboratory diagnosis of tuberculosis in resource-poor countries: challenges and opportunities. Clin Microbiol Rev. 2011;24(2):314-50. Epub 2011/04/13. doi: 10.1128/CMR.00059-10. PubMed PMID: 21482728; PMCID: PMC3122496.

36.   Toman K, Frieden T, World Health Organization. Toman's tuberculosis : case detection, treatment, and monitoring : questions and answers. 2nd ed. Geneva: World Health Organization; 2004. xviii, 332 p. p.

37.   Behr MA, Warren SA, Salamon H, Hopewell PC, Ponce de Leon A, Daley CL, Small PM. Transmission of Mycobacterium tuberculosis from patients smear-negative for acid-fast bacilli. Lancet. 1999;353(9151):444-9. Epub 1999/02/16. doi: 10.1016/s0140-6736(98)03406-0. PubMed PMID: 9989714.

38.   Tostmann A, Kik SV, Kalisvaart NA, Sebek MM, Verver S, Boeree MJ, van Soolingen D. Tuberculosis transmission by patients with smear-negative pulmonary tuberculosis in a large cohort in the Netherlands. Clin Infect Dis. 2008;47(9):1135-42. Epub 2008/10/01. doi: 10.1086/591974. PubMed PMID: 18823268.

39.   Hernandez-Garduno E, Cook V, Kunimoto D, Elwood RK, Black WA, FitzGerald JM. Transmission of tuberculosis from smear negative patients: a molecular epidemiology study. Thorax. 2004;59(4):286-90. Epub 2004/03/30. doi: 10.1136/thx.2003.011759. PubMed PMID: 15047946; PMCID: PMC1763818.

40.   Russell DA, Hatfull GF. PhagesDB: the actinobacteriophage database. Bioinformatics. 2017;33(5):784-6. Epub 2017/04/04. doi: 10.1093/bioinformatics/btw711. PubMed PMID: 28365761; PMCID: PMC5860397.

41.   Nobrega FL, Vlot M, de Jonge PA, Dreesens LL, Beaumont HJE, Lavigne R, Dutilh BE, Brouns SJJ. Targeting mechanisms of tailed bacteriophages. Nat Rev Microbiol. 2018;16(12):760-73. Epub 2018/08/15. doi: 10.1038/s41579-018-0070-8. PubMed PMID: 30104690.

42.   Vernhes E, Renouard M, Gilquin B, Cuniasse P, Durand D, England P, Hoos S, Huet A, Conway JF, Glukhov A, Ksenzenko V, Jacquet E, Nhiri N, Zinn-Justin S, Boulanger P. High affinity anchoring of the decoration protein pb10 onto the

bacteriophage T5 capsid. Sci Rep. 2017;7:41662. Epub 2017/02/07. doi: 10.1038/srep41662. PubMed PMID: 28165000; PMCID: PMC5292684.

43.   Fraser JS, Maxwell KL, Davidson AR. Immunoglobulin-like domains on bacteriophage: weapons of modest damage? Curr Opin Microbiol. 2007;10(4):382-7. Epub 2007/09/04. doi: 10.1016/j.mib.2007.05.018. PubMed PMID: 17765600.

44.   Lee S, Kriakov J, Vilcheze C, Dai Z, Hatfull GF, Jacobs WR, Jr. Bxz1, a new generalized transducing phage for mycobacteria. FEMS Microbiol Lett. 2004;241(2):271-6. Epub 2004/12/16. doi: 10.1016/j.femsle.2004.10.032. PubMed PMID: 15598543.

45.   Rybniker J, Kramme S, Small PL. Host range of 14 mycobacteriophages in Mycobacterium ulcerans and seven other mycobacteria including Mycobacterium tuberculosis--application for identification and susceptibility testing. J Med Microbiol. 2006;55(Pt 1):37-42. Epub 2006/01/03. doi: 10.1099/jmm.0.46238-0. PubMed PMID: 16388028.

46.   Ford ME, Stenstrom C, Hendrix RW, Hatfull GF. Mycobacteriophage TM4: genome structure and gene expression. Tuber Lung Dis. 1998;79(2):63-73. Epub 2000/01/25. doi: 10.1054/tuld.1998.0007. PubMed PMID: 10645443.

47.   Wu S, Liu B, Zhang X. Identification of a tail assembly gene cluster from deep-sea thermophilic bacteriophage GVE2. Virus Genes. 2009;38(3):507-14. Epub 2009/03/28. doi: 10.1007/s11262-009-0351-4. PubMed PMID: 19326202.

48.   Xu J, Hendrix RW, Duda RL. Conserved translational frameshift in dsDNA bacteriophage tail assembly genes. Mol Cell. 2004;16(1):11-21. Epub 2004/10/08. doi: 10.1016/j.molcel.2004.09.006. PubMed PMID: 15469818.

49.   Cuervo A, Pulido-Cid M, Chagoyen M, Arranz R, Gonzalez-Garcia VA, Garcia-Doval C, Caston JR, Valpuesta JM, van Raaij MJ, Martin-Benito J, Carrascosa JL. Structural characterization of the bacteriophage T7 tail machinery. J Biol Chem. 2013;288(36):26290-9. Epub 2013/07/26. doi: 10.1074/jbc.M113.491209. PubMed PMID: 23884409; PMCID: PMC3764833.

50.   Bartual SG, Otero JM, Garcia-Doval C, Llamas-Saiz AL, Kahn R, Fox GC, van Raaij MJ. Structure of the bacteriophage T4 long tail fiber receptor-binding tip. Proc Natl Acad Sci U S A. 2010;107(47):20287-92. Epub 2010/11/03. doi: 10.1073/pnas.1011218107. PubMed PMID: 21041684; PMCID: PMC2996694.

51.   Roy A, Kucukural A, Zhang Y. I-TASSER: a unified platform for automated protein structure and function prediction. Nat Protoc. 2010;5(4):725-38. Epub 2010/04/03. doi: 10.1038/nprot.2010.5. PubMed PMID: 20360767; PMCID: PMC2849174.

52.   Sambandamurthy VK, Derrick SC, Hsu T, Chen B, Larsen MH, Jalapathy KV, Chen M, Kim J, Porcelli SA, Chan J, Morris SL, Jacobs WR, Jr. Mycobacterium tuberculosis DeltaRD1 DeltapanCD: a safe and limited replicating mutant strain that protects immunocompetent and immunocompromised mice against experimental tuberculosis. Vaccine. 2006;24(37-39):6309-20. Epub 2006/07/25. doi: 10.1016/j.vaccine.2006.05.097. PubMed PMID: 16860907.

53.   Marrero J, Trujillo C, Rhee KY, Ehrt S. Glucose phosphorylation is required for Mycobacterium tuberculosis persistence in mice. PLoS Pathog. 2013;9(1):e1003116. Epub 2013/01/18. doi: 10.1371/journal.ppat.1003116. PubMed PMID: 23326232; PMCID: PMC3542180.

54.   Munoz-Elias EJ, McKinney JD. Mycobacterium tuberculosis isocitrate lyases 1 and 2 are jointly required for in vivo growth and virulence. Nat Med. 2005;11(6):638-44. Epub 2005/05/17. doi: 10.1038/nm1252. PubMed PMID: 15895072; PMCID: PMC1464426.

55.   Pethe K, Sequeira PC, Agarwalla S, Rhee K, Kuhen K, Phong WY, Patel V, Beer D, Walker JR, Duraiswamy J, Jiricek J, Keller TH, Chatterjee A, Tan MP, Ujjini M, Rao SP, Camacho L, Bifani P, Mak PA, Ma I, Barnes SW, Chen Z, Plouffe D, Thayalan P, Ng SH, Au M, Lee BH, Tan BH, Ravindran S, Nanjundappa M, Lin X, Goh A, Lakshminarayana SB, Shoen C, Cynamon M, Kreiswirth B, Dartois V, Peters EC, Glynne R, Brenner S, Dick T. A chemical genetic screen in Mycobacterium tuberculosis identifies carbon-source-dependent growth inhibitors devoid of in vivo efficacy. Nat Commun. 2010;1:57. Epub 2010/10/27. doi: 10.1038/ncomms1060. PubMed PMID: 20975714; PMCID: PMC3220188.

56.   Safi H, Gopal P, Lingaraju S, Ma S, Levine C, Dartois V, Yee M, Li L, Blanc L, Ho Liang HP, Husain S, Hoque M, Soteropoulos P, Rustad T, Sherman DR, Dick T, Alland D. Phase variation in Mycobacterium tuberculosis glpK produces transiently heritable drug tolerance. Proc Natl Acad Sci U S A. 2019;116(39):19665-74. Epub 2019/09/07. doi: 10.1073/pnas.1907631116. PubMed PMID: 31488707; PMCID: PMC6765255.

57.   Billig S, Schneefeld M, Huber C, Grassl GA, Eisenreich W, Bange FC. Lactate oxidation facilitates growth of Mycobacterium tuberculosis in human macrophages. Sci Rep. 2017;7(1):6484. Epub 2017/07/27. doi: 10.1038/s41598-017-05916-7. PubMed PMID: 28744015; PMCID: PMC5526930.

58.   Puckett S, Trujillo C, Wang Z, Eoh H, Ioerger TR, Krieger I, Sacchettini J,

Schnappinger D, Rhee KY, Ehrt S. Glyoxylate detoxification is an essential function of

malate synthase required for carbon assimilation in Mycobacterium tuberculosis. Proc

Natl Acad Sci U S A. 2017;114(11):E2225-E32. Epub 2017/03/08. doi:

10.1073/pnas.1617655114. PubMed PMID: 28265055; PMCID: PMC5358392.

59.   Upton AM, McKinney JD. Role of the methylcitrate cycle in propionate

metabolism and detoxification in Mycobacterium smegmatis. Microbiology (Reading).

2007;153(Pt 12):3973-82. Epub 2007/12/01. doi: 10.1099/mic.0.2007/011726-0.

PubMed PMID: 18048912.

60.   Marrero J, Rhee KY, Schnappinger D, Pethe K, Ehrt S. Gluconeogenic carbon

flow of tricarboxylic acid cycle intermediates is critical for Mycobacterium tuberculosis to

establish and maintain infection. Proc Natl Acad Sci U S A. 2010;107(21):9819-24.

Epub 2010/05/05. doi: 10.1073/pnas.1000715107. PubMed PMID: 20439709; PMCID:

PMC2906907.

61.   Schnappinger D, Ehrt S, Voskuil MI, Liu Y, Mangan JA, Monahan IM, Dolganov

G, Efron B, Butcher PD, Nathan C, Schoolnik GK. Transcriptional Adaptation of

Mycobacterium tuberculosis within Macrophages: Insights into the Phagosomal

Environment. J Exp Med. 2003;198(5):693-704. Epub 2003/09/04. doi:

10.1084/jem.20030846. PubMed PMID: 12953091; PMCID: PMC2194186.

62.   Rohde KH, Veiga DF, Caldwell S, Balazsi G, Russell DG. Linking the

transcriptional profiles and the physiological states of Mycobacterium tuberculosis

during an extended intracellular infection. PLoS Pathog. 2012;8(6):e1002769. Epub

2012/06/28. doi: 10.1371/journal.ppat.1002769. PubMed PMID: 22737072; PMCID: PMC3380936.

63.   Beste DJ, Bonde B, Hawkins N, Ward JL, Beale MH, Noack S, Noh K, Kruger NJ, Ratcliffe RG, McFadden J. (1)(3)C metabolic flux analysis identifies an unusual route for pyruvate dissimilation in mycobacteria which requires isocitrate lyase and carbon dioxide fixation. PLoS Pathog. 2011;7(7):e1002091. Epub 2011/08/05. doi: 10.1371/journal.ppat.1002091. PubMed PMID: 21814509; PMCID: PMC3141028.

64.   Watanabe S, Zimmermann M, Goodwin MB, Sauer U, Barry CE, 3rd, Boshoff HI. Fumarate reductase activity maintains an energized membrane in anaerobic Mycobacterium tuberculosis. PLoS Pathog. 2011;7(10):e1002287. Epub 2011/10/15. doi: 10.1371/journal.ppat.1002287. PubMed PMID: 21998585; PMCID: PMC3188519.

65.   Kim H. Structure-guided Inhibitor Design of Mycobacterium Tuberculosis Drug Targets from Central Carbon Metabolism. https : / /hdl .handle .net /1969 .1 /187362.: Texas A&M University; 2016.

66.   Pietranico SL, Foley LH, Huby N, Yun W, Dunten P, Vermeulen J, Wang P, Toth K, Ramsey G, Gubler ML, Wertheimer SJ. C-8 Modifications of 3-alkyl-1,8-dibenzylxanthines as inhibitors of human cytosolic phosphoenolpyruvate carboxykinase. Bioorg Med Chem Lett. 2007;17(14):3835-9. Epub 2007/05/29. doi: 10.1016/j.bmcl.2007.05.013. PubMed PMID: 17532214.

67.   Foley LH, Wang P, Dunten P, Ramsey G, Gubler ML, Wertheimer SJ. X-ray structures of two xanthine inhibitors bound to PEPCK and N-3 modifications of substituted 1,8-dibenzylxanthines. Bioorg Med Chem Lett. 2003;13(21):3871-4. Epub 2003/10/14. doi: 10.1016/s0960-894x(03)00723-6. PubMed PMID: 14552798.

68.   Foley LH, Wang P, Dunten P, Ramsey G, Gubler ML, Wertheimer SJ. Modified 3-alkyl-1,8-dibenzylxanthines as GTP-competitive inhibitors of phosphoenolpyruvate carboxykinase. Bioorg Med Chem Lett. 2003;13(20):3607-10. Epub 2003/09/25. doi: 10.1016/s0960-894x(03)00722-4. PubMed PMID: 14505680.

69.   Lamprecht DA, Finin PM, Rahman MA, Cumming BM, Russell SL, Jonnala SR, Adamson JH, Steyn AJ. Turning the respiratory flexibility of Mycobacterium tuberculosis against itself. Nat Commun. 2016;7:12393. Epub 2016/08/11. doi: 10.1038/ncomms12393. PubMed PMID: 27506290; PMCID: PMC4987515.

70.   Mackenzie JS, Lamprecht DA, Asmal R, Adamson JH, Borah K, Beste DJV, Lee BS, Pethe K, Rousseau S, Krieger I, Sacchettini JC, Glasgow JN, Steyn AJC. Bedaquiline reprograms central metabolism to reveal glycolytic vulnerability in Mycobacterium tuberculosis. Nat Commun. 2020;11(1):6092. Epub 2020/12/02. doi: 10.1038/s41467-020-19959-4. PubMed PMID: 33257709; PMCID: PMC7705017.

71.   Kasbekar M, Fischer G, Mott BT, Yasgar A, Hyvonen M, Boshoff HI, Abell C, Barry CE, 3rd, Thomas CJ. Selective small molecule inhibitor of the Mycobacterium tuberculosis fumarate hydratase reveals an allosteric regulatory site. Proc Natl Acad Sci U S A. 2016;113(27):7503-8. Epub 2016/06/22. doi: 10.1073/pnas.1600630113. PubMed PMID: 27325754; PMCID: PMC4941444.

72.   Li K, Schurig-Briccio LA, Feng X, Upadhyay A, Pujari V, Lechartier B, Fontes FL, Yang H, Rao G, Zhu W, Gulati A, No JH, Cintra G, Bogue S, Liu YL, Molohon K, Orlean P, Mitchell DA, Freitas-Junior L, Ren F, Sun H, Jiang T, Li Y, Guo RT, Cole ST, Gennis RB, Crick DC, Oldfield E. Multitarget drug discovery for tuberculosis and other infectious

diseases. J Med Chem. 2014;57(7):3126-39. Epub 2014/02/27. doi: 10.1021/jm500131s. PubMed PMID: 24568559; PMCID: PMC4084622.

73. Bukhdruker S, Varaksa T, Grabovec I, Marin E, Shabunya P, Kadukova M, Grudinin S, Kavaleuski A, Gusach A, Gilep A, Borshchevskiy V, Strushkevich N. Hydroxylation of Antitubercular Drug Candidate, SQ109, by Mycobacterial Cytochrome P450. Int J Mol Sci. 2020;21(20). Epub 2020/10/22. doi: 10.3390/ijms21207683. PubMed PMID: 33081390; PMCID: PMC7589583.

74. Geissmann Q. OpenCFU, a new free and open-source software to count cell colonies and other circular objects. PLoS One. 2013;8(2):e54072. Epub 2013/03/05. doi: 10.1371/journal.pone.0054072. PubMed PMID: 23457446; PMCID: PMC3574151.

75. DeJesus MA, Sacchettini JC, Ioerger TR. Reannotation of translational start sites in the genome of Mycobacterium tuberculosis. Tuberculosis (Edinb). 2013;93(1):18-25. Epub 2013/01/01. doi: 10.1016/j.tube.2012.11.012. PubMed PMID: 23273318; PMCID: PMC3582765.

76. Rodnina MV. Translation in Prokaryotes. Cold Spring Harb Perspect Biol. 2018;10(9). Epub 2018/04/18. doi: 10.1101/cshperspect.a032664. PubMed PMID: 29661790; PMCID: PMC6120702.

77. Cruz-Vera LR, Magos-Castro MA, Zamora-Romo E, Guarneros G. Ribosome stalling and peptidyl-tRNA drop-off during translational delay at AGA codons. Nucleic Acids Res. 2004;32(15):4462-8. Epub 2004/08/20. doi: 10.1093/nar/gkh784. PubMed PMID: 15317870; PMCID: PMC516057.

78.   Giudice E, Gillet R. The task force that rescues stalled ribosomes in bacteria. Trends Biochem Sci. 2013;38(8):403-11. Epub 2013/07/04. doi: 10.1016/j.tibs.2013.06.002. PubMed PMID: 23820510.

79.   Moore SD, Sauer RT. The tmRNA system for translational surveillance and ribosome rescue. Annu Rev Biochem. 2007;76:101-24. Epub 2007/02/13. doi: 10.1146/annurev.biochem.75.103004.142733. PubMed PMID: 17291191.

80.   Brunel R, Charpentier X. Trans-translation is essential in the human pathogen Legionella pneumophila. Sci Rep. 2016;6:37935. Epub 2016/11/29. doi: 10.1038/srep37935. PubMed PMID: 27892503; PMCID: PMC5124942.

81.   Woolstenhulme CJ, Parajuli S, Healey DW, Valverde DP, Petersen EN, Starosta AL, Guydosh NR, Johnson WE, Wilson DN, Buskirk AR. Nascent peptides that block protein synthesis in bacteria. Proc Natl Acad Sci U S A. 2013;110(10):E878-87. Epub 2013/02/23. doi: 10.1073/pnas.1219536110. PubMed PMID: 23431150; PMCID: PMC3593848.

82.   Pech M, Karim Z, Yamamoto H, Kitakawa M, Qin Y, Nierhaus KH. Elongation factor 4 (EF4/LepA) accelerates protein synthesis at increased Mg2+ concentrations. Proc Natl Acad Sci U S A. 2011;108(8):3199-203. Epub 2011/02/09. doi: 10.1073/pnas.1012994108. PubMed PMID: 21300907; PMCID: PMC3044372.

83.   Pinkham Schweber JT. Partial Depletion of Pth Increases Susceptibility to Macrolide
Drug Treatment in M. tuberculosis. http://nrs.harvard.edu/urn-3:HUL.InstRepos:33797262: Harvard University; 2016.

84.   Minato Y, Gohl DM, Thiede JM, Chacon JM, Harcombe WR, Maruyama F, Baughn AD. Genomewide Assessment of Mycobacterium tuberculosis Conditionally Essential Metabolic Pathways. mSystems. 2019;4(4). Epub 2019/06/27. doi: 10.1128/mSystems.00070-19. PubMed PMID: 31239393; PMCID: PMC6593218.

85.   DeJesus MA, Gerrick ER, Xu W, Park SW, Long JE, Boutte CC, Rubin EJ, Schnappinger D, Ehrt S, Fortune SM, Sassetti CM, Ioerger TR. Comprehensive Essentiality Analysis of the Mycobacterium tuberculosis Genome via Saturating Transposon Mutagenesis. mBio. 2017;8(1). Epub 2017/01/18. doi: 10.1128/mBio.02133-16. PubMed PMID: 28096490; PMCID: PMC5241402.

86.   Sassetti CM, Boyd DH, Rubin EJ. Genes required for mycobacterial growth defined by high density mutagenesis. Mol Microbiol. 2003;48(1):77-84. Epub 2003/03/27. doi: 10.1046/j.1365-2958.2003.03425.x. PubMed PMID: 12657046.

87.   Griffin JE, Gawronski JD, Dejesus MA, Ioerger TR, Akerley BJ, Sassetti CM. High-resolution phenotypic profiling defines genes essential for mycobacterial growth and cholesterol catabolism. PLoS Pathog. 2011;7(9):e1002251. Epub 2011/10/08. doi: 10.1371/journal.ppat.1002251. PubMed PMID: 21980284; PMCID: PMC3182942.

88.   Bonin PD, Erickson LA. Development of a fluorescence polarization assay for peptidyl-tRNA hydrolase. Anal Biochem. 2002;306(1):8-16. Epub 2002/06/19. doi: 10.1006/abio.2002.5700. PubMed PMID: 12069408.

89.   Lea WA, Simeonov A. Fluorescence polarization assays in small molecule screening. Expert Opin Drug Discov. 2011;6(1):17-32. Epub 2012/02/14. doi: 10.1517/17460441.2011.537322. PubMed PMID: 22328899; PMCID: PMC3277431.

90.   Chernyakov I, Baker MA, Grayhack EJ, Phizicky EM. Chapter 11. Identification and analysis of tRNAs that are degraded in Saccharomyces cerevisiae due to lack of modifications. Methods Enzymol. 2008;449:221-37. Epub 2009/02/14. doi: 10.1016/S0076-6879(08)02411-7. PubMed PMID: 19215761; PMCID: PMC2788775.